การสังเคราะห์อนุภาคคอมโพสิทของสังกะสีออกไซด์และอนุภาคคาร์บอนระดับนาโนเมตร
ด้วยปฏิกิริยาสภาวะก๊าซ

นางสาวจีรพร กลั่นหวาน
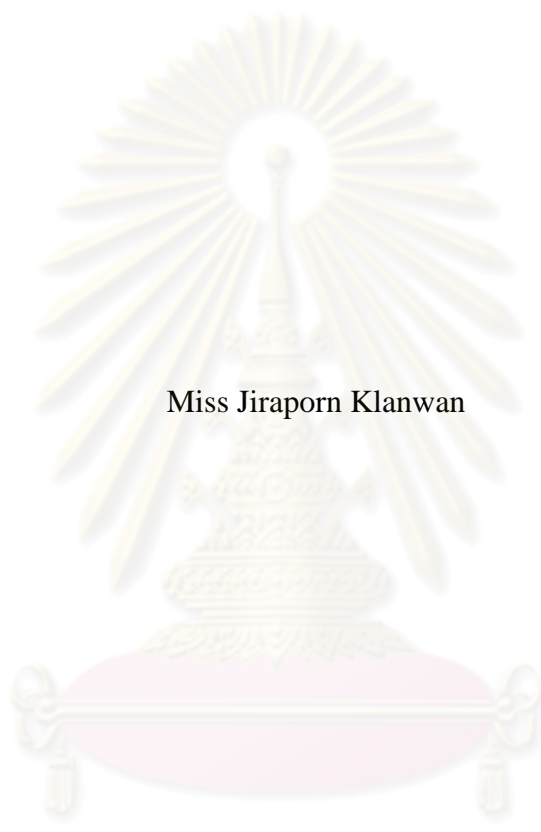
SYNTHESIS OF PARTICULATE COMPOSITE OF ZINC OXIDE AND CARBON
NANOPARTICLES BY GAS PHASE REACTION

Miss Jiraporn Klanwan

A Dissertation Submitted in Partial Fulfillment of the Requirements
for the Degree of Doctor of Engineering Program in Chemical Engineering
Department of Chemical Engineering
Faculty of Engineering
Chulalongkorn University
Academic Year 2010

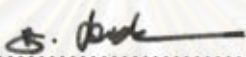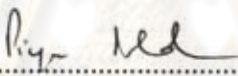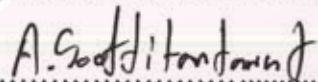|	
Thesis Title	SYNTHESIS OF PARTICULATE COMPOSITE OF ZINC OXIDE AND CARBON NANOPARTICLES BY GAS PHASE REACTION
By	Miss Jiraporn Klanwan
Field of study	Chemical Engineering
Thesis Advisor	Associate Professor Tawatchai Charinpanitkul, D.Eng.
Thesis Co-advisor	Apinan Soottitantawat, D.Eng.

Accepted by the Faculty of Engineering, Chulalongkorn University in Partial Fulfillment of the Requirements for the Doctor's Degree

.... Dean of the Faculty of Engineering
(Associate Professor Boonsom Lerdhirunwong, Dr.Ing.)
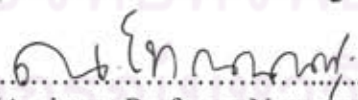
THESIS COMMITTEE

.... Chairman
(Professor Piyasarn Praserthdam, Dr.Ing.)

.... Thesis Advisor
(Associate Professor Tawatchai Charinpanitkul, D.Eng.)

.... Thesis Co-advisor
(Apinan Soottitantawat, D.Eng.)
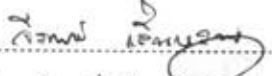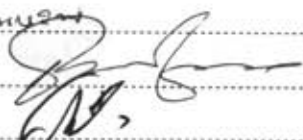
.... Examiner
(Assistant Professor Varong Pavarajarn, Ph.D.)

.... Examiner
(Assistant Professor Nattaporn Tonanon, D.Eng.)

.... External Examiner
(Sorapong Pavasupree, D.Eng.)

จีรพร กลั่นหวาน : การสังเคราะห์อนุภาคคอมโพสิทของสังกะสีออกไชด์และอนุภาคคาร์บอน ระดับนาโนเมตรด้วยปฏิกิริยาสภาวะก๊าซ (SYNTHESIS OF PARTICULATE COMPOSITE OF ZINC OXIDE AND CARBON NANOPARTICLES BY GAS PHASE REACTION) อ. ที่ ปรึกษาวิทยานิพนธ์หลัก : รศ.คร. ธวัชชัย ชรินพาณิชกุล, อ. ที่ปรึกษาวิทยานิพนธ์ร่วม : คร. อภินันท์ สุทธิธารธวัช, 135 หน้า.

งานวิจัยนี้ อนุภาคคอมโพสิทของสังกะสีออกไชด์และอนุภาคคาร์บอนระดับนาโนเมตรถูก สังเคราะห์ขึ้นด้วยปฏิกิริยาสภาวะก๊าซในขั้นตอนเดียวโดยใช้กลีเซอรอลและเฟอร์โรซีนเป็นแหล่งของ คาร์บอนและเหล็กสำหรับการเกิดอนุภาคคาร์บอนระดับนาโมเมตร ขณะที่ใช้ผงสังกะสีบริสุทธิ์สำหรับการ เกิดอนุภาคสังกะสีออกไชด์ การสังเคราะห์แบบแยกเดี่ยวของอนุภาคคาร์บอนระดับนาโนเมตรและอนุภาค สังกะสีออกไชด์ถูกทำการศึกษาแยกจากกัน เพื่อศึกษาตัวแปรที่มีอิทธิพลต่อการเกิดของแต่ละองค์ประกอบ ของอนุภาคคอมโพสิทของสังกะสีออกไชด์/อนุภาคคาร์บอนระดับนาโนเมตร อนุภาคคาร์บอนระดับนาโน เมตรโดยเฉพาะอย่างยิ่ง ท่อคาร์บอนระดับนาโนเมตรแบบผนังหลายชั้นถูกสังเคราะห์ขึ้นด้วยวิธีการตก สะสมไอเชิงเคมี ภายใต้การควบคุมอัตราการไหลของก๊าซไนโตรเจน อุณหภูมิที่ใช้ในการสังเคราะห์ และ อัตราส่วนโดยโมลของกลีเซอรอลต่อเฟอร์โรซีน การสังเคราะห์ท่อคาร์บอนระดับนาโนเมตรแบบผนังชั้น เดียวถูกทำการศึกษาเช่นกันด้วยวิธียิงเลเซอร์โดยการควบคุมความเข้มเลเซอร์และอุณหภูมิที่ใช้ในการ สังเคราะห์ เพื่อให้เกิดเข้าใจในการเกิดท่อคาร์บอนระดับนาโมเมตร ในขณะที่อนุภาคสังกะสีออกไชด์ระดับ นาโมเมตรถูกสังเคราะห์ขึ้นด้วยปฏิกิริยาออกซิเดชั่นของสังกะสีบริสุทธิ์ โดยการควบคุมอัตราการไหลของ ก๊าซไนโตรเจน อุณหภูมิที่ใช้ในการสังเคราะห์ และอัตราการไหลของก๊าซออกซิเจน หลังจากนั้นอนุภาค คอมโพสิทถูกทำการศึกษาภายใต้สภาวะที่ถูกออกแบบจากข้อมูลของการศึกษาข้างต้น การศึกษาทางด้าน เทอร์โมไดนามิกส์แสดงให้เห็นการเกิดปฏิกิริยาออกซิเดชั่นของคาร์บอนและเหล็กอย่างหลีกเลี่ยงไม่ได้ ภายใต้ช่วงกว้างของอุณหภูมิที่ใช้ในการสังเคราะห์ อุณหภูมิที่ใช้ในการสังเคราะห์ถูกพบว่าเป็นตัวแปรหลัก ของการสังเคราะห์อนุภาคคอมโพสิทของสังกะสีออกไชด์/ท่อคาร์บอนระดับนาโนเมตรแบบผนังหลายชั้น จากผลการทดลอง อนุภาคคอมโพสิทของสังกะสีออกไชด์/ท่อคาร์บอนระดับนาโนเมตรแบบผนังหลายชั้น ถูกสังเคราะห์ขึ้นภายใต้สภาวะของอัตราการไหลของก๊าซไนโตรเจน อัตราการไหลของก๊าซออกซิเจน และ อุณหภูมิที่ใช้ในการสังเคราะห์ที่ 500 มิลลิลิตรต่อนาที 100 มิลลิลิตรต่อนาที และ 800 องศาเซลเซียส ตามลำดับ

ภาควิชา: วิศวกรรมเคมี   ลายมือชื่อนิสิต ....

สาขาวิชา: วิศวกรรมเคมี   ลายมือชื่อ อ.ที่ปรึกษาวิทยานิพนธ์หลัก ....

ปีการศึกษา: 2553   ลายมือชื่อ อ.ที่ปรึกษาวิทยานิพนธ์ร่วม ....

4971804921: MAJOR CHEMICAL ENGINEERING
KEYWORDS : ZnO / CARBON NANOPARTICLES / COMPOSITE / GAS PHASE REACTION

JIRAPORN   KLANWAN: SYNTHESIS   OF   PARTICULATE COMPOSITE OF ZINC OXIDE AND CARBON NANOPARTICLES BY GAS PHASE REACTION. ADVISOR : ASSOC. PROF. TAWATCHAI CHARINPANITKUL,   D.Eng.,   CO-ADVISOR   :   APINAN SOOTTITANTAWAT, D.Eng., 135 pp.

In this work, particulate composites of ZnO and carbon nanoparticles were synthesized by single-step gas phase reaction. Glycerol and ferrocene were used as carbon and iron sources for formation of the carbon nanoparticles, while Zn powder was employed as Zn source for the formation of ZnO. Isolated synthesis of carbon nanoparticles and ZnO particles was separately studied for investigating experimental parameters which affected the formation of each constituent of ZnO/CNT composite. The carbon nanoparticles, especially MWCNTs, were synthesized by chemical vapor deposition by manipulating N_2 flow rate, synthesizing temperature and glycerol to ferrocene molar ratio. To understand the formation of the CNTs, synthesis of SWCNTs by laser ablation was also investigated by controlling laser intensity and synthesizing temperature. While, the ZnO nanoparticles were synthesized by oxidation of pure Zn by adjusting N_2 flow rate, synthesizing temperature and O_2 flow rate. The composites were then investigated under designated conditions with respect to data of previous investigation. The study of thermodynamics exhibited unavoidable oxidation of C and Fe over wide ranges of the synthesizing temperature. The synthesizing temperature was found to be a major parameter for the synthesis of the ZnO/CNT composites. Based on the experimental results, the ZnO/MWCNT composites could be synthesized under the condition of the N_2 flow rate, O_2 flow rate and synthesizing temperature of 500 mL/min, 100 mL/min and 800 °C, respectively.

Department :   Chemical Engineering   Student's Signature   Jiraporn Klanwan

Field of Study :   Chemical Engineering   Advisor's Signature   T.Charinpanitkul

Academic Year : 2010   Co-advisor's Signature   A.Scott Hardnrod

ACKNOWLEDGEMENTS

CONTENTS

LIST OF TABLES

LIST OF FIGURES

Page

NOMENCLATURES

Δ	=	Coefficient of Pilling and Bedworth
α	=	Conversion of ZnO
τ	=	Time of totally Zn consumption
ω_{RBM}	=	Radial breathing mode frequency
bcc	=	Body-centered cubic
C	=	Carbon
Co	=	Cobalt
CPC	=	Condensation particle counter
C_{O_2}	=	Concentration of O_2
$C_{O_2}^e$	=	Equilibrium concentration of O_2
$C_{O_2}^i$	=	Initial concentration of O_2
d_{Zn}	=	Density of Zn
D_{O_2}	=	Diffusion coefficient of O_2
D_A	=	Projected area diameter of CNT
D_f	=	Diameter of fibrous CNT
D_m	=	Mobility based diameter of CNT
DMA	=	Differential mobility analyzer
d_t	=	Diameter of SWCNT
fcc	=	Face-centered cubic
Fe	=	Iron
Fe_3C	=	Iron carbide
k_{CNTs}	=	Rate constant of CNTs
k_{Zn}	=	Rate constant of zinc
L_f	=	Length of CNT,
m_{O_2}	=	Mass of O_2
m_{Zn}^0	=	Initial mass of zinc
m_{Zn}^t	=	Mass of zinc at time t

N_2	=	Nitrogen
N_{O_2}	=	Diffusion flux of O_2
Ni	=	Nickel
O_2	=	Oxygen
R	=	Radius
r_0	=	Initial radius of Zn particle
r_1	=	Initial radius of the reaction interface (metal/oxide)
r_2	=	Initial radius of the oxide layer
RBM	=	Radial breathing mode
S_1	=	Surface area of the reaction interface
SEM	=	Scanning electron microscopy
SMPS	=	Scanning mobility particle analyzer
T	=	Temperature
t	=	time
TEM	=	Transmission electron microscopy
VLS	=	Vapor-liquid-solid
VS	=	Vapor-solid
V_{Zn}^0	=	Initial volume of Zn
V_{Zn}	=	Volume of Zn
V_{ZnO}	=	Volume of ZnO
$W_{C,1}$	=	Weight of synthesized carbon at zone 1
$W_{C,2}$	=	Weight of synthesized carbon at zone 2
$W_{C,3}$	=	Weight of synthesized carbon at zone 3
$W_{ferrocene}$	=	Weight of used ferrocene
$W_{glycerol}$	=	Weight of used glycerol
$W_{ZnO,2}$	=	Weight of synthesized ZnOat zone 2
$W_{ZnO,3}$	=	Weight of synthesized ZnO at zone 3
$W_{ZnO/MWCNT}$	=	Weight of synthesized ZnO/MWCNT composites
XRD	=	X-Ray Diffraction
Zn	=	Zinc
ZnO	=	Zinc oxide
Z_p	=	Electrical mobility of the collected particles

R_1	=	Radius of the inner electrode
R_2	=	Radius of the outer electrode
L	=	Length of electrode
V	=	Applied voltage
n	=	Number of elementary charge units
e	=	Elementary unit of charge
C_c	=	Cunningham slip correction factor
μ	=	Gas viscosity
d_p	=	Particle diameter
K_n	=	Knudsen number
λ	=	Mean free path
ΔH	=	Enthalpy of reaction
ΔS	=	Entropy of reaction
T	=	Temperature of reaction
ΔG°	=	Difference between the free energy of 1 mole of gaseous MO at 1 atm pressure, and the sum of the free energies of a half of 1 mole of O_2 at 1 atm pressure and 1 mole of gaseous M at 1 atm pressure, all at the temperature T
p_{MO}	=	Equilibrium vapor pressure of solid MO at temperature of T
p_M	=	Equilibrium vapor pressure of solid M at temperature of T
p_{O_2}	=	Equilibrium pressure of O_2 at temperature of T
$G^{\circ}_{M(g)}$	=	Molar free energy of the gaseous M under a pressure of 1 atm and temperature of T
$G^{\circ}_{M(s)}$	=	Molar free energy of the solid M under a pressure of 1 atm and temperature of T
$G^{\circ}_{MO(g)}$	=	Molar free energy of the gaseous MO under a pressure of 1 atm and temperature of T
$G^{\circ}_{MO(s)}$	=	Molar free energy of the solid MO under a pressure of 1 atm and temperature of T

$V_{M(s)}$ = Molar volume of the solid M at the pressure of P and temperature of T

$V_{MO(s)}$ = Molar volume of the solid MO at the pressure of P and temperature of T

ศูนย์วิทยทรัพยากร
จุฬาลงกรณ์มหาวิทยาลัย

CHAPTER I

INTRODUCTION

1.1 Background and motivation

Since the discovery of carbon nanotubes (CNTs) (Iijima, 1991), the CNTs have attracted considerable attention owing to their unique electrical and extraordinary mechanical properties as well as optical and thermal properties (Saito, Dresselhaus and Dresselhaus, 1998). From many researches of nanoelectronic devices, the CNTs have been widely adopted as field emitters due to their special properties such as high aspect ratio, low work function and good electrical conductivity. To improve field emission properties of the CNTs, the CNT growth is synthesized with metal oxides to improve the field emission properties (Yu et al., 2002). Metal oxides enhance the emission sites and reduce the work function, resulting in lower turn-on voltages in comparison with pristine CNTs. Among variety of metal oxides, zinc oxide (ZnO), which is a semi-conducting material with a large exciton binding energy of 60 meV, is a promising candidate material for field emission improvement (Özgür et al., 2005) due to its wide band gap (3.3 eV) and small electron affinity (2.1 eV). In the past researches, ZnO nanostructures grown with CNTs could reduce the threshold electric field because ZnO has smaller electron affinity than the CNT, and the ZnO/CNT junction is similar to a ZnO/metal junction allowing electrons to be easily emitted into a vacuum (Yu et al, 2006).

Recently, several researchers reported synthesis methods of the ZnO/CNT composites (Chen et al., 2006; Wu et al., 2007). These methods are related to wet chemical process of various chemicals operated under low temperature which seems to be complicated and might cause contamination of synthesized products. From the limitations of these previous works, another simple synthesis method of the composites such a facile single-step synthesis which expected to decrease contamination was motivated. In this work, the ZnO/CNT composites were synthesized using gas phase reaction within single-step process. Glycerol, known as by-product of bio-diesel production, was used as carbon source, while ferrocene was used as iron catalyst for the formation of the carbon nanoparticles, especially

MWCNTs using chemical vapor deposition (CVD) method. Zn powder was employed as Zn source for the formation of ZnO nanoparticles using oxidation method. The carbon nanoparticle synthesis process was simultaneously taken place with ZnO nanoparticles synthesis process within the same of reactor system, leading to partial formation of their composites. Various parameters including nitrogen flow rate, oxygen flow rate, synthesizing temperature and glycerol to ferrocene molar ratio significantly affected on the formation of the composites. Therefore, isolated synthesis of carbon nanoparticles and ZnO particles was previously studied for controlling various parameters, leading to the formation of the ZnO/MWCNT composites under designated condition from the previous studies.

1.2 Objective of research

The objective of this research was to synthesize the ZnO/CNT composites by gas phase reaction. Pure zinc and oxygen were employed as sources for fabrication of ZnO nanoparticles while glycerol and ferrocene were used as carbon and iron sources for fabrication carbon nanoparticles. The research was preliminary investigated from study of isolated synthesis of carbon nanoparticles and ZnO particles for controlling various parameters which affected on the formation of the composite. The ZnO/MWCNT composites were sequentially synthesized under the designated condition.

1.3 Scope of research

1.3.1 Synthesize SWCNTs using laser ablation under atmospheric pressure by controlling laser intensity and temperature.

1.3.2 Synthesize carbon nanoparticles using CVD of glycerol and ferrocene by varying nitrogen flow rate, synthesizing temperature and glycerol to ferrocene molar ratio.

1.3.3 Synthesize ZnO nanoparticles by oxidation of zinc under various conditions of nitrogen flow rate, synthesizing temperature and oxygen flow rate.

1.3.4 Synthesize ZnO/MWCNT composites by gas phase reaction under designated condition.

1.35 Characterize the synthesized nanoparticles by following instruments:

- Scanning Electron Microscope (SEM)

- Transmission Electron Microscope (TEM)

- Raman Spectroscope

- Scanning Mobility Particle Sizer (SMPS)

- X-Ray Diffraction (XRD)

- UV-Visible Spectrophotometer (UV-Vis)

- Fourier Transform Infrared Spectrophotometer (FT-IR)

1.4 Procedure of the research

1.4.1 Survey and review related literatures

1.4.2 Synthesize SWCNTs by laser ablation

1.4.3 Synthesize carbon nanoparticles by CVD of glycerol and ferrocene

1.4.4 Synthesize ZnO by oxidation of Zn

1.4.5 Perform preliminary experiments to find out suitable condition for the synthesis of the ZnO/MWCNT composites by gas phase reaction

1.4.6 Analyze and conclude the experimental results

1.4.7 Prepare a manuscript for journal publication and dissertation

1.5 Obtained benefits

1.5.1 Obtain fundamental knowledge related to carbon nanoparticles, ZnO nanoparticles and their composites.

1.5.2 Obtain advanced knowledge related to synthesis methods and formation mechanisms of carbon nanoparticles, ZnO nanoparticles and their composites

CHAPTER II

FUNDAMENTAL KNOWLEDGE AND LITERATURE REVIEW

2.1 Carbon nanotubes (CNTs)

2.1.1 Structure of CNTs

Carbon nanotubes (CNTs) which were discovered in 1991 (Iijima, 1991) are allotropes of carbon with a cylindrical structure, built from sp^2 carbon units and consist of honeycomb lattices known as graphene sheet. They are a seamless structure with a diameter of a few nanometers but lengths of many microns.

They can be classified into 2 main types: single-walled carbon nanotubes (SWCNTs) and multi-walled carbon nanotubes (MWCNTs). The SWCNTs are made of a single rolled graphite sheet with a typical diameter of about 1 nm while the MWCNTs are closed graphite tubules rolled like a graphite sheet with the distance between sheets about 0.34 nm as shown in Figure 2.1 (a) and (b), respectively.

(a)   (b)

Figure 2.1 Structures of (a) SWCNTs and (b) MWCNTs.

(itech.dickinson.edu)

Depending on how the graphene sheets of a nanotube are rolled together at different chirality and angle (Saito et al., 1998), they are classified by their chiral vectors (C_h) as shown in equation 2.1 into armchair, zigzag and chiral shapes as shown in Figure 2.2.

$$C_h = na_1 + ma_2 \equiv (n, m) \qquad (2.1)$$

where a_1 and a_2 are unit vectors in the two-dimensional hexagonal lattice

   n and m are integers

(a)

(b)   (c)   (d)
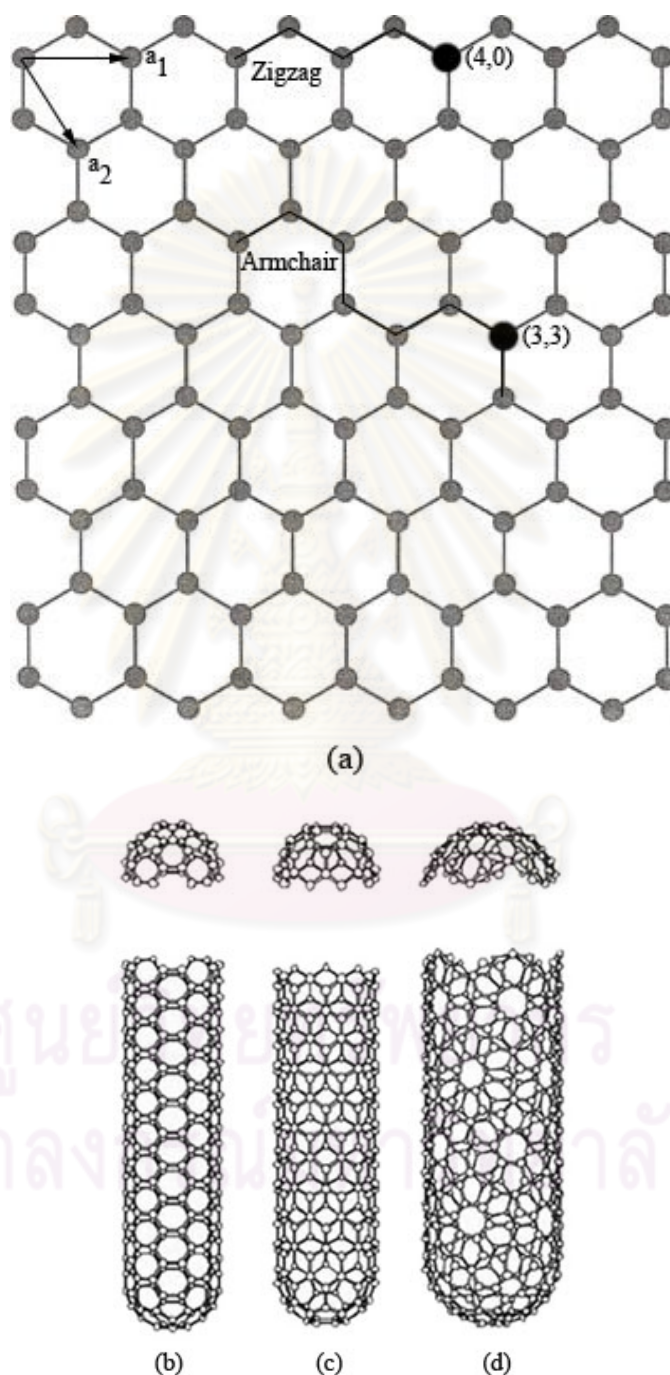
Figure 2.2 Structures of (a) an unrolled graphene sheet of a nanotube, (b) an armchair nanotube, (c) a zigzag nanotube and (d) a chiral nanotube

(cnx.org/content/m22580/latest/)

Another important parameter which determines properties of nanotube along with diameter of the tube is chiral angle (θ), the angle between C_h and a_1 with value in the range of 0° and 30°. An armchair nanotube corresponds to the case of n = m, that is C_h = (n, n) with the chiral angle of 30°, while a zigzag nanotube corresponds to the case of m = 0, or C_h = (n, 0) with the chiral angle of 0°. All other (n, m) chiral vectors correspond to chiral nanotubes with the chiral angles between 0° and 30° as shown in Table 2.1

Table 2.1 Classification of carbon nanotubes and their electrical conductivity

Type	Chiral vector (C_h)	Chiral angle (θ)	Electrical conductivity
Armchair	(n,n)	30°	Metallic
Zigzag	(n,0)	0°	Metallic or Semiconducting*
Chiral	(n,m)	0°-30°	Metallic or Semiconducting*

*Electrical conductivity of zigzag and chiral nanotubes depend on theirs chiral vector

The characteristic structure of a nanotube strongly affects its electrical properties which the armchair nanotubes are always metallic, while zigzag and chiral nanotubes are either metallic or semiconducting, depending on theirs chiral vector.

2.1.2 Physical properties of CNTs

The CNTs are known to have remarkable electronic and mechanical properties because of their unique structures, leading to application in nano-electronic and nano-mechanical devices, respectively. Furthermore, properties of carbon nanotubes can also be expanded to thermal and optical properties as well.

As a result of the carbon–carbon sp^2 bonding, they are predicted to have high stiffness and axial strength which must ultimately depend on the strength of its interatomic bonds (Paradise and Goswami, 2007)). On a per-bond basis, the graphitic sp^2 bonding is 33% stronger than the sp^3 bonding of diamond, the hardest substance in nature. Experimental and theoretical results have shown an elastic modulus of greater than 1 TPa (the elastic modulus of diamond is 1.2 TPa) and reported strengths 10–100 times higher than the strongest steel at a fraction of the weight (Thostenson, Ren, and Chou, 2001). Experimental result in tensile strengths

has shown in the range from 11 to 63 GPa, with dependence on the outer shell diameter, which is not far from the theoretical yield strength of about 100 GPa. From Table 2.2, the CNTs show their theoretical tensile strength over diamond. This is particularly beneficial for high-strength properties of composites based on nanotubes.

Table 2.2 Theoretical mechanical properties of CNTs (Yamabe, 1995)

Material	Young's modulus (GPa)	Tensile strength (GPa)
SWCNTs	1054	150
MWCNTs	1200	150
Diamond	600	130
Steel	208	0.4
Wood	16	0.008

Thermal properties including specific heat and thermal conductivity of carbon nanotubes are determined primarily by the phonons which are a result of lattice vibrations (Popov, 2004). The thermal conductivity of carbon nanotubes is dependent on the temperature. Especially at low temperatures, the phonon contribution to these quantities dominates (Berber, Kwon, and Tomànek, 2000). Experimental result shows thermal conductivity of SWCNTs at room temperature about 3500 $W \cdot m^{-1} \cdot K^{-1}$ (Pop et al., 2006) which compares to copper, a well-known metal for its good thermal conductivity, which transmits 385 $W \cdot m^{-1} \cdot K^{-1}$.

Theoretical and experimental results show superior electrical properties of carbon nanotubes. In theory, metallic nanotubes can produce electric current carrying capacity 1000 times higher than copper wires (Collins, and Avouris, 2000). The electronic capabilities possessed by carbon nanotubes are seen to arise predominately from interlayer interactions, rather than from interlayer interactions between multi-layers within a single carbon nanotube or between isolated nanotubes (Dresselhaus, Dresselhaus, and Saito, 1995).

Unique optical properties have proved with capabilities of acting as either a metal or semiconductor, which depend on tubule diameter and chiral angle. Metallic conduction can be achieved without introduction of doping dependence. For semi-conducting nanotubes, the band gaps have been found to be proportional to a

fraction of the diameter and without relation to the tubule chirality (Dresselhaus et al., 1995).

2.1.3 Synthesis of CNTs

There are several processes to synthesize CNTs which are difference in how carbon atoms are produced from carbon sources, including sublimation of graphite by arc discharge (Antisari, Marazzi, and Krsmanovic, 2003) and laser ablation method (Yudasaka et al., 1997) and decomposition of carbon-containing molecules by chemical vapor deposition method (Nasibulin et al., 2005).

- Arc discharge method

This method is carried out in low pressure which sealed reaction chambers and vacuum equipment are needed to provide the atmosphere. An electric arc discharge is generated between two graphite electrodes under inert atmosphere of helium or argon. A very high temperature is obtained which allows the sublimation of the carbon. Two kinds of synthesis can be performed in the arc: evaporation of pure graphite (Tang et al., 2005) or co-evaporation of graphite and metal (Liu et al., 2004). Process parameters involve small gaps between electrodes, high current, plasma between the electrodes, voltages under specified electrode dimensions.

- Laser ablation method

This is known to produce CNTs with the highest quality and high purity of single-walled CNTs (Paradise et al., 2007). In this method, a rod of graphite as carbon source and a transition metal mixture is irradiated at its surface by laser under an inert atmosphere, leading to evaporation of the mixture. Then, carbon atoms dissolve and saturate in liquid droplets of the catalyst nanoparticles at high temperature, followed by the formation of CNTs. The process parameters which affect on the formation of CNTs by laser ablation method are type and concentration of catalyst in the rod, type and power of laser, temperature and pressure of the reaction system.

- Chemical vapor deposition (CVD) method

This method involves heating carbon-containing molecules as carbon source such as acetylene (Lee et al., 2002) and ethanol (Maruyama et al., 2005) and catalyst source, including a transition metal and organometallic complex such as metallocene at high temperatures over a period of time. The carbon-containing molecules are catalytically decomposed on the catalyst nanoparticles. After that, carbon atoms diffuse and dissolve into the catalyst nanoparticles until saturation and precipitation of the carbon atoms take place to form the tubes. The characteristics of the carbon nanotubes produced by CVD method depend on the working conditions such as type of carbon and catalyst source, temperature and pressure of the system, flow rate of carrier gas and reaction time.

Mechanisms of these methods consist of diffusion, dissolution, saturation and precipitation of carbon atoms in transition metal nanoparticle acts as catalyst, in particular Fe, Co and Ni. The catalyst nanoparticles are molten to form liquid droplets where the carbon atoms can dissolve in with specific carbon solubility, depending on type of the catalyst and form into metal carbide until the carbon atoms are equilibrium in liquid-solid phase with that catalyst. As supersaturation state of carbon atoms in the catalyst, precipitation of the carbon atoms on the surface of catalyst take place, leading to the formation of the CNTs (Dupuis, 2005).

2.2 Zinc Oxide (ZnO) nanostructures

2.2.1 Structure of ZnO

ZnO is a wide band gap (3.4 eV) II-VI compound semiconductor with white powder and nearly insoluble in water but soluble in acids or alkalis. It has a stable wurtzite (hexagonal) structure with lattice constants of a = 0.325 nm and c = 0.521 nm and consists of tetrahedral coordinated zinc and oxygen atoms as shown in Figure 2.3.
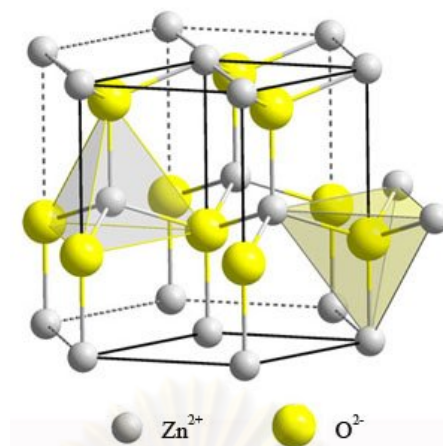
Figure 2.3 Wurtzite structure of ZnO.

http://www.thefullwiki.org/Wurtzite_(crystal_structure)

The tetrahedral coordination is also a common indicator of sp^3 covalent bonding nature. However, the Zn-O bond also possesses very strong ionic character and tends to increase the band gap beyond the one expected from the covalent bonding. Therefore, ZnO lies on the borderline between being classed as a covalent and ionic compound. Furthermore, the coordination gives rise to polar symmetry along the hexagonal axis. In such a polarity (non-centrosymmetric) structure, the center of positive charge and negative charge can be displaced due to external pressure induced lattice distortion. This displacement results in local dipole moment, thus a macroscopic dipole moment appears over the whole crystal, leading to characteristic piezoelectrical properties of ZnO.

2.2.2 Physical properties of ZnO nanostructure

The basic physical properties of bulk ZnO is shown in Table 2.3. It is worth noting that as the dimension of the semiconductor materials continuously shrinks down to nanometer or even smaller scale, some of their physical properties undergo changes known as the "quantum size effects", including mechanical, piezoelectric, electrical and optical properties.

Table 2.3 Physical properties of wurtzite ZnO (Pearton et al., 2003)

Properties	Value
Density	5.606 g/cm^3
Melting point	2248 K
Relative dielectric constant	8.66
Gap energy	3.4 eV, direct
Exciton binding energy	60 meV
Electron mobility (T = 300 K)	200 cm^2/V s
Hole mobility (T = 300 K)	5-50 cm^2/V s

ZnO is a relatively soft material with approximate hardness of 4.5 on the Mohs scale (Battez et al., 2008). Its elastic constants are smaller than those of relevant III-V semiconductors, such as GaN. The high heat capacity and heat conductivity, low thermal expansion and high melting temperature of ZnO are beneficial for ceramics (Port, 1991).

Piezoelectricity is also an important property. Among the tetrahedral bonded semiconductors, it has been stated that ZnO has a piezoelectric tensor equal to or even greater than that of GaN and AlN which means that ZnO is a suitable candidate for device applications requiring a large electromechanical coupling (Jagadish et al., 2006).

As a direct and large band-gap material, ZnO is attracting a lot of attention for a variety of electronic and optoelectronic applications. Advantages associated with a large band gap include higher breakdown voltages, ability to sustain large electric fields, lower noise generation, and high temperature and high-power operation (Özgür et al., 2005).

2.2.3 Synthesis of ZnO nanostructure

ZnO nanostructures which can be synthesized into a variety of morphologies including nanowires, nanorods, tetrapods, nanobelts, nanoflowers, nanoparticles and so on can be obtained via a variety of methods thermal evaporation, gas phase reaction and so on.

- Vapor transport synthesis process

The most common process to synthesize ZnO nanostructures utilizes a vapor transport process. In such a process, Zn vapor and oxygen source such as oxygen gas, CO and CO_2 react with each other to form ZnO nanostructures. There are several methods to generate Zn and oxygen source for the formation of ZnO nanostructures which can be categorized into following these methods.

Oxidation of Zn method, Zn powder is heated up under oxygen flow. After that, zinc vapor is oxidized to form ZnO nanostructure. Although this facilitates relative low temperature (500~700 °C), partial pressure of vaporized zinc and oxygen must be controlled carefully in order to obtain desired ZnO nanostructure. It has been observed that changing of their pressures contributes to a large variation on the morphology of nanostructure (Chang et al., 2004).

Thermal evaporation of ZnO method, decomposition of ZnO powder is direct method. However, it is limited to very high temperature (1400 °C) due to high decomposition temperature of ZnO powder (Li, Tand, and Wang, 2009).

Carbothermal reduction of ZnO method, this method is nearly the same as thermal evaporation of ZnO method. However, graphite powder as reducing agent is mixed with ZnO powder, leading to lower decomposition temperature. At about 800-1100 °C, graphite reduces ZnO to form Zn, CO and CO_2 vapors. Finally, Zn, CO and CO_2 will react to form ZnO nanostructures (Song et al., 2008).

According to the difference on nanostructure formation mechanisms, the extensively used vapor transport process can be categorized into the catalyst free vapor-solid (VS) process and catalyst assisted vapor-liquid-solid (VLS) process.

For catalyst free VS process, The Zn atoms were continuously evaporated from the source material during the heating process. In the presence of oxygen, the Zn vapors absorbed on the surface of quartz tube and react with oxygen to form ZnO nuclei. As the reactant concentration increases, the ZnO nuclei individually grow in upward direction in the form of nanostructures. In contrast, catalyst assisted VLS process; the source vapor (Zn vapor) reacted with the metal particles, which act as catalyst and from alloy droplets. After reaching at the supersaturation state, the grown droplets lead to the formation of nanostructures. The typical characteristic of VLS process is the presence of metal particles capped at the end of grown structures.

- Other synthesis processes

Although the vapor transport process is the dominant synthesis method for growing ZnO nanostructures, other growth methods such as electro-deposition and sol-gel have been developed in parallel. These methods provide the possibility of forming ZnO nanostructures at low temperature.

In an electro-deposition method (Li, Cheng, and Zhang, 2000), AAM (anodic alumina membrane) with highly ordered nanopores was used as a template. Zinc nanowires were fabricated into the nanopores via electro-deposition, forming zinc nanowires array. Then the nanowire array was oxidized at 300 °C for 2 hours and ZnO nanowire array was obtained.

In a sol-gel synthesis method (Lakshmi, Dorhout, and Martin, 1997), AAM was also used as the template and immersed into suspension containing zinc acetate for 1 minute, then heated in air at 120 °C for 6 hours. ZnO nanofibers were eventually obtained after removing the AAM template. This sol-gel process was further improved by an electrochemical method in order to obtain nanorods with diameter smaller than 50 nm.

These methods are complementary to the vapor transport synthesis of ZnO nanostructure, and also employ less rigorous synthesis conditions and provide great potential for device applications.

2.3 Composite material (Kaw, 2005)

A composite material is a structural material that consists of two or more combined constituents that are combined at a macroscopic level and are not soluble in each other. One constituent is called the reinforcing phase and the one in which it is embedded is called the matrix. The reinforcing phase material may be in the form of fibers, particles, or flakes. The matrix phase materials are generally continuous. Composites are classified by the geometry of the reinforcement or by the type of matrix as shown below.

- *Particulate composites* consist of particles immersed in matrices such as alloys and ceramics. They are usually isotropic because the particles are added randomly. Particulate composites have advantages such as improved strength,

increased operating temperature, oxidation resistance and so on. Typical examples include use of aluminum particles in rubber, silicon carbide particles in aluminum and gravel, sand and cement to make concrete.

- *Flake composites* consist of flat reinforcements of matrices. Typical flake materials are glass, mica, aluminum, and silver. Flake composites provide advantages such as high out-of-plane flexural modulus, higher strength, and low cost. However, flakes can not be oriented easily and only a limited number of materials are available for use.

- *Fiber composites* consist of matrices reinforced by short (discontinuous) or long (continuous) fibers. Fibers are generally anisotropic and examples include carbon and aramids. Examples of matrices are resins such as epoxy, metals such as aluminum, and ceramics such as calcium-alumino silicate.

- *Nanocomposites* consist of materials that are of the scale of nanometers. The accepted range to be classified as a nanocomposite is that one of the constituents is less than 100 nm. At this scale, the properties of materials are different from those of the bulk material. Generally, advanced composite materials have constituents on the microscale. By having materials at the nanometer scale, most of the properties of the resulting composite material are better than the ones at the microscale. Not all properties of nanocomposites are better, in some cases, toughness and impact strength can decrease.

2.4 Differential Mobility Analyzer (DMA)

Depending on the location where nucleation and growth of the synthesized nanoparticles by gas phase reaction take place, these synthesis processes can be divided into two categories; (i) supported nanoparticles on substrates and (ii) floating nanoparticle synthesis process. In the supported nanoparticle synthesis process, the synthesized nanoparticles are supported on a substrate such as single-walled carbon nanotubes (SWCNTs) can be produced by the supported catalyst process such as the supergrowth technique (Futaba et al., 2005). Conversely, in the floating nanoparticle synthesis process usually referred to as aerosol synthesis process,

the synthesized nanoparticles are suspended in the gas stream through out the formation.

In case of the floating nanoparticle synthesis process, an important physical parameter for characterizing the behavior of these particles is the size. It is therefore desirable to measure and classify the size of the particles and to yield monodisperse particles to gain understanding of the particle dynamics and control particle contamination. Among the various methods developed for the analysis of nanometer aerosol particles, differential mobility analyzer (DMA) has become the most common instrument widely used for classifying and generating monodisperse particles such as combination of laser ablation and electrostatic classification could provide a narrow size range of multi-walled carbon nanotubes (MWCNTs) and generated monodisperse MWCNTs from acetylene/hydrogen mixture using the monodisperse nickel nanoparticles (Kim and Zachariah, 2007).

A typical setup of a general DMA shown in Figure 2.4 consists of two concentric metal electrodes with the inner electrode maintained at a controlled negative voltage, in range of 1 V and 10 kV, while the outer electrode is electrically grounded, leading to creation of an electric field between these electrodes.
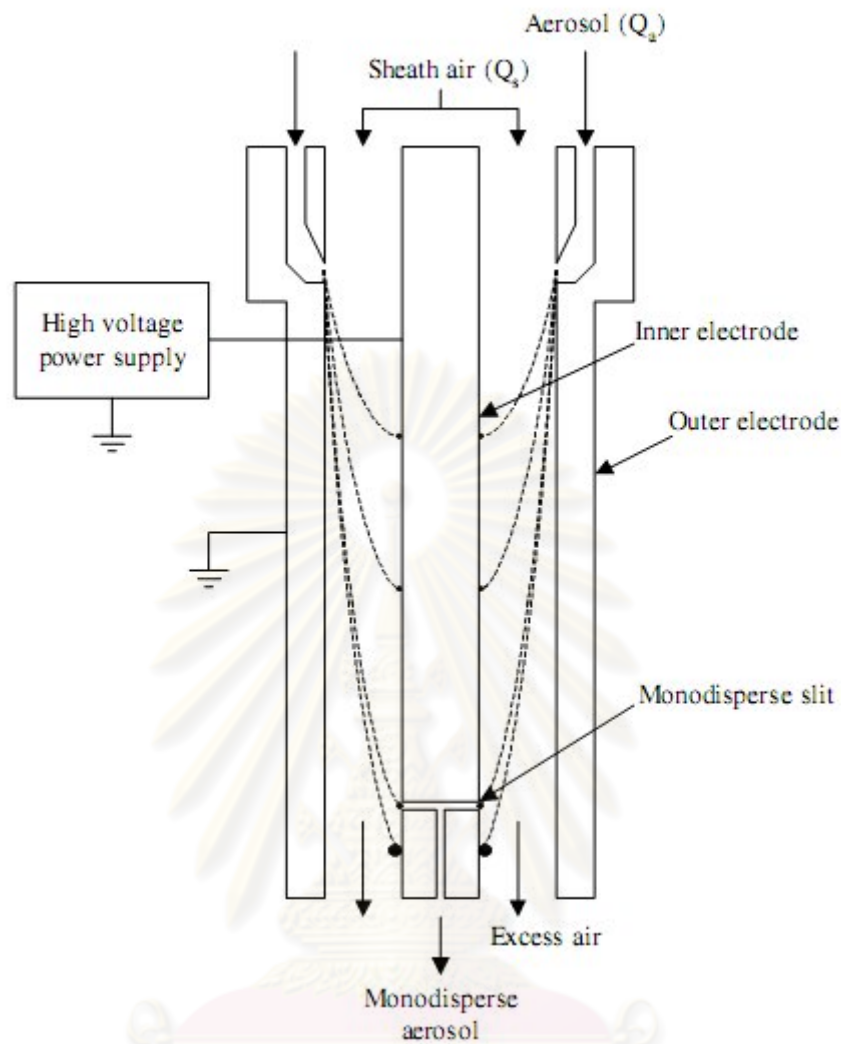
Figure 2.4 Differential Mobility Analyzer (DMA) for classifying and generating monodisperse aerosol particles (Intra, and Tippayawong, 2008)

The polydisperse charged aerosol (Q_a) and particle-free sheath air (Q_s) are introduced at the top of the DMA and flow down the annular space between the electrodes. The aerosol surrounds the inner core of sheath air, and both flows pass down the annulus with no mixing of the two laminar streams. The electric field causes positively charged particles to be attracted through the sheath air to the negative charged inner rod. Particles are collected along the length of the inner rod. The location of the collecting particles depends on the particle electrical mobility (Z_p), the fluid flow rate, and the DMA geometry. The electrical mobility of the collected particles is a function of the dimensions of the DMA, the applied voltage, and the fluid flow rate as shown in equation 2.2 proposed by Knutson, and Whitby (1975).

$$Z_p = \frac{(Q_s + Q_a)\ln(R_2 / R_1)}{2\pi LV} \qquad (2.2)$$

where

Z_p = Electrical mobility of the collected particles

R_1 = Radius of the inner electrode

R_2 = Radius of the outer electrode

L = Length of electrode

V = Applied voltage

From Stokes' law, the electrical mobility is related to particle diameter (d_p) as shown in equation 2.3

$$d_p = \frac{neC_c}{3\pi\mu Z_p} \qquad (2.3)$$

where

n = Number of elementary charge units

e = Elementary unit of charge (1.61×10^{-19} C)

C_c = Cunningham slip correction factor

μ = Gas viscosity

The Cunningham slip correction factor is a function of the particle Knudsen number (K_n) proposed by Cunningham, 1910 shown in equation 2.4.

$$C_c = 1 + K_n \left[1.257 + 0.4\exp(-1.1/K_n)\right] \qquad (2.4)$$

where

$$K_n = \frac{2\lambda}{d_p}$$

Particles with a high electrical mobility are collected along the upper portion of the rod. Particles with a low electrical mobility are collected on the lower portion of the rod. Particles with narrow range of electrical mobility exit with the monodisperse air flow through a small slit located at the bottom of the inner rod.

These particles are transferred to a particle counter to determine the particle number concentration such as condensation particle counter (CPC). The remaining particles are exhausted out as excess air flow. The size distribution is obtained by varying the applied voltage.

2.5 Gibbs free energy of reaction (Gaskell, 1981)

The Gibbs free energy (ΔG) of a reaction is a measure of the thermodynamic driving force that makes a reaction occurs. A negative value for ΔG indicates that a reaction can proceed spontaneously without external inputs, while a positive value indicates that it will not. The equation for Gibbs free energy of the reaction is shown in equation 2.5.

$$\Delta G = \Delta H - T\Delta S \tag{2.5}$$

where ΔH = Enthalpy of the reaction

                     ΔS = Entropy of the reaction

                     T = Temperature of the reaction

The enthalpy (ΔH) is a measure of the actual energy that is liberated when the reaction occurs (the heat of reaction). If it is negative, then the reaction gives off energy (exothermic reaction), while if it is positive the reaction requires energy (endothermic reaction). The entropy (ΔS) is a measure of the change in the possibilities for disorder in the products compared to the reactants. For example, if a solid (an ordered state) reacts with a liquid (a somewhat less ordered state) to form a gas (a highly disordered state), there is normally a large positive change in the entropy for the reaction.

2.6 Reaction equilibrium in a system containing condensed phases and a gaseous phase (Gaskell, 1981)

Consider the reaction equilibrium between a pure solid metal M, its pure oxide MO and O_2 at the temperature T and the pressure P as shown in equation 2.6.

$$M\,(s) + \frac{1}{2}\,O_2\,(g) = MO\,(s) \tag{2.6}$$
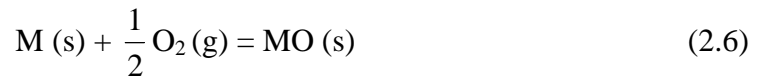
It is considered that O_2 is insoluble in the solid metal. Both the metal M and the oxide MO exist as vapor species in the gas phase, as is required by the criteria for phase equilibria,

$$\bar{G}_M \text{ (in the gas phase)} = G_M \text{ (in the solid metal phase)} \tag{2.7}$$

$$\bar{G}_{MO} \text{ (in the gas phase)} = G_{MO} \text{ (in the solid metal phase)} \tag{2.8}$$

Therefore, reaction equilibrium is established in the gas phase. The equilibrium of interest is thus

$$M\,(g) + \frac{1}{2}\,O_2\,(g) = MO\,(g) \tag{2.9}$$
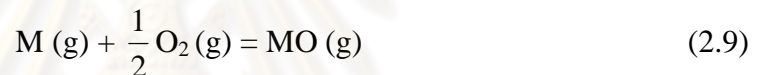
The free energy of the reaction can be written as in equation 2.10

$$G^{\circ}_{MO(g)} - \frac{1}{2}G^{\circ}_{O_2(g)} - G^{\circ}_{M(g)} = -RT\ln\frac{p_{MO}}{p_M\,p^{\frac{1}{2}}_{O_2}} \tag{2.10}$$

or
$$\Delta G^{\circ} = -RT\ln\frac{p_{MO}}{p_M\,p^{\frac{1}{2}}_{O_2}}$$

where ΔG° = Difference between the free energy of 1 mole of gaseous MO at 1 atm pressure, and the sum of the free energies of a half of 1 mole of O_2 at 1 atm pressure and 1 mole of gaseous M at 1 atm pressure, all at the temperature T

p_{MO} = Equilibrium vapor pressure of solid MO at the temperature of T

p_M = Equilibrium vapor pressure of solid M at the temperature of T

p_{O_2} = Equilibrium pressure of O_2 at the temperature of T

Equation 2.7 and 2.8 can be written as equation 2.11 and 2.12, respectively.

$$G^{\circ}_{M(g)} + RT \ln p_{M(g)} = G^{\circ}_{M(s)} + \int_{P=1}^{P=p_{M(g)}} V_{M(s)} dP \qquad (2.11)$$

$$G^{\circ}_{MO(g)} + RT \ln p_{MO(g)} = G^{\circ}_{MO(s)} + \int_{P=1}^{P=p_{MO(g)}} V_{MO(s)} dP \qquad (2.12)$$

where $G^{\circ}_{M(g)}$ = Molar free energy of the gaseous M under a pressure of 1 atm and the temperature T

$G^{\circ}_{M(s)}$ = Molar free energy of the solid M under a pressure of 1 atm and the temperature T

$G^{\circ}_{MO(g)}$ = Molar free energy of the gaseous MO under a pressure of 1 atm and the temperature T

$G^{\circ}_{MO(s)}$ = Molar free energy of the solid MO under a pressure of 1 atm and the temperature T

$V_{M(s)}$ = Molar volume of the solid M at the pressure of P and the temperature of T

$V_{MO(s)}$ = Molar volume of the solid MO at the pressure of P and the temperature of T

It is to be noted that the value of the integral terms of $\int_{P=1}^{P=p_{M(g)}} V_{M(s)} dP$ and $\int_{P=1}^{P=p_{MO(g)}} V_{MO(s)} dP$ are small enough to be considered negligible. Therefore, equation 2.11 and 2.12 can be reduced into equation 2.13 and 2.14, respectively.

$$G^{\circ}_{M(g)} + RT \ln p_{M(g)} = G^{\circ}_{M(s)} \qquad (2.13)$$

$$G^{\circ}_{MO(g)} + RT \ln p_{MO(g)} = G^{\circ}_{MO(s)} \qquad (2.14)$$

Equation 2.10 can be written as shown in equation 2.15

$$G^{\circ}_{MO(s)} - \frac{1}{2}G^{\circ}_{O_2(g)} - G^{\circ}_{M(s)} = -RT\ln\frac{1}{p^{\frac{1}{2}}_{O_2}} \qquad (2.15)$$

or $\qquad\qquad\qquad\qquad \Delta G^{\circ} = -RT\ln K$

where $\qquad \Delta G^{\circ}$ = Standard free energy of reaction $M(s) + \frac{1}{2}O_2(g) = MO(s)$

$\qquad K \quad = \dfrac{1}{p^{\frac{1}{2}}_{O_2}}$

Thus in the case of reaction equilibria involving pure condensed phase and a gas phase, the equilibrium constant K can be written solely in terms of those species which occur only in the gas phase. ΔG° is a function only of temperature, then K is a function of temperature, and hence at any fixed temperature the establishment of reaction equilibrium occurs at a unique value of $p_{O_2} = p_{O_2\,(eq,T)}$.

If, at any temperature, T, the actual O_2 partial pressure in a closed metal-metal oxide-oxygen system is greater than $p_{O_2\,(eq,T)}$, then spontaneous oxidation of the metal will occur, thus consuming O_2 and decreasing the O_2 pressure in the gas phase. When the actual O_2 partial pressure has thus been lowered to $p_{O_2\,(eq,T)}$, then, provided that both solid phases are still present, the oxidation reaction ceases and equilibrium prevails. Similarly, if the O_2 partial pressure in a closed metal-metal oxide-oxygen system was originally less than $p_{O_2\,(eq,T)}$, then spontaneous reduction of the oxide would occur until $p_{O_2\,(eq,T)}$ was reached.

2.7 Ellingham diagram for oxides

Ellingham (1944) plotted the experimentally determined $\Delta G°$-T relationships for the oxidation of a series of metals. The general forms of the relationships approximated to straight lines over temperature ranges. The relations could thus be expressed by means of the simple equation as shown in equation 2.16

$$\Delta G° = A + BT \qquad\qquad (2.16)$$

where   A = Temperature-independent standard enthalpy change, $\Delta H°$

B = Negative of temperature-independent standard entropy change, $-\Delta S°$

The variation of $\Delta G°$ with T at constant total pressure is plotted for oxidation reactions of various metals such as Fe, Ni, Cr and Zn is known as an Ellingham diagram shown in Figure 2.5.
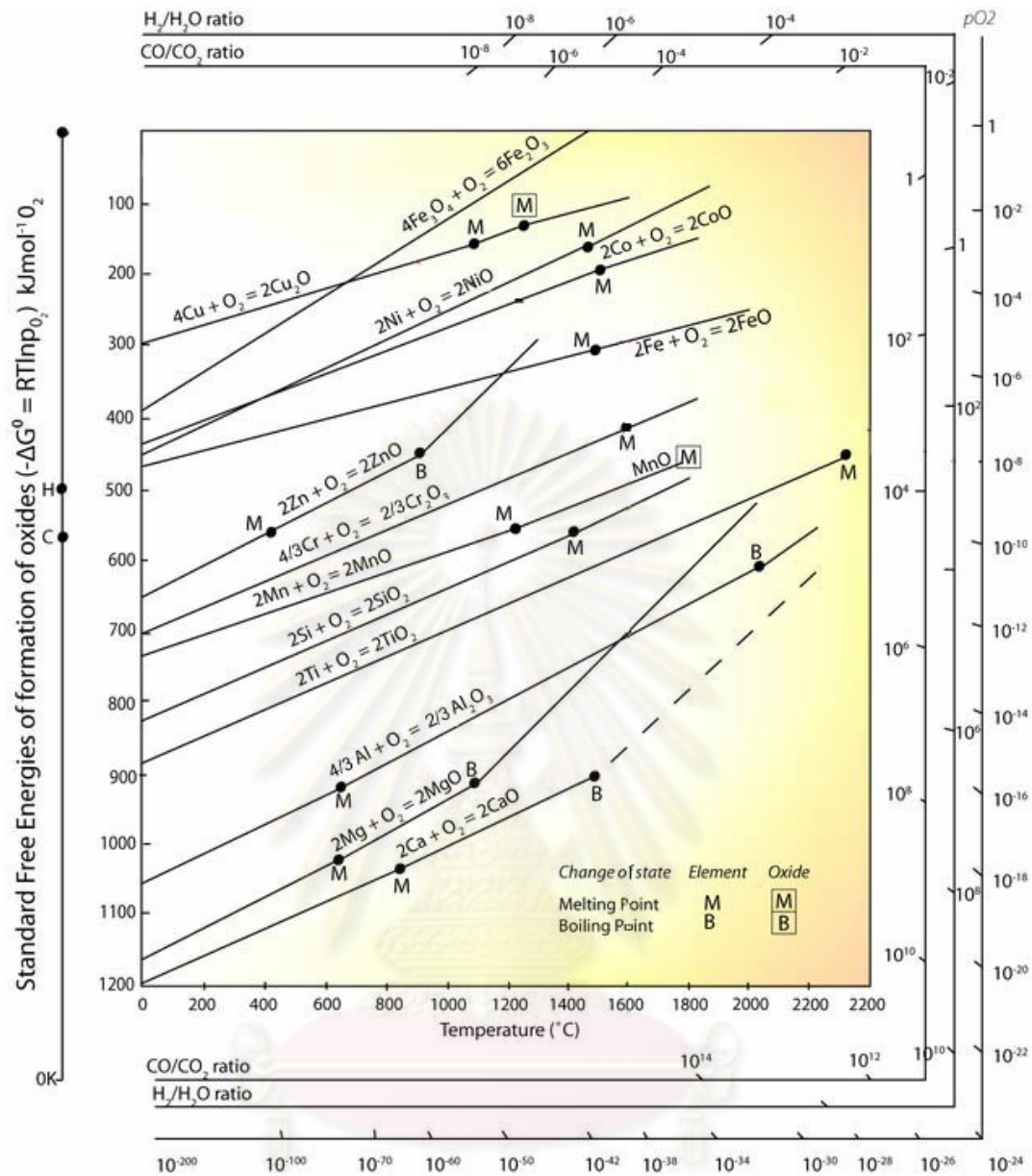
Figure 2.5 Ellingham diagram for metallurgical oxides.

(http://www.doitpoms.ac.uk/tlplib/ellingham_diagrams/ellingham.php)

From equation 2.16, ΔH^o is the intercept of the line with the $T = 0$ K axis, and ΔS^o is the negative of the slope of the line. As ΔS^o is a negative quantity, the line has a positive slope. The value of ΔG^o for an oxidation reaction is thus a measure of the chemical affinity of the metal for O_2, and the more negative the value of ΔG^o at any temperature, then the more stable the oxide.

2.8 Literature Reviews

2.8.1 Investigation of synthesis of the SWCNTs by laser ablation

Yudasaka et al. (1999) studied the formation of the SWCNTs by the Nd:YAG laser ablation of 3 different targets, including C/Ni/Co, C/Ni and C/Co. The target was placed at the center of a quartz tube reactor and then heated up to 1197 ℃. The Nd:YAG laser beam (wavelength of 532 nm, pulse width of 6-7 ns and frequency of 10 Hz) irradiated the target surface perpendicularly for 60 s under Ar flow. The results exhibited the yield of SWCNTs on the target composition with yields following the order C/Ni/Co > C/Ni >> C/Co. The SWCNT bundles formed when using target of C/Ni/Co is thicker and longer than those of C/Ni. The diameters of the SWCNTs when using C/Ni/Co target were larger and more uniform than those of C/Ni.

Yudasaka et al. (1997) synthesized SWCNTs by pulsed Nd:YAG laser ablation of C/Ni/Co target. The effects of the power of laser and the target composition on the formation of the SWCNTs were investigated. The target was heated up to 1200 ℃ under the optimum pressure and flow rate of 500-600 Torr and 0.2-0.5 L/min, respectively. The Nd:YAG laser beam (wavelength of 532 nm, pulse width of 7 ns, frequency of 10 Hz and power of 1.2 J/pulse) irradiated the target surface perpendicularly. The SWCNTs were formed when the power of the laser in a range of 1.1-4.4 W. However, the power was larger than 5.4 W, the quantity of the SWCNTs decreased dramatically. Decreasing of Ni and Co in the target composition provided increasing of the SWCNT yield with higher laser power.

Kataura et al. (2000) investigated the effect of furnace temperature on the formation of the SWCNTs by laser ablation of C/Ni/Co target. The target with Ni/Co of 0.45/0.45 at.% was inserted into the quartz tube reactor and then heated up in a range of 800-1350 ℃ under 500 Torr of Ar. After that, the Nd:YAG laser irradiated the target surface perpendicularly. At the furnace temperature of 800 ℃, the SWCNTs with a very small diameter were synthesized, but the abundance was very low. When the furnace temperature was increased, the SWCNTs were synthesized with high abundance and purity.

Detail of proposed reviews of the synthesis of the SWCNTs by Nd:YAG pulse laser ablation is summarized in Table 2.4.

2.8.2 Investigation of synthesis of the carbon nanoparticles by CVD

Charinpanitkul et al. (2009) studied synthesis of the carbon nanoparticles by CVD of naphthalene and ferrocene. A mixture of naphthalene and ferrocene with a constant ratio of 1:1 was loaded into a graphite boat and then inserted into a quartz tube reactor where the local temperature was kept above the vaporization temperature of the mixture. The reaction temperature was varied in a range of 800-1050ºC. The synthesized products were combination of carbon nanocapsules (CNCS) and MWCNTs. The increasing of temperature resulted in the enhance formation of CNCs with lower amount of the CNTs. The experimental results also revealed that the total yield of the products could be enhanced with the increased reaction temperature.

Musso et al. (2008) synthesized CNTs using CVD of camphor and ferrocene. The effect of temperature on the formation of the CNTs on crystalline silicon substrate was investigated. A mixture of camphor and ferrocene with a 20/1 mass ratio was prepared in a flask which connected to the quartz tube reactor. The substrate was inserted into a quartz tube reactor and then heat up in a range of 800-1000 ºC. Subsequently, the flask was heated up to 220 ºC, leading to the vaporization of the mixture, and the vaporized mixture were carried into the reactor by the flow of nitrogen. At a substrate temperature in the range of 650-900 ºC, a carpet of vertically oriented CNTs, with spare signs of other forms of carbon, was obtained on silicon substrate. On the other hand, the film grown on the silicon substrate in the temperature range of 950-1070 ºC showed the formation of a nanographite layer and carbon fibers.

Andrews et al. (1999) studied the formation of the MWCNTs by CVD of ferrocene-xylene mixture. The mixture of ferrocene and xylene was fed into a two-stage tubular quartz reactor using syringe pump. The liquid feed was then preheated to 175 ºC. At this temperature, the liquid was immediately vaporized and swept into the reaction zone of the furnace by flow of Ar. Various parameters, such as the furnace temperature (650-1050 ºC), ferrocene/xylene ratio and feed rate, total reaction time

and gas flow rate, were adjusted to determine the growth conditions for high purity aligned MWCNTs.

The results revealed that at 1050 ºC, a small amount of the MWCNTs was formed at the entrance of the furnace. However, when the reactor temperature was lowered to 675 ºC, copious amounts of aligned MWCNTs were produced. At a xylene partial pressure of 4 mbar, the MWCNTs were found only. However, at a higher xylene partial pressure of 20 mbar, amorphous carbons were observed only. At a Fe/C ratio of 0.75 at.% showed the presence of the Fe catalyst inside the core of the MWCNTs. Lowering the Fe/C ratio by a factor of 10 produced longer and thinner nanotubes and the Fe catalyst was absent inside the core of the tubes.

Detail of proposed reviews of the synthesis of the MWCNTs by CVD under atmospheric pressure is summarized in Table 2.5.

2.8.3 Investigation of synthesis of the ZnO nanoparticles by oxidation

Park et al. (2006) studied the growth of ZnO nanowires using few amount of oxygen. The ZnO nanowire has grown from metal Zn granule under controlled O_2 environments. The effects of oxygen concentration and temperature on the formation of the ZnO nanowires were investigated. The total flow rate of oxygen and nitrogen was controlled at 200 mL/min, while the oxygen concentration was adjusted from 0.5 to 5 vol%. The temperature was varied in a range of 700-1000 ºC. The ZnO nanowires became shorter when oxygen concentration was increased. ZnO nanorods became nanowires and needles when the temperature was varied from 700 to 800 and 900 ºC, respectively.

Umar et al. (2005) studied formation of ZnO nanorods with large quantity using metallic zinc powder and oxygen. A quartz boat of Zn was inserted into a quartz tube reactor and then heated up to the temperature ranges of 500-620 ºC under pressure of 3 Torr. Nitrogen and Oxygen flow rates were introduced into the system with their flow rates of 10 and 20 sccm, respectively. General morphologically studies indicated the as-grown products are flower-shaped containing several hundreds of nanorods. The obtained nanorods have a diameter of 150-250 nm while

their lengths are 5-10 µm. The detailed structural analysis revealed that the ZnO nanorods exhibit a single crystalline wurtzite phase containing very less structural defects.

Dai et al. (2002) synthesized tetrapod ZnO nanoparticles using oxidation reaction between pure Zn and oxygen. Alumina boat which loaded Zn was inserted in a horizontal tube furnace. The temperature of furnace was ramped to 825-925 °C at heating rate of 50-100 °C/min. From FE-SEM images, ZnO nanoparticles were a tetrapod shape having four legs with diameter 70-150 nm and length of legs was 2-3 µm. In detailed structure of individual ZnO was characterized by using TEM. From bright-field images, there was no streaking in the nanorod. From dark-field images, single crystal nature of nanorod was observed. Therefore, ZnO nanoparticles which use oxidations in gas phase were high-quality nanocrystal.

Wu and Xie (2004) studied about synthesis of ZnO nanoparticles using the oxidation reaction between Zinc vapor and oxygen at various temperatures (1050-1400 °C) and pressure (1-12 kPa). The powder Zn was vaporized by using inductive furnace. Firstly, Zn vapor contacted with argon atoms in the gas mixture because the molecular weight of argon atom is heavier than oxygen atom. Then, Zn vapor was condensed to Zn aerosol. In the same time, Zn aerosol reacted with oxygen atom to produced ZnO nanoparticles.

As-synthesis ZnO have four needle-like feet (tetrapod) with diameter of 6-45 nm and length 280-435 nm. While the temperature was raised, the diameter of ZnO increased and the length of ZnO decreased. The ZnO nanoparticles of different sizes were obtained in range of gas pressure at each evaporation temperature. For example at 1350 °C, the pressure was varied from 2.2 to 6 kPa and the nanowhiskers with longest needle-like feet were obtained at a pressure of 4 kPa. However, the spheroid nanoparticles were obtained out side this pressure range.

Detail of proposed reviews of the synthesis of the ZnO nanoparticles by oxidation is summarized in Table 2.6.

2.8.4 Investigation of synthesis of the ZnO/MWCNT composites

Chrissanthopoulos et al. (2007) reported synthesis of various ZnO nanostructures grown on multi-walled carbon nanotubes by thermal evaporation method. The influence of deposition time at 4, 8 and 15 min and substrate temperature at 850-900 ℃ were investigated. An equimolar zinc oxide and graphite was mixed and then put on boat placed at the closed end of a fused silica tube. The MWCNTs were used as received. The mixture was inserted for few minutes in a preheated (at ~1000 ℃) horizontal furnace, while the CNTs pellets were placed at various position at a temperature interval 850-950 ℃.

The experiment showed various structures such as polypods and nano-hedgehogs, depending on various factors as well as the location of the ZnO–CNT junction. Single, isolated nanorods appear to form at the end of a CNT.

Chen et al. (2006) presented zinc oxide nanoparticles decorated multi-walled carbon nanotubes. MWCNTs were prepared by the chemical catalytic vapor deposition process (CVD) of acetylene. The obtained MWCNTs were modified with citric acid, which were sonicated 30 min and refluxed at 80 ℃. Then, the mixture was filtered, washed and dried at 60 ℃. The ZnO/MWCNTs composites were prepared using a sol-gel method, in which zinc acetate was dissolved in anhydrous ethanol. Finally, the modified MWCNTs were added. The additions were accompanied by stirring and sonication. The temperature was maintained at 60 °C. Finally, the ZnO/MWCNTs precursor was dried at 70 ℃ and then calcined at 450, 600 and 750 ℃, respectively for 2 h under the protection of nitrogen.

The results reveal that the MWNT are decorated with ZnO particles. The average size of calcined ZnO at 450, 600 and 750 ℃ was about 11, 48 and 89 nm, respectively. Furthermore, the UV emission of MWCNTs was improved significantly through modification with ZnO.

Du, Hao, and Wang (2008) presented the preparation of floral-patterned ZnO/MWCNTs heterogeneity structure by using microwave irradiation heating method. Pristine nanotubes were refluxed in nitric acid at 140 °C for 4 h. Then, zinc acetate was added into the MWCNTs solution. The solution was placed in

a microwave oven with an outside refluxing system and irradiated for 2 min. Finally, the suspension was washed with ethanol and deionized water by centrifugation, then dried at 60 ℃ under air atmosphere.

It was found that the flower-like zinc oxide grows around the multi-walled carbon nanotubes to form a floral-patterned structure. Multi-walled carbon nanotubes play a role as a template for the growth of ZnO and they can link ZnO particles together as a complex fabrication. The flower-like zinc oxide is uniform and has an average diameter of 2 micron. The average length of flower petals is about 1 micron.

Jiang, and Gao (2005) studied the fabrication and characterization of ZnO-coated multi-walled carbon nanotubes with photocatalytic activity. MWCNTs were prepared by the catalytic decomposition of methane. The pristine nanotubes were dispersed in a dilute sodium dodecyl sulfate (SDS) aqueous solution by using the ultrasonication. ZnO nanoparticles were achieved via the reaction of zinc acetate and lithium hydroxide monohydrate in a hydrous ethanol medium. Ethanol solution containing Zn^{2+} and SDS-coated MWCNTs were refluxed at 80 °C for 3 h. Then, the mixture was boiled at 95 °C for 3 h. The final black product was rinsed repeatedly with ethanol and distilled water, and then vacuum dried at 60 °C for 12 h.

It can be observed that most of MWCNTs containing individual CNTs and CNT bundles have been covered with ZnO nanoparticle layers with an average size of ~6 nm. The composite shows enhanced photocatalytic degradation of methylene blue solution.

Detail of proposed reviews of the synthesis of the composite of ZnO and MWCNTs is summarized in Table 2.7.

Table 2.4 Literature reviews of the synthesis of the SWCNTs by Nd:YAG pulse laser ablation

Researcher	Target type	Target composition	Laser intensity	Ar flow rate	Temperature	Pressure	Experimental results
Yudasaka et al. (1999)	C/Ni/Co	0.0-4.5 % atom each of Ni and Co	1-6 W	0.5 L/min	1197 ºC	600 Torr	SWCNTs with yields following the order C/Ni/Co > C/Ni >>C/Co
	C/Ni	0.15-0.9 % atom of Ni					
	C/Co	0.6-9.0 % atom of Co					
Yudasaka et al. (1997)	C/Ni/Co	0.6-4.5 % atom each of Ni and Co	1.1-9.1 W	0.2-0.5 L/min	1200 ºC	500-600 Torr	SWCNTs at the laser intensity lower than 4.4 W
Kataura et al. (2000)	C/Ni/Co	0.45 % atom each of Ni and Co		1.2-12 mm/s	800-1350 ºC	500 Torr	Change in diameter distribution of SWCNTs at changing flow velocity

Table 2.5 Literature reviews of the synthesis of the MWCNTs by CVD under atmospheric pressure

Researcher	Carbon precursor	Catalyst precursor	Carbon/Catalyst molar ratio	Carrier gas flow rate	Temperature		Deposition time	Experimental results
					Preheater	Reactor		
Charinpanitkul et al. (2009)	Naphthalene	Ferrocene	20/1	N_2 rate of 0.12 L/min	-	800-1050 ºC	15 min	MWCNTs and Carbon naocapsules (CNCs)
Musso et al. (2008)	Camphor	Ferrocene	24/1	N_2 rate of 0.42 L/min	220 ºC	800-1100 ºC	20 min	Vertically aligned MWCNTs
Andrews et al. (1999)	Xylene	Ferrocene	15/1 with feed rate of 1-5 mL/h	$Ar + 0.1 \% H_2$ with total rate of 0.75-1.88 L/min	175 ºC	650-1050 ºC	120 min	Aligned MWCNTs

Table 2.6 Literature reviews of the synthesis of the ZnO nanoparticles by oxidation of Zn

Researcher	O_2 flow rate	Carrier gas flow rate	Temperature)	Pressure	Reaction time	Experimental results
Park et al. (2006)	1-10 mL/min	190-199 mL/min	700-1000 ºC	760 Torr		ZnO nanowire, nanorod, nanoneedle
Umar et al. (2005)	20 mL/min	N_2 rate of 10 mL/min	500-620 ºC	3 Torr	60-90 min	Flower-shaped ZnO containing several hundreds of nanorods
Dai et al. (2002)			825-925 ºC	760 Torr	1-30 min	ZnO tetrapod
Wu et al. (2004)	25 mL/min	Ar rate of 25 mL/min	1050-1400 ºC	7.5-90 Torr	15 min	ZnO nanowhisker

Table 2.7 Literature reviews of the synthesis of the ZnO/MWCNT composite

Researcher	CNTs			Fabrication of ZnO on the CNTs		Experimental results
	Method	Synthesizing temperature	N_2 flow rate	Method	Synthesizing temperature	
Chrissanthopoulos et al. (2007)	Commercial grade	-	-	Carbothermal reduction of ZnO	1000 ºC	Single, isolated ZnO nanorod on the end of a MWCNT.
Chen et al. (2006)	CVD of acetylene	700 ºC	0.24 L/min	Sol-gel of zinc acetate	60 ºC	MWCNT decorated with ZnO particles
Du et al. (2008)	Commercial grade	-	-	Sol-gel of zinc acetate		Flower-like ZnO grown around the multi-walled carbon nanotubes
Jiang et al. (2005)	Commercial grade	-	-	Sol-gel of zinc acetate	80 ºC	MWCNTs covered with ZnO nanoparticle

CHAPTER III

EXPERIMENT

Referring to the objective of this work, the synthesized particulate composites of ZnO and carbon nanoparticles by single-step gas phase reaction were required. Within the gas phase reaction of the composites, the composites were expected to be combinantion of the ZnO and carbon nanoparticles. However, the combination of those major compounds for the formation of the composites was found to be more complexity than both isolated synthesis of the ZnO nanoparticles and carbon nanoparticles due to complex thermochemical oxidation at high temperature range of related elements in the system including Zn, C and Fe.

For controlling the formation of the composites, both of isolated synthesis of the ZnO nanoparticles and carbon nanoparticles were investigated before the synthesis of the composites. The carbon nanoparticles, especially MWCNTs with high purity, were synthesized by CVD of glycerol and ferrocene. Furthermore, to truly understand the formation of the MWCNTs, parallel study of synthesis of SWCNTs by laser ablation was revealed. While, the ZnO nanoparticles were synthesized by oxidation of pure Zn. After the studies of the isolated synthesis of the SWCNTs, MWCNTs and ZnO nanoparticles, the ZnO/MWCNT composites were then investigated under controlling conditions for decrease in the thermochemical oxidation of undesired products.

Therefore, experiment of this work were separated into 4 parts including the synthesis of SWCNTs by laser ablation, the synthesis of carbon nanoparticles by CVD of glycerol and ferrocene, the synthesis of ZnO nanoparticles by oxidation of Zn and the synthesis of composites of ZnO/MWCNT composites by gas phase reaction. Various parameters which affected on the synthesis of each part were carefully investigated.

3.1 Synthesis of the SWCNTs by laser ablation

3.1.1 Raw materials and experiment

C/Ni/Co target rod (Toyo Tanso Company) with a diameter of 6 mm and length of 30 mm prepared from particulate mixture of carbon and 0.6% atomic of nickel and cobalt, respectively was used as C, Ni and Co sources of this work, respectively as shown in Figure 3.1.

Figure 3.1 C/Ni/Co target rod.

The SWCNTs were synthesized by pulsed Nd:YAG laser ablation of the C/Ni/Co target rod within a quartz tube reactor which is schematically shown in Figure 3.2. The experimental set up consists of an electrical furnace, a quartz tube (outer diameter of 28 mm, inner diameter of 25 mm and length of 700 mm), a mass flow controller (MFC), a pressure transducer, a vacuum pump, and a rotating motor with a speed of 7 rpm.
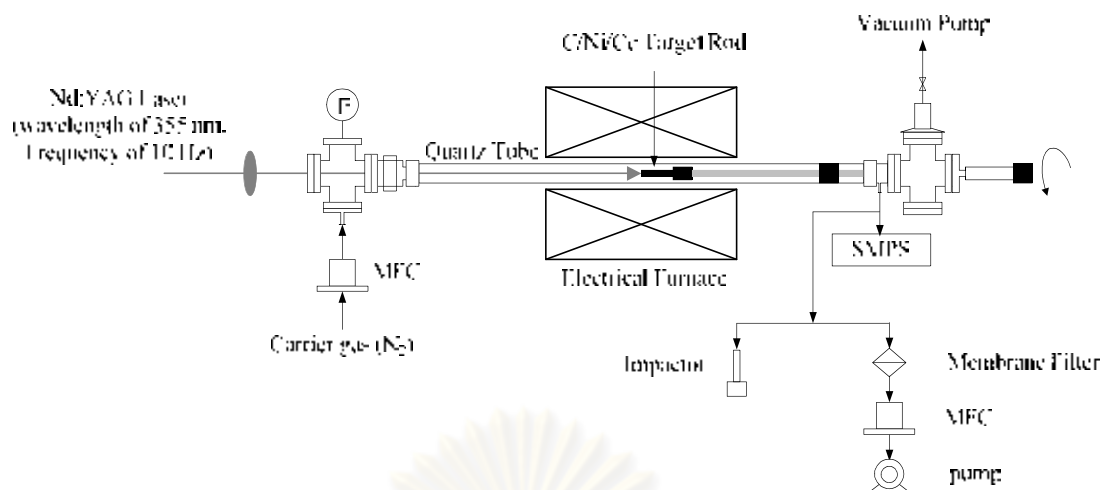
Figure 3.2 Schematic diagram of experimental apparatus for aerosol generation of the SWCNTs by pulsed Nd:YAG laser ablation.

Before the laser ablation, the C/Ni/Co target rod was heated to a desired temperature. The Nd:YAG laser beam (wavelength of 355 nm, repetition rate of 10 Hz, pulse width of 10 ns) with desired laser power irradiated perpendicularly to the target surface which was steadily rotated for uniform ablation. All experiments were carried out under atmospheric pressure and nitrogen flow rate of 1.5 L/min. The airborne products were collected on a polycarbonate membrane filter (filter size of 25 mm and pore size of 100 nm, ADVANTEC) for characterizing their morphology and crystallinity by Scanning Electron Microscope and Raman Spectroscope, respectively. The detailed morphology of the synthesized SWCNTs was analyzed by a Transmission Electron Microscopy. The TEM specimens were prepared by depositing aerosol on a TEM microgrid (200 mesh) using an impactor. Furthermore, the size distribution of the airborne SWCNTs was also determined by a computer controlled Scanning Mobility Particle Sizer (SMPS) system equipped with a Differential Mobility Analyzer and a Condensation Particle Counter.

3.1.2 Experimental procedures

The experimental procedures of this work were separated into 2 parts as following;

3.1.2.1 Variation of laser intensity

In this part, effect of laser intensity was investigated on morphology, particle size distribution and crystallinity of the synthesized carbon nanoparticles at the laser intensity of 0.4, 0.5 and 0.6 W. The experiments were fixed at temperature of 25 ℃ under atmospheric pressure and nitrogen flow rate of 1.5 L/min.

3.1.2.2 Variation of temperature

Referring to many previous reports, the temperature could affect on the formation of the SWCNTs including their quality and quantity. Therefore, in this part, effect of temperature on the morphology, size distribution and crystallinity of the synthesized SWCNTs was studied at the reaction temperature of 25, 200, 400, 600, 800, 1000 and 1080 ℃. It should be noted that the temperature was controlled not higher than 1080 ℃ due to limitation of the electrical furnace. The dimensions (diameter and length) of the monodispersed SWCNTs by DMA with mobility-based diameters of 100 and 200 nm were also analyzed by SEM. The experiments were controlled under laser intensity of 0.6 W, atmospheric pressure and nitrogen flow rate of 1.5 L/min.

3.2 Synthesis of the carbon nanoparticles by CVD of glycerol and ferrocene

3.2.1 Raw materials and experiment

In this work, glycerol (Ajax Chemicals) and ferrocene (Sigma-Aldrich) were used as sources of carbon and iron catalyst for the synthesis of the carbon nanoparticles by CVD, respectively. Boiling points of glycerol and ferrocene are 290 and 249 ℃, respectively. Experimental set up shown in Figure 3.3 consists of an

electrical furnace, a quartz tube reactor with inner diameter of 34 mm and length of 600 mm, a boat of glycerol-ferrocene mixture, silicone stoppers and a dust collector.
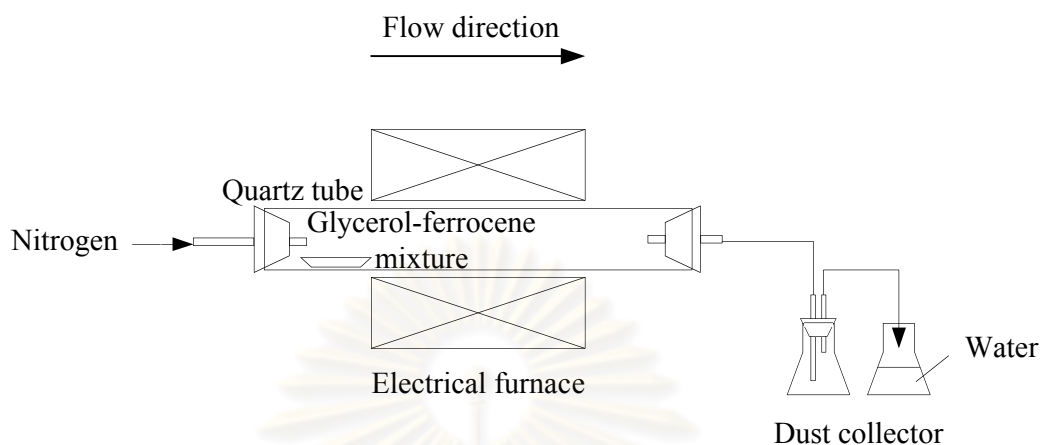
Figure 3.3 Experimental set up for synthesizing carbon nanoparticles by CVD of glycerol and ferrocene.

Glycerol and ferrocene were mixed with desired molar ratio and loaded into the boat. After that, the boat of the glycerol-ferrocene mixture was inserted inside the tube reactor at position of 5 cm from inlet of the reactor. From temperature profile as shown in Appendix A, it could be assured that temperature of the position of 5 cm from the inlet was high enough for vaporization of the mixture of glycerol-ferrocene. Before heating the furnace up, residual air inside the tube reactor was eliminated by supplying nitrogen gas with flow rate of 200 mL/min for 20 min. The furnace was then heated up until desired temperature under controlling desired nitrogen flow rate. The process was controlled for 1 hr. The tube was then naturally cooled down to room temperature. The synthesized black products on inner wall of the tube reactor were kept and characterized their morphology, crystallinity and phase.

3.2.2 Experimental procedures

The experimental procedures of this work were separated into 3 parts as following;

3.2.2.1 Variation of nitrogen flow rate

Referring to many previous reports, the nitrogen flow rate could affect on the formation of the carbon nanoparticles including their quality and quantity. In this part, the nitrogen flow rate was found to be controlled not higher than 500 mL/min because, at the nitrogen flow rate higher than 500 mL/min, the carbon nanoparticles could not be formed on inner wall of the quartz tube reactor. Therefore, effect of nitrogen flow rate on the morphology, crystallinity and yield of the synthesized carbon nanoparticles was investigated by varying flow rate at 50, 200, 350 and 500 mL/min under the same condition of synthesizing temperature of 800 ℃ and glycerol to ferrocene molar ratio of 5 to 1.

3.2.2.2 Variation of synthesizing temperature

From preliminary study, it should be noted that, at the synthesizing temperature lower than 800 ℃, some of vaporized glycerol could not be decomposed and then condensed into liquid droplets of glycerol and deposited on inner wall of the quartz tube reactor. However, the synthesizing temperature could not be controlled higher than 900 ℃ due to limitation of the electrical furnace and, especially poisoning from the silicone stoppers. Therefore, in this part, the effect of synthesizing temperature on the morphology, crystallinity and yield of the synthesized carbon nanoparticles was studied at 800, 850 and 900 ℃. The nitrogen flow rate and glycerol to ferrocene molar ratio were fixed at 350 mL/min and 5/1, respectively.

3.2.2.3 Variation of glycerol to ferrocene molar ratio

In this part, the effect of glycerol to ferrocene molar ratio on the quality and quantity of the synthesized carbon nanoparticles was studied by varying the molar ratio in a range of 5/1, 10/1 and 20/1 under the same condition of synthesizing temperature of 800 ℃ and nitrogen flow rate of 350 mL/min.

3.3 Synthesis of the ZnO nanoparticles by oxidation of Zn

3.3.1 Raw materials and experiment

In this work, zinc powder (Sigma-Aldrich, purity > 98%) with its boiling point of 907 ℃ was used as Zn source for the synthesis of the ZnO nanoparticles by oxidation of the Zn. Experimental set up for the synthesis of the ZnO nanoparticles shown in Figure 3.4 was modified from the experimental set up for the synthesis of the carbon nanoparticles as shown in Figure 3.3 by changing position of a boat of Zn powder to 15 cm from the inlet and adding oxygen to react with vaporized Zn to form ZnO nanoparticles.
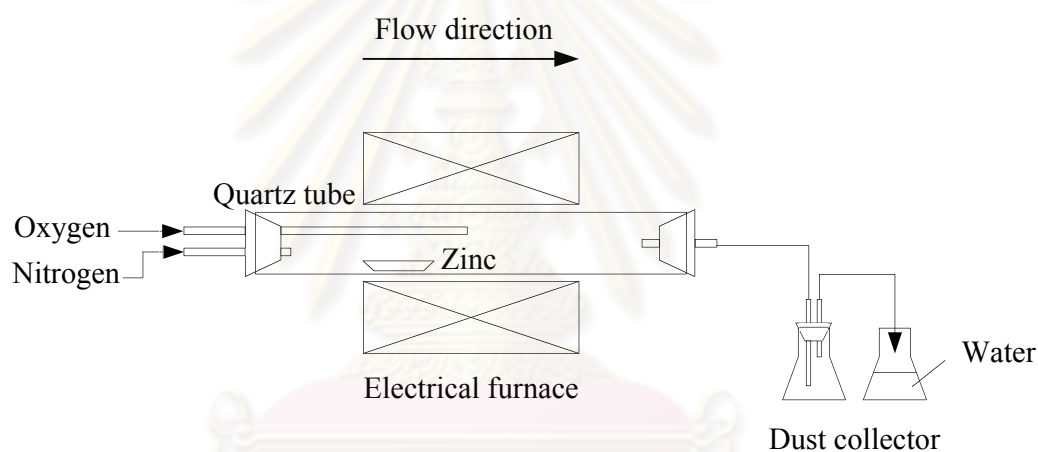
Figure 3.4 Experimental set up for synthesizing ZnO nanoparticles by oxidation of Zn.

Zinc powder was loaded into the boat and inserted inside the tube reactor at position of 15 cm from the inlet. From temperature profile as shown in Appendix A, it could be also assured that temperature of the position of 15 cm from the inlet was high enough for evaporization of the Zn powder. Before heating the furnace up, residual air inside the tube reactor was eliminated by supplying nitrogen gas with flow rate of 200 mL/min for 20 min. The furnace was then heated up until desired temperature under controlling desired nitrogen and oxygen flow rates. The process was controlled for 1 hr. The tube was then naturally cooled down to room temperature. The synthesized white products on inner wall of the tube reactor were kept and characterized their morphology, size and phase.

3.3.2 Experimental procedures

Because of the objective of this work was to synthesize the ZnO/MWCNT composites. Therefore, various parameters including the nitrogen flow rate and synthesizing temperature which also affected on the formation of the ZnO nanoparticles were also controlled as same as those for the isolated synthesis of the carbon nanoparticles by CVD.

3.3.2.1 Variation of nitrogen flow rate

In this part, effect of nitrogen flow rate on the morphology, size and yield of the synthesized ZnO nanoparticles was investigated by varying flow rate at 200, 350 and 500 mL/min under the same condition of synthesizing temperature of 800 ºC and oxygen flow rate of 100 mL/min. From preliminary study, it should be noted that the oxygen flow rate could not be controlled lower than 100 mL/min due to not enough for the formation of the ZnO nanoparticles.

3.3.2.2 Variation of synthesizing temperature

Effect of synthesizing temperature on the morphology, size and yield of the synthesized ZnO nanoparticles was studied in a range of 800, 850 and 900 ºC. The nitrogen and oxygen flow rates were fixed at 500 and 100 mL/min, respectively.

3.3.2.3 Variation of oxygen flow rate

Referring to many previous reports, the oxygen flow rate could affect on the formation of the ZnO nanoparticles including their quality and quantity. From preliminary study, the oxygen flow rate was found to be controlled not lower than 100 mL/min. When preliminary study of thermodynamics was investigated, the oxygen flow rate was considerably controlled not higher than 150 mL/min for avoiding thermochemical oxidation of Zn, C, Fe elements within the system of the composite synthesis. Therefore, in this part, effect of oxygen flow rate on the formation of the synthesized ZnO nanoparticles was studied in at the rate of 100 and 150 mL/min

under the same condition of N_2 flow rate of 500 mL/min and synthesizing temperature of 800 ℃.

3.4 Synthesis of the ZnO/MWCNT composites by gas phase reaction

3.4.1 Raw materials and experiment

Raw materials of this work were glycerol, ferrocene and Zn powder as C, Fe and Zn sources. Experimental set up for the synthesis of the composites shown in Figure 3.5 was combined from the experimental set up for the synthesis of the carbon nanoparticles as shown in Figure 3.3 and the experimental set up for the synthesis of the ZnO nanoparticles as shown in Figure 3.4.
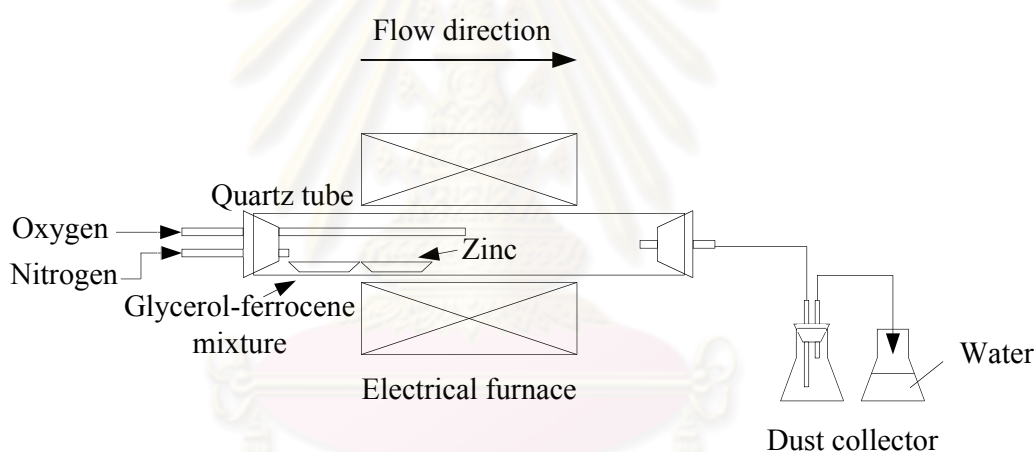
Figure 3.5 Experimental set up for synthesizing ZnO/MWCNT composites.

Glycerol-ferrocene mixture and Zn powder were loaded into separated boats and then inserted inside the quartz tube reactor at position of 5 and 15 cm from the inlet, respectively. Before heating the furnace up, residual air inside the tube reactor was eliminated by supplying nitrogen gas with flow rate of 200 mL/min for 20 min. The furnace was then heated up until desired temperature under nitrogen and oxygen flow rates of 500 and 100 mL/min, respectively. The process was controlled for 1 hr. The tube was then naturally cooled down to room temperature. The synthesized gray products on inner wall of the tube reactor were kept and characterized their morphology and size and phase.

3.4.2 Experimental procedures

In this part, thermodynamic data for oxidation of related elements including Zn, C and Fe was firstly investigated by using Ellingham diagram. From the diagram, the synthesizing temperature of 800 and 900 ℃ was carefully considered to be major parameter for the synthesis of the composites under controlling of the nitrogen flow rate, oxygen flow rate and glycerol to ferrocene molar ratio at 500 mL/min, 100 mL/min and 5/1, respectively.

3.5 Analytical instruments

The instruments were used to characterize morphology, structure, and phase of the synthesized carbon nanoparticles, ZnO nanoparticles and their composites are Scanning Electron Microscope (SEM), Transmission Electron Microscope (TEM), and X-Ray Diffraction (XRD), respectively. Purity and crystallinity of the synthesized carbon nanoparticles were characterized by Raman Spectroscope, while size distribution and classification of the synthesized airborne SWCNTs were investigated by Scanning Mobility Particle Sizer (SMPS). The composites were further characterized their absorption, elements and boding by UV-Visible Spectrophotometer (UV-Vis), Energy Dispersive X-Ray Spectroscopy and Fourier Transform Infrared Spectrophotometer, respectively to confirm their structures.

3.5.1 Scanning Electron Microscopy (SEM)

Morphology and size of the synthesized carbon nanoparticles, ZnO nanoparticles and their composites were investigated by SEM (Hitachi, model S4500 and JEOL model JSM-6400).

3.5.2 Transmission Electron Microscope (TEM)

Structure of the synthesized carbon nanoparticles, ZnO nanoparticles and their composites were investigated by TEM (JEOL model JEM 2100).

3.5.3 Raman Spectroscope

Purity and crystallinity of the synthesized carbon nanoparticles were characterized by Raman Spectroscope (Perkin Elmer model Spectrum GX).

3.5.4 Scanning Mobility Particle Sizer (SMPS)

The SMPS (TSI model 3081) was used to analyze particle size distribution of airborne SWCNTs synthesized by laser ablation, and classify their size. The SMPS consists of differential mobility analyzer (DMA) as the main component for generating or sizing aerosol. For example given a polydisperse input aerosol, the instrument output can be a stream of monodiperse aerosol of known particle size. The number of monodisperse aerosol was counted by condensation particle counter (CPC).

3.5.5 X-Ray Diffraction (XRD)

The XRD (Bruker model X8APEX) was used to characterize phase of the synthesized carbon nanoparticles, ZnO nanoparticles and their composites.

3.5.6 UV-Visible Spectrophotometer (UV-Vis)

The UV-Vis spectrophotometer (Shimadzu model UV-1700) was used to measure absorbance of the synthesized carbon nanoparticles, ZnO nanoparticles and their composites.

3.5.7 Fourier Transform Infrared Spectrophotometer (FT-IR)

The FT-IR spectrometer (Thermo model 470 FT-IR) was used to measure bonding of the composite of carbon nanoparticles and ZnO nanoparticles.

CHAPTER IV

RESULT AND DISCUSSION

4.1 Synthesis of the SWCNTs by laser ablation

Referring to many experimental results reported in other previous works, this part has set its aim to study effect of synthetic parameters on the morphology, size and purity of the airborne SWCNTs synthesized by Nd:YAG pulsed laser ablation of C/Ni/Co rod. Effect of laser intensity and synthesizing temperature on the morphologies, size and purity of the synthesized SWCNTs were thoroughly investigated and then reported and discussed in this part.

4.1.1 Effect of laser intensity

In this part, the effect of the laser intensity at the intensity of 0.4, 0.5 and 0.6 W on morphology, particle size distribution and crystallinity of the synthesized carbon nanoparticles in aerosol was studied under the same condition of nitrogen flow rate of 1.5 L/min, temperature of 25ºC and atmospheric pressure.

The morphology of the synthesized carbon nanoparticles at different laser intensities of 0.4, 0.5 and 0.6 W was shown in Figure 4.1. Agglomerated primary carbon nanoparticles without fibrous particles could be clearly observed although the laser intensity was increased.
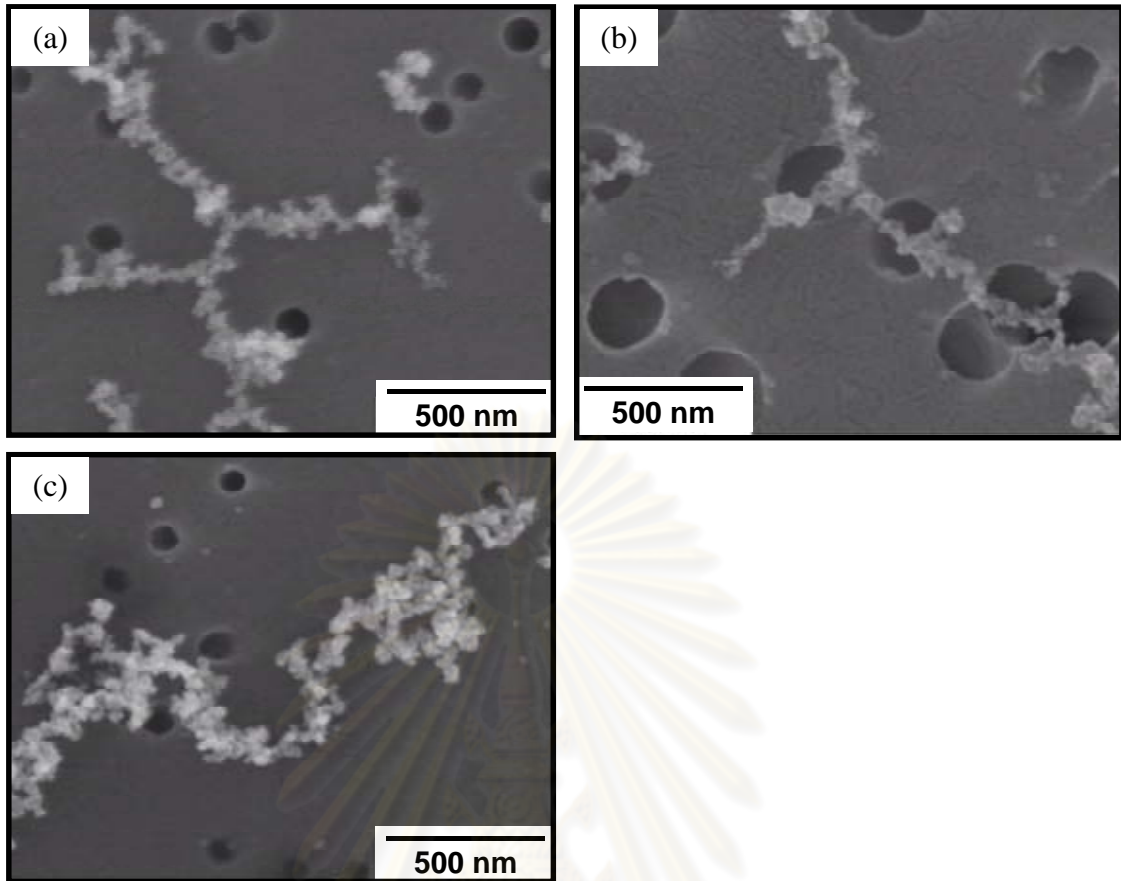
Figure 4.1 SEM images of the synthesized carbon nanoparticles at different laser intensities: (a) 0.4 W, (b) 0.5 W and (c) 0.6 W.

The size distributions based on electrical mobility of the agglomerated carbon nanoparticles synthesized at the laser intensity of 0.4, 0.5 and 0.6 W as shown in Figure 4.2 are similar normal curve with nearly same average sizes about 100 nm. At the laser intensity of 0.4 W, the number concentration of the synthesized carbon nanoparticles was 10.8×10^4 particles/cc. While at higher laser intensity the concentration was significantly increased. The number concentrations of the synthesized carbon nanoparticles were 31.0×10^4 and 35.6×10^4 particles/cc at the laser intensity of 0.5 and 0.6 W, respectively.
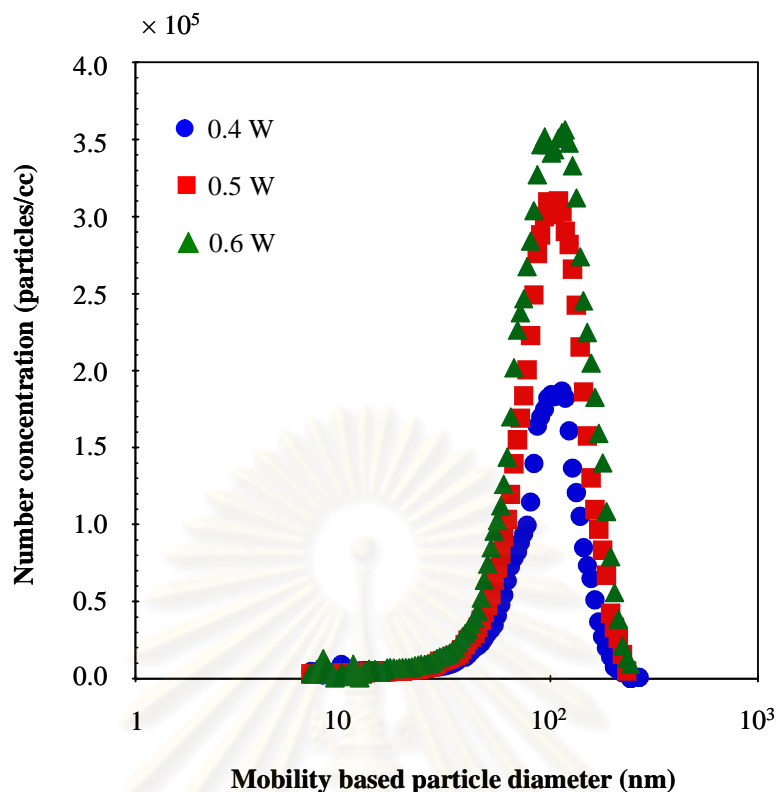
Figure 4.2 Size distributions of the agglomerated carbon nanoparticles synthesized at different laser intensities: (a) 0.4 W, (b) 0.5 W and (c) 0.6 W.

Similarity of the mobility size distributions was considered to be corresponding to the similarity of generated any fibrous particles as shown in the typical SEM images. From the relation of the images and size distributions, we could conclude that increasing the laser intensity while the controlled temperature at 25 ℃ did not effect on the morphology, which carbon nanoparticles were only formed, but effect on the concentration of the synthesized carbon nanoparticles.

Raman spectrum of the agglomerated carbon nanoparticles synthesized at the laser intensity of 0.6 W as shown Figure 4.3 shows its strong responses at about 1,590 cm^{-1} from graphitic bonding in crystalline carbon which known as G peak, and another peak at about 1,350 cm^{-1} from disorder and defective carbon which known as D peak. The I_D to I_G ratio of the carbon nanoparticles was 0.81.
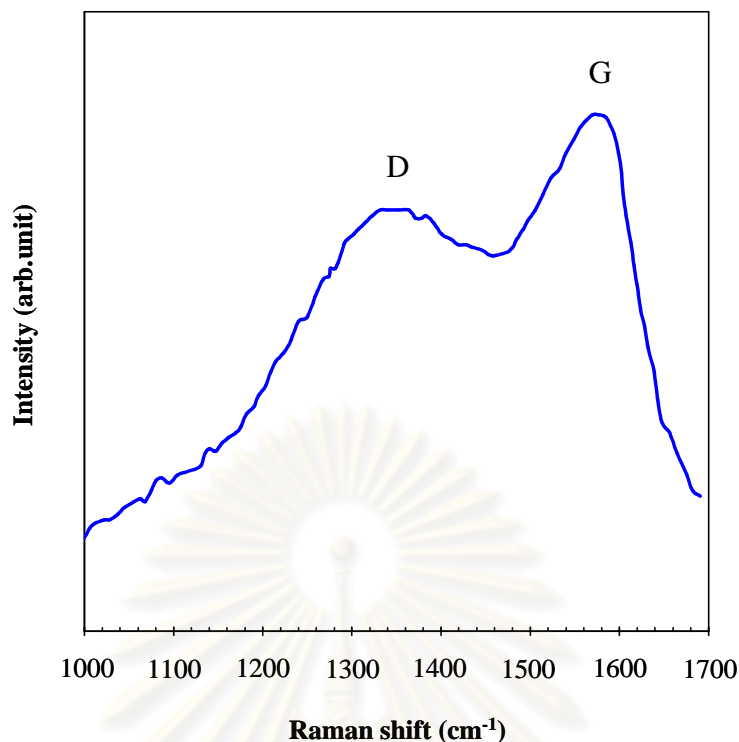
Figure 4.3 Raman spectrum of the agglomerated carbon nanoparticles synthesized at the laser intensity of 0.6 W.

These results could be ascribed that at a low temperature, vapor of the catalytic Ni and Co produced by the irradiation of the rod was condensed and then solidified rapidly because temperature difference between the furnace and laser irradiation was so high, leading to C atoms could diffuse and dissolve into the solidified catalytic nanoparticles difficultly (Yudasaka et al., 1999). Therefore, any fibrous could not be formed. However, the laser intensity effected on the number concentration of the synthesized carbon nanoparticles because C, Ni and Co vapor could be higher produced at increasing of laser intensity, leading to higher number concentration of the synthesized carbon nanoparticles.

4.1.2 Effect of temperature

In this part, the effect of the temperature in a range of 25, 200, 400, 600, 800, 1000 and 1080 ºC on the morphology, size distribution and crystallinity of the synthesized SWCNTs was investigated under the condition of the laser intensity of 0.6 W, atmospheric pressure and nitrogen flow rate of 1.5 L/min.

The synthesized airborne carbon nanoparticles at different temperatures were collected on a membrane filter. The morphology of those carbon nanoparticles was observed using SEM as shown in Figure 4.4. At the temperature of 25, 600 and 800 ℃, agglomerates of spherical nanoparticles were observed without any fibrous particles as shown in Figure 4.4(a), (b) and (c), respectively. While a higher concentration of fibrous and spherical products could be obtained at the temperature of 1000 and 1080 ℃ as shown in Figure 4.4(d) and (e), respectively. All fibrous particles have the average diameter less than 20 nm and length of longer than 500 nm while the spherical primary particles were in a size range of 10–20 nm, which were agglomerated each other. It is inferred that the fibrous products were CNTs and the spherical products were amorphous carbon or metallic nanoparticles.

These results would be ascribed to the fact that at a low temperature, carbon clusters and catalytic Ni and Co nanoparticles would undergo very slow diffusion process, leading to insufficient supply of carbon precursor (Yudasaka et al., 1999). Therefore, lower quantity of nanostructure products was synthesized.
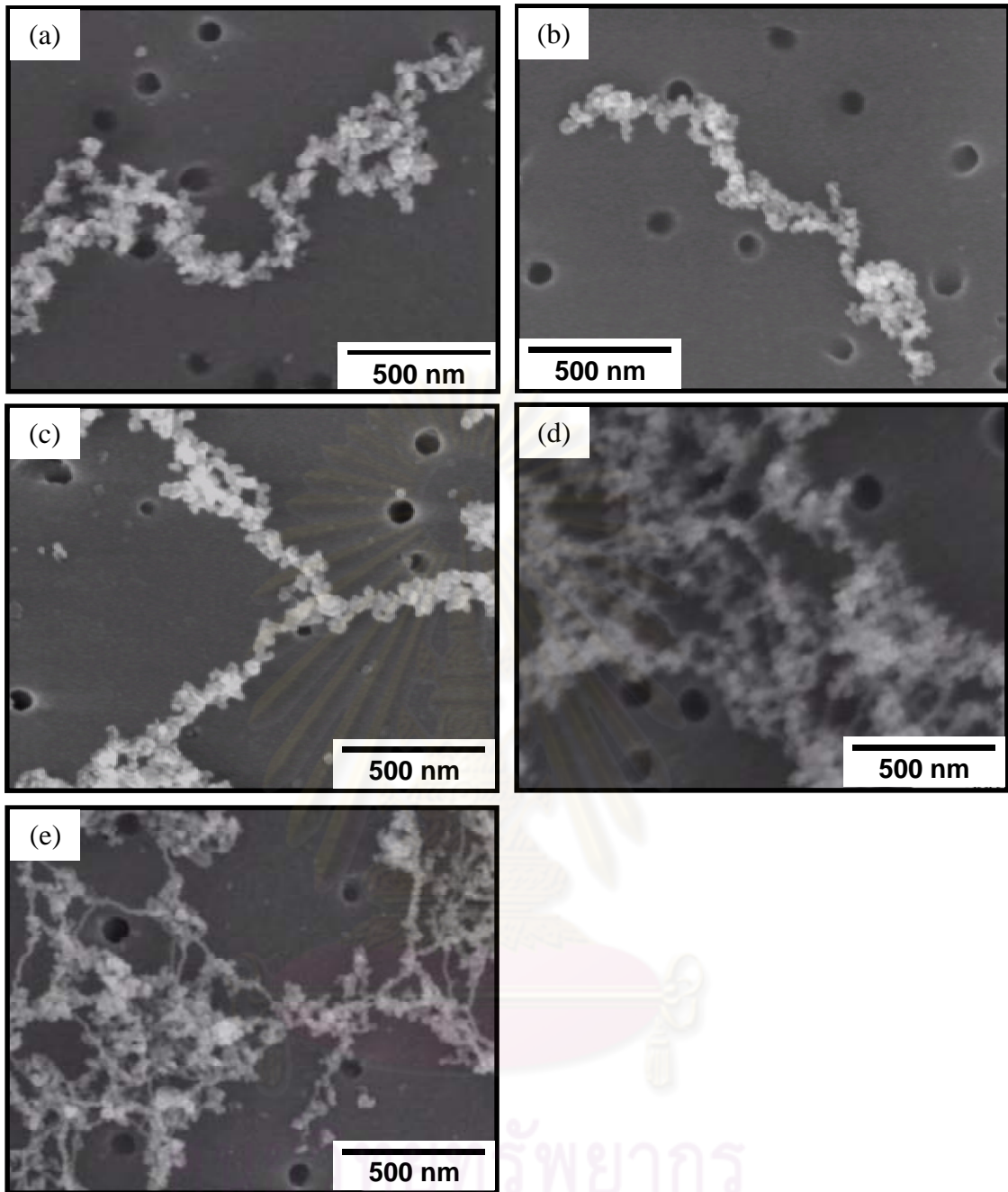
Figure 4.4 SEM images of the synthesized carbon nanoparticles at different temperatures on membrane filter: (a) 25 ºC, (b) 600 ºC, 800 ºC, (d) 1000 ºC and (e) 1080 ºC.

Size distributions of the produced airborne carbon nanoparticles measured by SMPS system are shown in Figure 4.5. In the measurable size range (20–600 nm in mobility diameter), highly carbon nanoparticles were synthesized in aerosol form. At the temperature of 25 ºC, relatively narrow size distribution with the peak diameter around 100–200 nm could be observed. Size distributions with the

same of the peak diameter become broader at higher temperatures (200, 400, 600 and 800 ºC). It could be clearly observed that at higher temperature, their size distribution was much broader, especially at the temperature of 600 and 800 ºC. While at the temperature of 1000 and 1080 ºC, size distributions were as similar as those of the temperature of 600 and 800 ºC. However, new peak around 20 nm was observed. The total number concentration of the synthesized CNTs could be synthesized by this system in the order of 10^6 particles/cc. It is corresponding to mass concentration in the order of ten mg/m^3 with an assumption of uniform density.
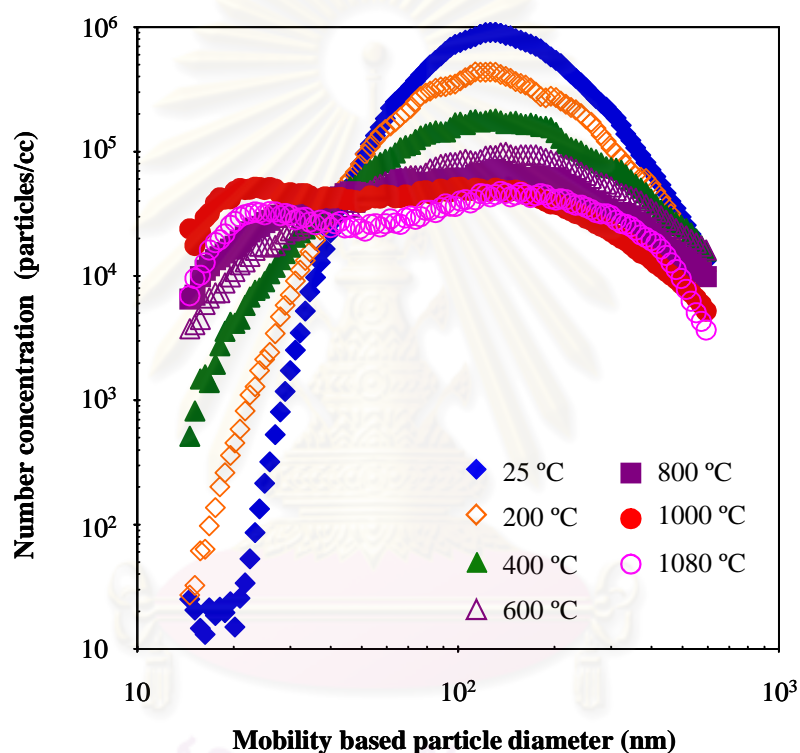
Figure 4.5 Mobility based size distribution of the synthesized carbon nanoparticles at different temperatures.

Changes in the mobility size distribution would be attributed to the generation of fibrous particles which could be observed in the typical SEM images. At the temperature of 25, 200, 400, 600 and 800 ºC, any fibrous particles could be observed in the SEM image because the catalyst particles could not activate majority of carbon atoms to form CNTs (Kataura et al., 2000). Therefore, only spherical (primary) particles formed and then agglomerated while the particles suspended in gas. On the other hand, at the temperature of 1000 and 1080 ºC, the temperatures were

high enough for stimulating the formation of the CNTs. Carbon atoms could be activated on the catalyst surface to grow CNTs. Furthermore, some agglomerated particles were simultaneously formed and adhered on the outer wall of the fibers in the gas phase.

In addition, the correlation between the geometric dimensions of CNT measured from SEM images (Figure 4.4) and mobility spectrum of those in the gas phase (Figure 4.5) was analyzed. The monodispersed aerosol of the synthesized SWCNTs at the temperature of 1080 ℃ was prepared by the size classification using DMA.
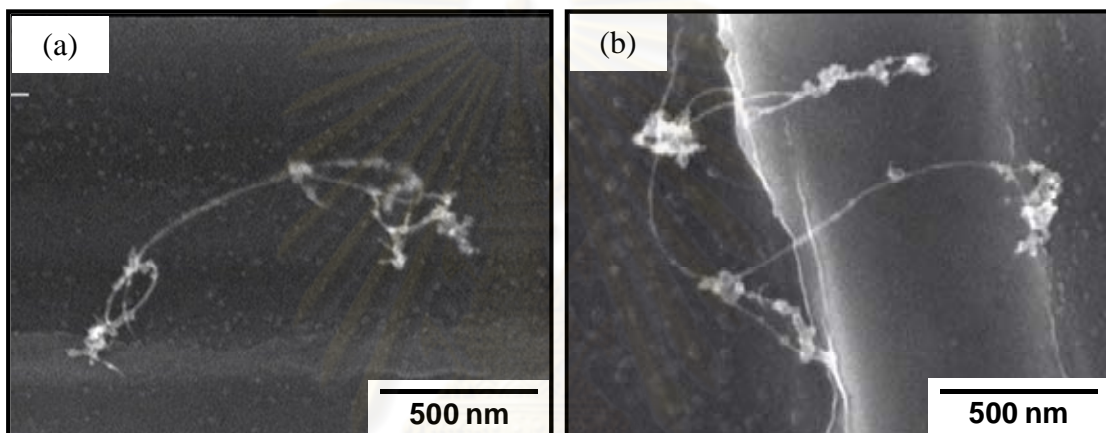
Figure 4.6 SEM images of the classified particles by DMA synthesized at the temperature of 1080 ℃ with different classified size: (a) 100 nm and (b) 200 nm.

Figure 4.6 shows typical SEM images of particles classified to be (a) 100 nm and (b) 200 nm in mobility-based diameter by DMA. Figure 6(a) exhibits fibrous structured particles with diameter less than 10 nm and length of more than 1 micrometer. Some spherical particles, which would potentially be amorphous carbon or catalytic particles, coagulate on to the surface of the fiber. The diameter of the fiber classified at 200 nm as shown in Figure 4.6(b) was similar to those of 100 nm. However, the length is much larger than the particle shown in Figure 4.6(a).

The mobility based particle diameter is known to be proportional to projected area equivalent diameter in the case of non-spherical particles (Kim, and Zachariah, 2006) as shown in equation 4.1

.

$$L_f D_f = \frac{\pi D_A^2}{4} \qquad\qquad (4.1)$$

where L_f = The length of the CNT,

D_f = The diameter of the CNT

D_A = The projected area diameter of the CNT

Kim et al., 2006 reported that the mobility diameter (D_m) of CNTs was determined by linearly proportional to the projected area diameter (D_A), which was obtained from the combination of TEM images and digital image software analysis. Therefore, it is acceptable that the projected area diameter (D_A) of carbon nanoparticles could be estimated from the mobility diameter (D_m) as shown in 4.2. Constants were obtained in a prior study where mobility classified fibers were deposited on TEM grids and digitized to obtain the projected area diameter.

$$D_A = 1.1621D_m - 8.9131 \qquad\qquad (4.2)$$

Therefore, the similar size distributions of the synthesized SWCNTs at 1000 and 1080 °C could imply the similar projected area equivalent diameter of them which corresponded to the similar morphology of them as shown in Figure 4.4(b) and (c), respectively.

The similarity of the fiber diameter classified at 100 and 200 nm seems to be affected by the formation of uniform catalysts. After the ablation of the target, catalyst nanoparticles were generated by the vapor phase condensation. Then, carbon atoms diffused into the catalysts to form the tubes and became fibers. In other words, the numbers of the SWCNTs in each classified fiber diameter were close each other because the fibers originated from that of isolated tubes became lower energy after a certain fiber diameter was reached. Then, the addition of further isolated tubes might not been energetically favorable (Wang et al., 2006), leading to the nearly same numbers of the tubes in each fiber.

In order to characterize crystallinity of the synthesized carbon nanoparticles, Raman spectroscope was employed. Raman spectra of the airborne carbon nanoparticles synthesized at the different temperatures were shown in Figure 4.7. It is well recognized that the Raman shift band in the range of 100–300 cm^{-1},

which is known as the radial breathing mode (RBM), is a signature of SWCNTs (Saito, Dresselhaus, and Dresselhaus, 1998). Those RBM frequency ω_{RBM} (cm^{-1}) depends strongly on the SWCNT diameter (d_t), as could be described by equation 4.3.

$$\omega_{RBM} = \frac{A}{d_t} + B \qquad (4.3)$$

where A (in nm cm^{-1}) and B (in cm^{-1}) are constants and vary between isolate tube and bundle tubes.

Regarding to the low Raman shift range, broad spectrum in Figure 4.7(a) reveals that negligible amount of SWCNTs were synthesized at the temperature of 25 ºC, while the distinctive RBM signal at 220–240 cm^{-1} could assure the presence of SWCNTs within the airborne carbon nanoparticles synthesized at higher temperatures of 1000 and 1080 ºC, respectively. Regardless the effect of single tube–tube interaction within tube bundle, the respective values of parameter A and B equal to 248 nm cm^{-1} and 0 cm^{-1} (Jorio et al., 2001). As a result, the calculated diameter of the SWCNTs synthesized at 1000 and 1080 ºC were equivalent to 1.1 and 1.2 nm, respectively.

In the high Raman shift region (1,300–1,600 cm^{-1}) which is associated with the tangential C–C stretching mode of their radiated carbon nanoparticles, a stronger band at 1,590 cm^{-1} known as the G band, and another band at 1,350 cm^{-1} known as the D band are distinctively observed. The presence of graphitic bonding due to the periodic sp^2 valance in crystalline carbonaceous material would strengthen the intensity of the G band scattering (Ganter et al., 2009). This band shows two different components, the lower frequency component (G$^-$) and higher frequency component (G$^+$) which associated with vibration along the circumferential direction and direction of the CNT axis, respectively (Liu et al., 2009). Meanwhile, the D band would reflect the present of disorder and defective carbonaceous constituents. Therefore, the intensity of D to G band (I_D/I_G ratio) could represent the relative existence of amorphous carbon to crystalline components within the irradiated sample.
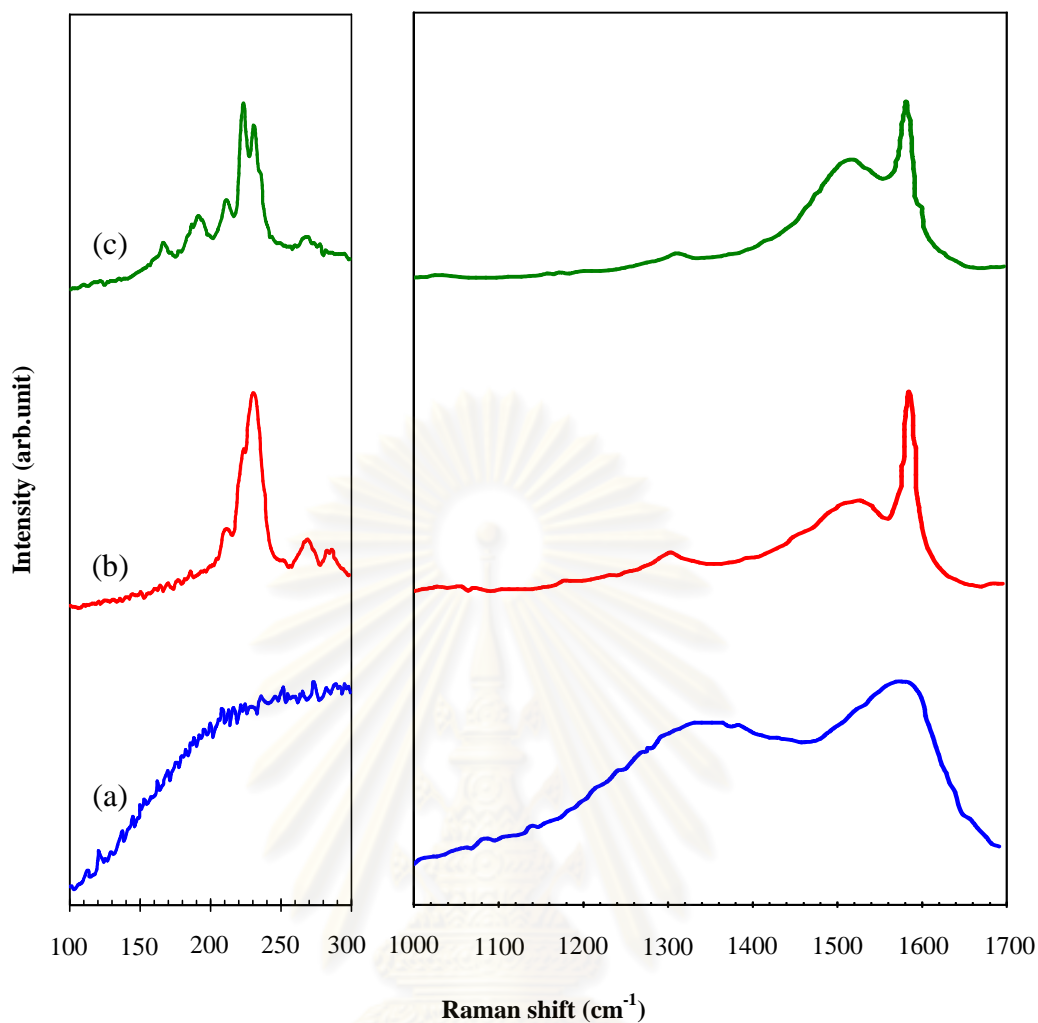
Figure 4.7 Raman spectra of the airborne SWCNTs synthesized at different temperatures: (a) 25 ℃, (b) 1000 ℃ and (c) 1080 ℃.

As could be observed in Figure 4.8, the I_D/I_G ratios of the synthesized carbon nanoparticles were 0.81, 0.20 and 0.15 at the temperature of 25, 1000 to 1080 ℃, respectively. In consistent with previous works (Kokai et al., 1999), these lower I_D/I_G ratios reveal the higher graphitic crystallinity of the airborne SWCNTs synthesized at the elevated temperature. Based on both lower and higher Raman shift signals, it could be anticipated that the airborne carbon nanoparticles synthesized at 1080 ℃ would contain the highest content of SWCNTs.
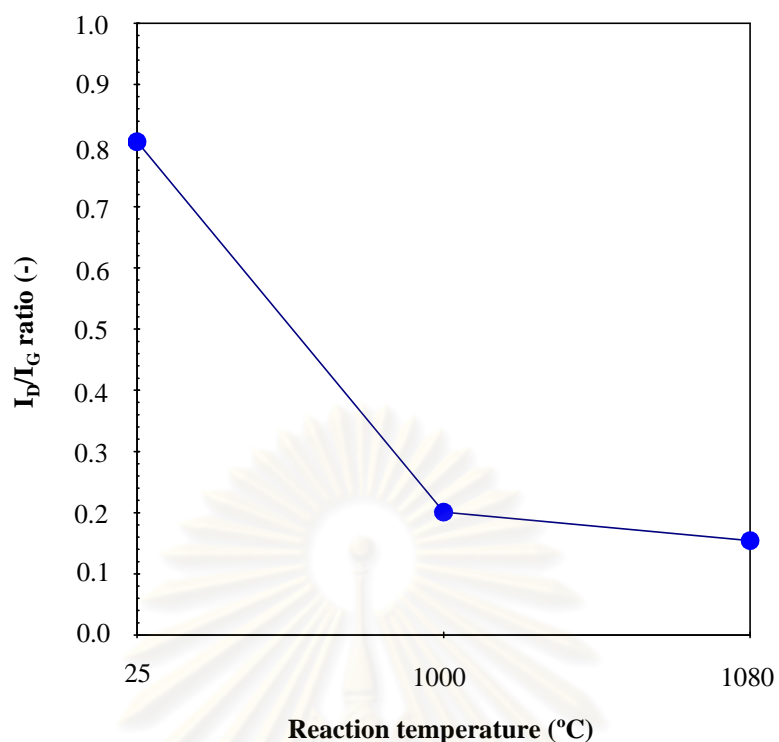
Figure 4.8 The I_D/I_G ratios of the synthesized carbon nanoparticles at different temperature.
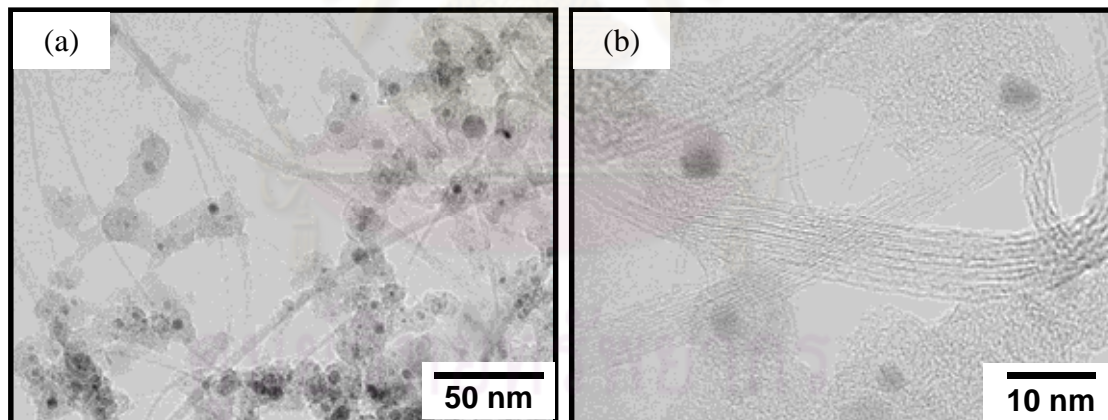
Figure 4.9 TEM images with different magnifications of the airborne SWCNTs synthesized at temperature of 1080 °C.

In order to finding the existence of SWCNTs within the airborne carbon nanoparticles, TEM analysis of as-prepared products was performed. HRTEM micrographs of the airborne product synthesized at 1080 °C were shown in Figure 4.9. It could be clearly seen the presence of isolated and bundling SWCNTs coexisting with amorphous carbon and catalyst nanoparticles.

Based on the TEM images, the diameter distribution of the isolated SWCNT is in a narrow range of 1.0–1.7 nm, which is in acceptable agreement with the calculated results using equation 4.3. Further quantitative analysis of SWCNT diameter was also conducted and plotted in Figure 4.10. It could be clearly observed that the modal diameter of the SWCNTs was about 1.2 nm.
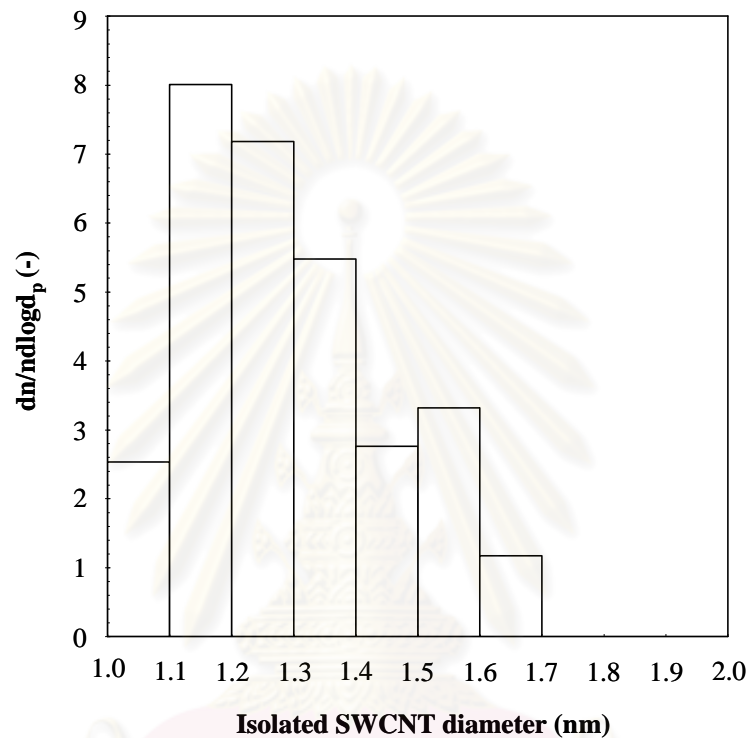
Figure 4.10 Size distribution of the isolated SWCNTs at the temperature of 1080 ℃ measured by TEM image processing.

4.1.3 Possible mechanisms

SWCNT formation mechanism, proposed here, is believed that vapor-liquid-solid (VLS) mechanism of carbon catalyzed by molten metal nanoparticles (Gorbunov et al., 2002). At first, carbon, nickel and cobalt vapors are produced from laser irradiation on the C/Ni/Co target rod. The metal catalyst particles act as nuclei for the growth of the tubes in the gas phase (Nyamori, Mhlanga, and Coville, 2008) are formed which shown in Figure 11. The Ni/Co catalyst vapors initially form nuclei in nucleation process, after that the nuclei condense and coagulate in condensation and particle coagulation, respectively. C vapors around the catalyst particles diffuse

on catalyst surface and dissolute until saturate inside the catalyst particles in carbon diffusion, dissolution and saturation of carbon process, respectively. Because of carbon saturation inside the catalysts, carbon atoms segregate from the catalyst particles and then form into SWCNTs.

This proposed mechanism also explains how the SWCNTs growth is influenced by the temperature. At the temperature of 1080 °C, the initial Ni/Co catalyst vapors gradually form into the molten catalytic particles because of gradual decreasing of temperature from laser source to temperature. The Ni/Co catalyst vapors can be transformed their phase into liquid droplets. Therefore, carbon vapors from laser vaporized C/Ni/Co target rod can highly diffuse into the molten catalytic particles. While the temperature of 1000 ℃, amount of the molten catalytic particles are decreased gradually leading to lower dissolution of the carbon vapors. Therefore, the SWCNTs synthesized at the temperature of 1000 ℃ have lower purity than those of 1080 ℃ as shown in Figure 5. However, at the temperature of 25 ℃, the catalytic particles are no longer molten in form of the liquid droplets but in solid particles because of rapid decreasing of the temperature from the laser source to the temperature. None of carbon vapors can dissolve into the catalytic particles at all, leading to none of the formation of the SWCNTs (Yudasaka et al. (1999)). This is reason of the SWCNTs at the higher temperature more clearly seen in Figure 4 which is good agreement with the formation behavior of the SWCNTs from size classification by DMA.

Vaporization of C, Ni and Co atoms	Nucleation, condensation and coagulation of Ni/Co catalyst	Diffusion of C on the catalyst surface	Dissolution of C inside the catalyst	Saturation of C in the catalyst	Segregation of C	CNT nucleation
C/Ni/Co Rod	C, Ni and Co vapors	Ni/Co catalyst and C	C on the catalyst surface	C dissoluted the catalyst	C saturated the catalyst	C segregated the catalyst	CNTs initiated by the catalyst

Hot Temperature Zone	Cooling Zone

Figure 4.11 Vapor-liquid-solid Mechanisms of the SWCNTs synthesized by laser ablation

4.2 Synthesis of the carbon nanoparticles by CVD of glycerol and ferrocene

From many experimental results reported in other previous works, this part has set its aim to study effect of synthetic parameters on the morphology, size, crystallinity and purity, and yield of the carbon nanoparticles synthesized by CVD of the mixture of glycerol and ferrocene. Effect of synthesizing temperature, nitrogen flow rate and glycerol to ferrocene molar ratio on the morphology, size, crystallinity and purity, and yield of the synthesized carbon nanoparticles were thoroughly investigated and then reported and discussed in this part.

Referring to temperature profiles as shown in Appendix A, it could be clearly seen each profile consisted of 3 temperature gradients along flow direction including zone 1 (0-15 cm from inlet) where the temperature increased from the lowest to the highest, zone 2 (15-45 cm from inlet) where the temperature was the highest and zone 3 (45-60 cm from inlet) where the temperature decreased from the highest to the lowest. It is well known that the temperature gradients and velocities gradients took place throughout the quartz tube reactor and could affect on the morphology, size, crystallinity and purity, and yield of the synthesized carbon nanoparticles. Therefore, the synthesized carbon nanoparticles were distinguish studied into 3 different zones as presented above.

4.2.1 Effect of nitrogen flow rate

In this part, the effect of nitrogen flow rate on the morphology, size, crystallinity and purity, and yield of the synthesized carbon nanoparticles was studied under the same condition of synthesizing temperature of 800 ℃ and glycerol to ferrocene molar ratio of 5 to 1.

Zone 1

SEM images as shown in Figure 4.12 revealed the carbon nanoparticles deposited at zone 1 within the quartz tube reactor with different nitrogen flow rates. At nitrogen flow rate of 50 mL/min, the morphology of the synthesized carbon nanoparticles shown in Figure 4.12(a) was warm-like MWCNTs with outer diameter and length of the tubes in range of 175-200 nm and 600-750 nm,

respectively. While the longer MWCNTs were clearly seen at higher nitrogen flow rate. At nitrogen flow rate of 200 mL/min, the MWCNTs with outer diameter of about 180 nm and length of about 10 μm, respectively were synthesized as shown in Figure 4.12(b). At nitrogen flow rate of 350 and 500 mL/min, the synthesized carbon nanoparticles were carpet-like MWCNT structure as shown in Figure 4.12(c) and (d), respectively. The diameters of the tubes at nitrogen flow rate of 350 mL/min were in range of 30-80 nm. While the diameters of the tubes at nitrogen flow rate of 500 mL/min were in range of 30-60 nm. Furthermore, it could be clearly seen some amorphous carbons deposited on the outer wall of the synthesized MWCNTs.

Figure 4.12 SEM images of the MWCNTs deposited at zone 1 with different nitrogen flow rates: (a) 50 mL/min, (b) 200 mL/min, (c) 350 mL/min and (d) 500 mL/min.

Raman spectra of the MWCNTs deposited at zone 1 with different nitrogen flow rates as shown Figure 4.13 exhibited their strong response at about 1,590 cm^{-1} from graphitic bonding in crystalline carbon which known as G peak, and another peak at about 1,350 cm^{-1} from disorder and defective carbon which known as D peak. The I_D to I_G ratios of the MWCNTs deposited at zone 1 with the nitrogen flow rate of 50, 200, 350 and 500 mL/min were 0.66, 0.33, 0.24 and 0.28, respectively.

Figure 4.13 Raman spectra of the MWCNTs deposited at zone 1 with different nitrogen flow rates: (a) 50 mL/min, (b) 200 mL/min, (c) 350 mL/min and (d) 500 mL/min.

Zone 2

SEM images of the carbon nanoparticles deposited at zone 2 with different nitrogen flow rates were shown in Figure 4.14. At nitrogen flow rate of 50 mL/min, the synthesized carbon nanoparticles shown in Figure 4.14(a) was warm-like MWCNTs with outer diameter and length of the tubes in range of 125-200 nm and about 1 μm, respectively. While the longer MWCNTs were clearly seen at higher

nitrogen flow rate. At nitrogen flow rate of 200 mL/min, the curvature of MWCNTs with outer diameters in range of 40-150 nm were synthesized as shown in Figure 4.14(b). At nitrogen flow rate of 350 mL/min, the synthesized carbon nanoparticles were straight MWCNTs with the outer diameters in range of 40-80 nm as shown in Figure 4.14(c). While the morphology of synthesized carbon nanoparticles at the nitrogen flow rate of 500 mL/min was urchin-like MWCNT structure which the tubes with the outer diameter and length of their tubes in range of 30-60 nm and about 1 µm, respectively were grown from agglomerated catalytic particles as shown in Figure 4.14(d).
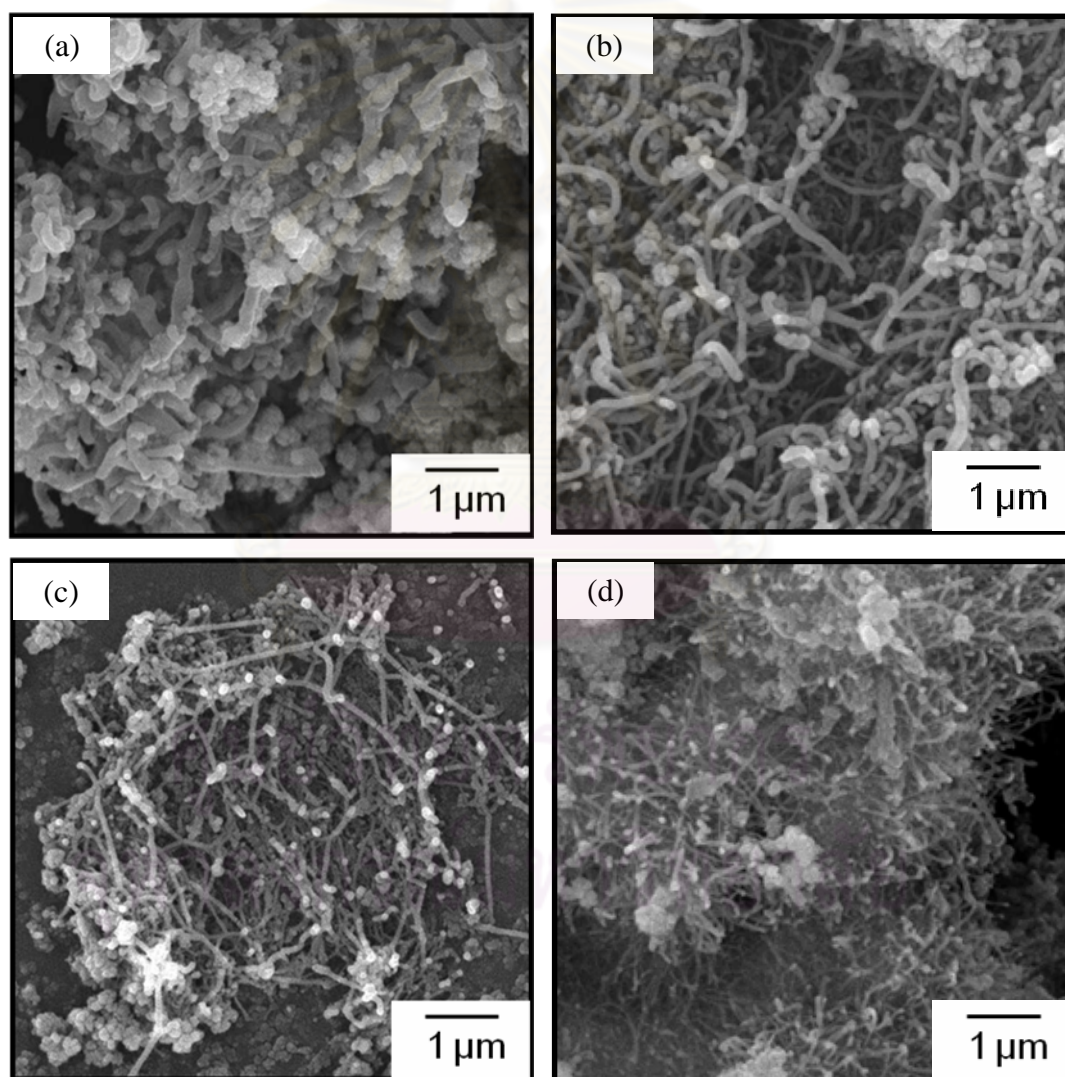
Figure 4.14 SEM images of the MWCNTs deposited at zone 2 with different nitrogen flow rates: (a) 50 mL/min, (b) 200 mL/min, (c) 350 mL/min and (d) 500 mL/min.

Raman spectra of the MWCNTs deposited at zone 2 with different nitrogen flow rates in Figure 4.15 exhibited the same of 2 responses at G peak and D peak which the I_D to I_G ratios of the MWCNTs deposited at zone 2 with the nitrogen flow rate of 50, 200, 350 and 500 mL/min were 0.88, 0.43, 0.21 and 0.31, respectively.
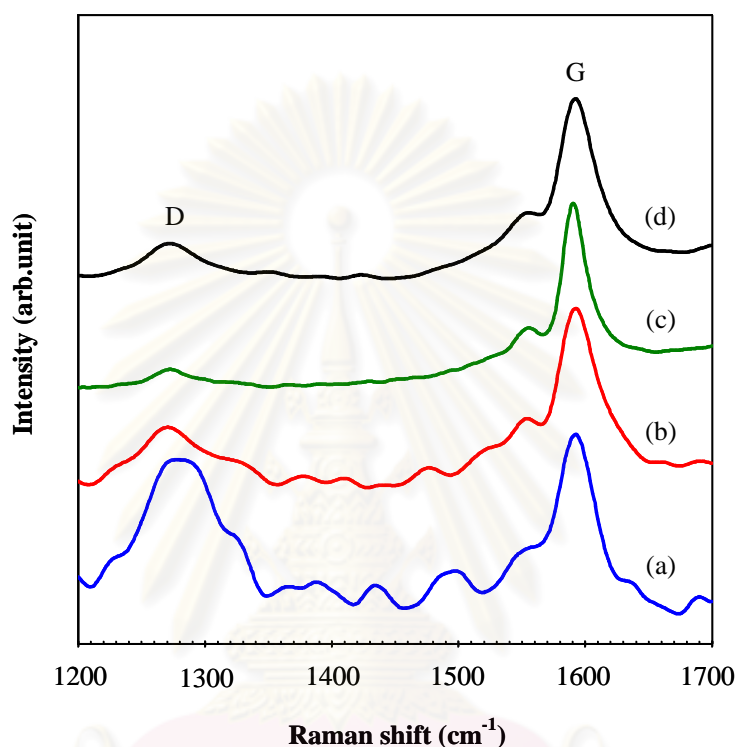
Figure 4.15 Raman spectra of the MWCNTs deposited at zone 2 with different nitrogen flow rates: (a) 50 mL/min, (b) 200 mL/min, (c) 350 mL/min and (d) 500 mL/min.

Zone 3

SEM images as shown in Figure 4.16 revealed the carbon nanoparticles deposited at zone 3 with different nitrogen flow rates. At nitrogen flow rate of 50 mL/min, the synthesized carbon nanoparticles shown in Figure 4.16(a) was MWCNTs with outer diameter and length of the tubes about 170 nm and 1-3 μm, respectively. While the longer MWCNTs were clearly observed at higher nitrogen flow rate. At nitrogen flow rate of 200 mL/min, the MWCNTs with outer diameters and length of the tubes in range of 80-170 nm and more than 3 μm, respectively were

synthesized as shown in Figure 4.16(b). While the morphology of synthesized carbon nanoparticles at the nitrogen flow rate of 350 mL/min was carpet-like MWCNT structure which the tubes with the outer diameters in range of 40-80 nm as shown in Figure 4.16(c). At nitrogen flow rate of 500 mL/min, the synthesized carbon nanoparticles were the combination of the straight MWCNTs with the outer diameters about 50 nm and agglomerated particles as shown in Figure 4.16(d).
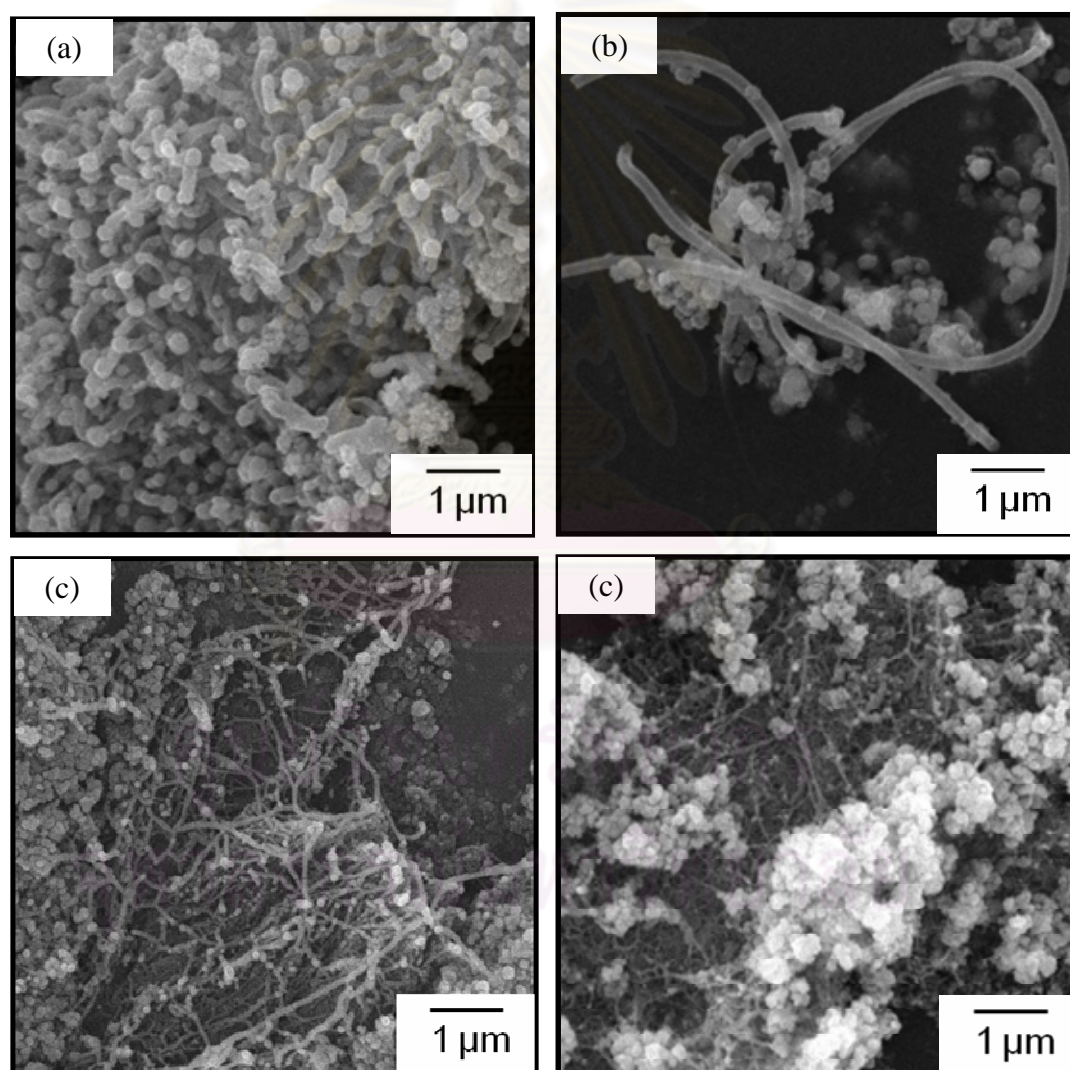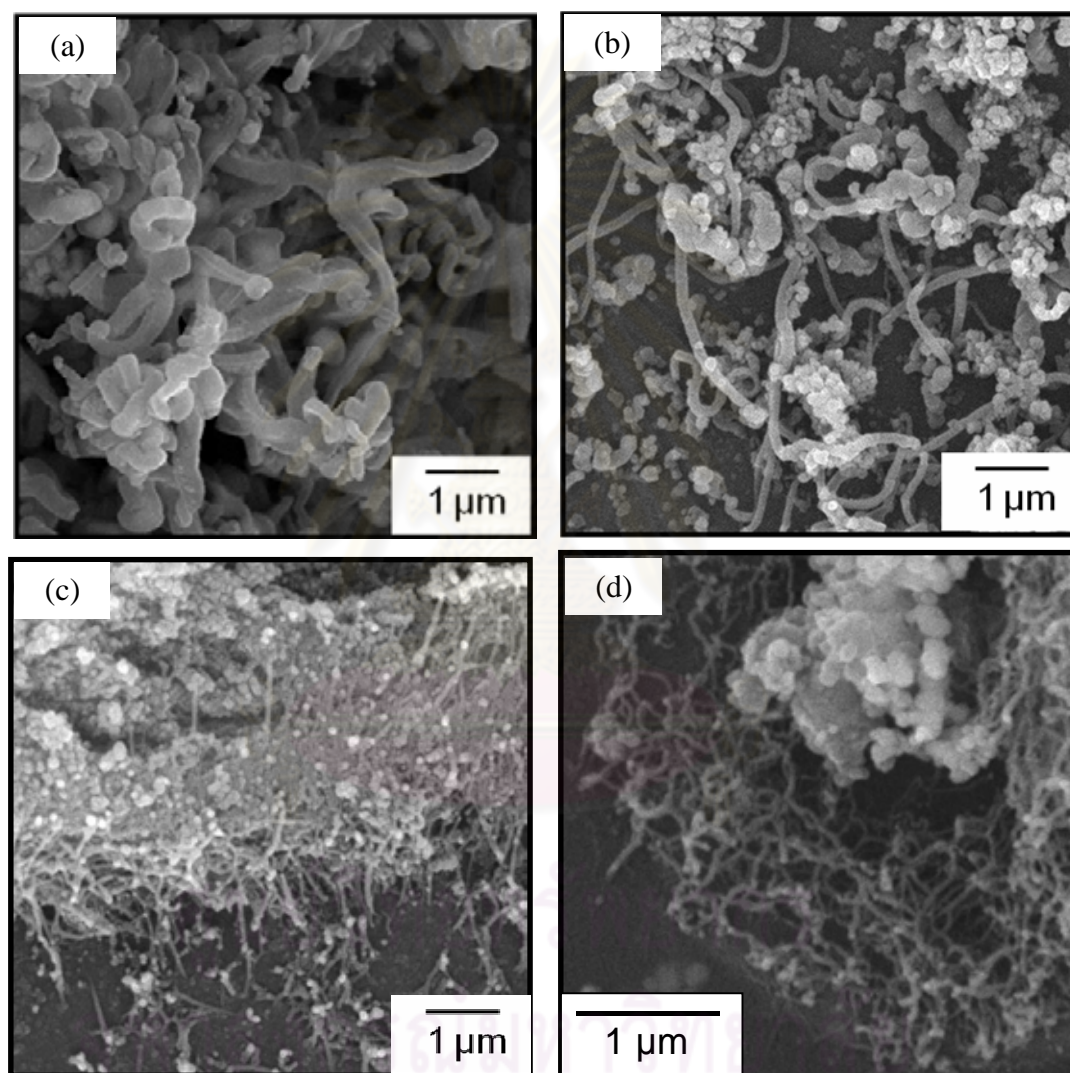

Figure 4.16 SEM images of the MWCNTs deposited at zone 3 with different nitrogen flow rates: (a) 50 mL/min, (b) 200 mL/min, (c) 350 mL/min and (d) 500 mL/min.

Raman spectra of the MWCNTs deposited at zone 3 synthesized with different nitrogen flow rates were shown in Figure 4.17. Their responses were at G peak and D peaks. The I_D/I_G ratios of the MWCNTs deposited at zone 3 with the

nitrogen flow rate of 50, 200, 350 and 500 mL/min were 0.59, 0.43, 0.22 and 0.31, respectively.
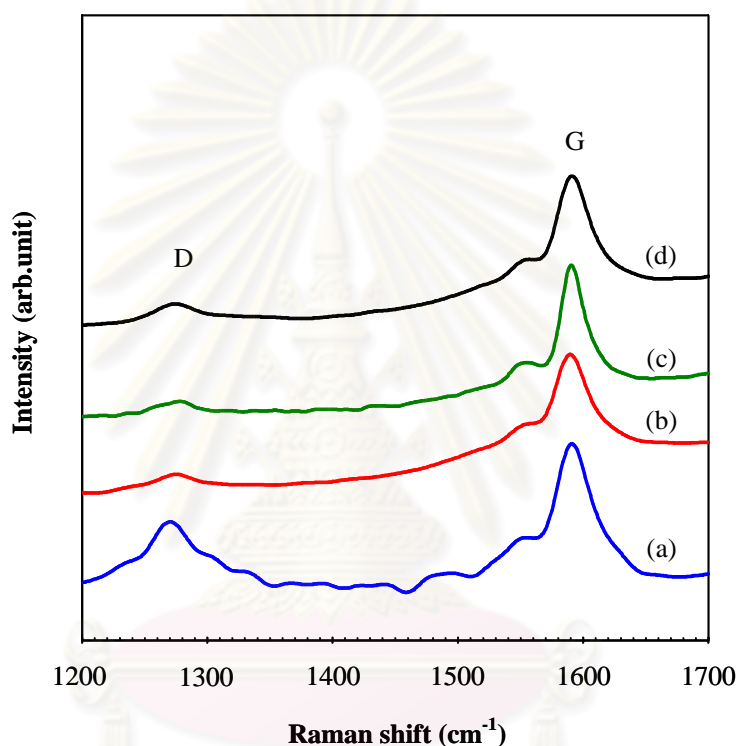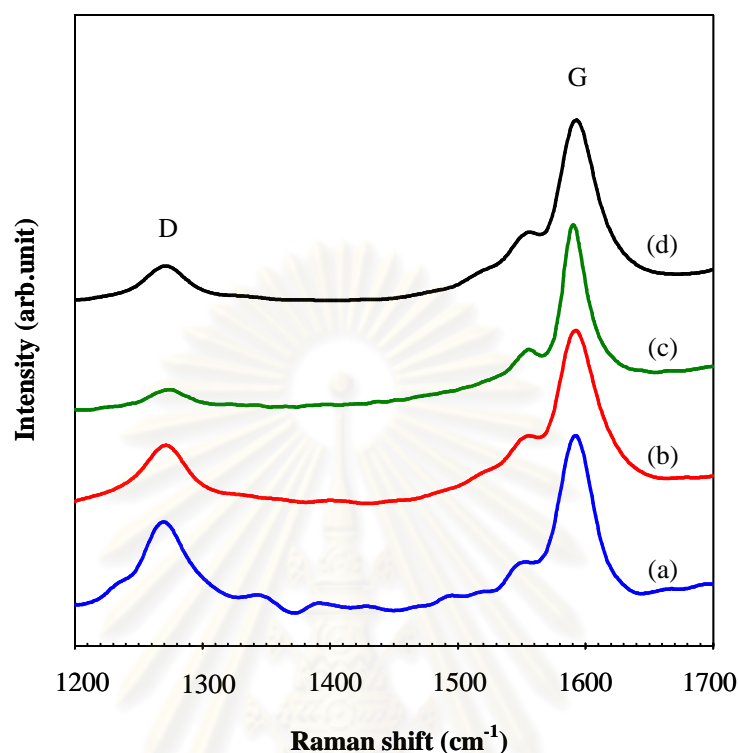

Figure 4.17 Raman spectra of the MWCNTs deposited at zone 3 with different nitrogen flow rates: (a) 50 mL/min, (b) 200 mL/min, (c) 350 mL/min and (d) 500 mL/min.

The I_D/I_G ratios in Figure 4.18 revealed that the nitrogen flow rate strongly affected on crystallinity and purity of the synthesized carbon nanoparticles. At nitrogen flow rate of 50 mL/min, the carbon nanoparticles deposited at begin, middle and zone 3 had the lowest crystallinity and purity compared to the carbon nanoparticles synthesized at higher flow rate deposited at the same positions. While the carbon nanoparticles synthesized at nitrogen flow rate of 350 mL/min had the highest crystallinity and purity. Therefore, in this work, the nitrogen flow rate of 350 mL/min was optimal flow rate for the synthesis of the CNTs.
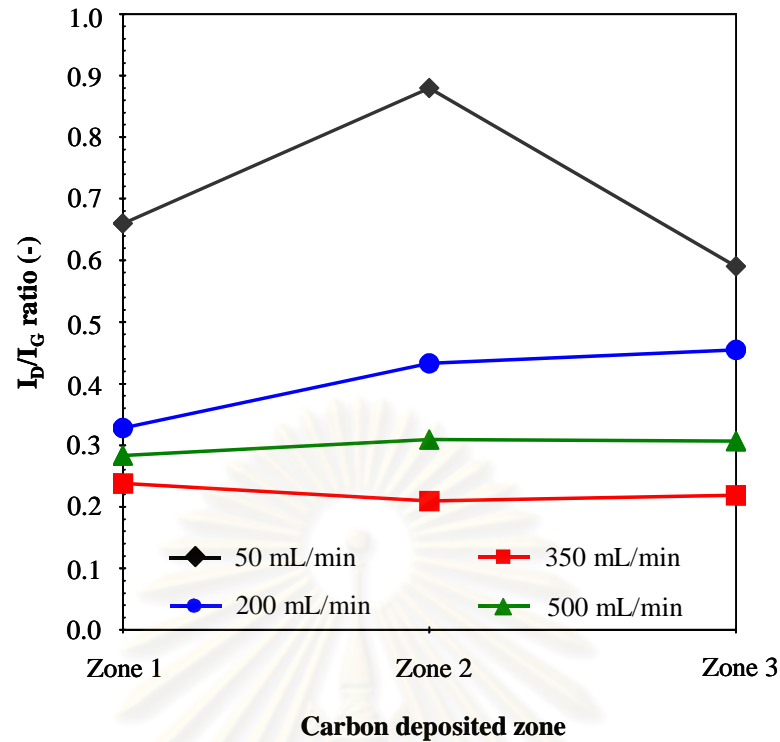
Figure 4.18 I_D/I_G ratios of the synthesized MWCNTs at different nitrogen flow rates.

Carbon yields of the synthesized carbon products can be defined in equation 4.4.

$$\text{Carbon yield}\,(\%) = \frac{W_{C,1} + W_{C,2} + W_{C,3}}{W_{\text{glycerol}} + W_{\text{ferrocene}}} \times 100 \qquad (4.4)$$

where $W_{C,1}$ = Weight of synthesized carbon at zone 1

                   $W_{C,2}$ = Weight of synthesized carbon at zone 2

                   $W_{C,3}$ = Weight of synthesized carbon at zone 3

                   W_{glycerol} = Weight of used glycerol

                   $W_{\text{ferrocene}}$ = Weight of used ferrocene

Figure 4.19 shows the carbon yields of the synthesized carbon nanoparticles with different nitrogen flow rates. At the nitrogen flow rate of 50 mL/min, the carbon yield was 6.1 %. While the yield gradually decreased as 4.2, 2.1 and 1.7 % at the nitrogen flow rate of 200, 350 and 500 mL/min, respectively.
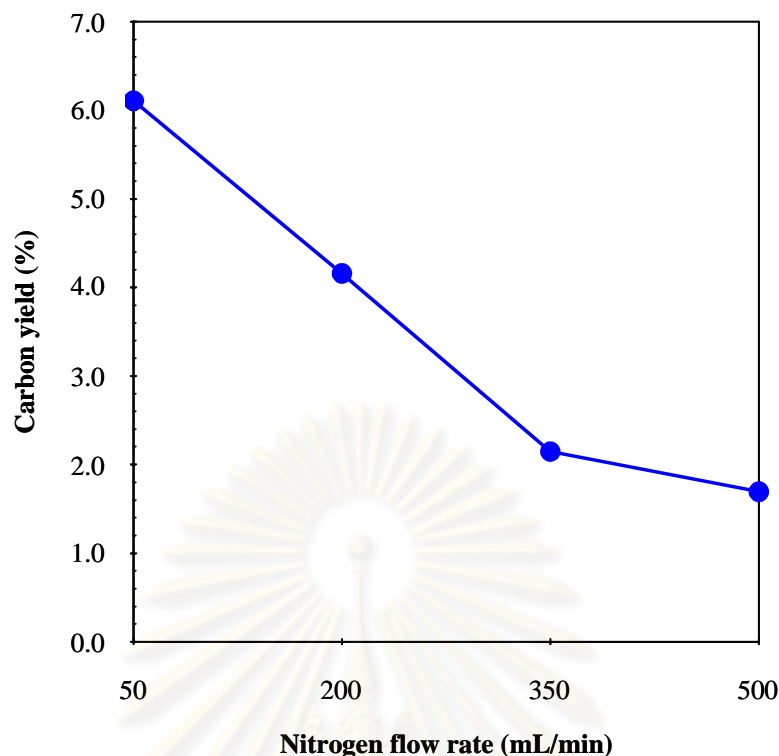
Figure 4.19 Yields of the synthesized carbon nanoparticles at different nitrogen flow rates.

It is well known that residence time is the time that a particle spends in a particular system which is the inversely proportional function of a flow rate. From Figure 4.20, it could be clearly observed that residence time was significantly decreased from 11.5 to 2.9, 1.6 and 1.2 when the nitrogen flow rate was increased from 50 to 200, 350 and 500 mL/min.

From the experimental results, the increase in the nitrogen flow rate resulted in significant decrease in the tube diameters which could be explained by residence time. From previous work (Kobayashi et al., 2004), it should be noted that the diameters of the synthesized CNTs were closely correlated with those of the catalytic nanoparticles and tended to be slightly smaller than the particle size. It means that decrease in the Fe size resulted in decrease in diameters of the tubes. The decrease in the Fe size could be occurred when aggregation of the Fe nanoparticles was decreased. Endo et al., 2001 reported that the aggregation of the Fe nanoparticles was decreased when the nitrogen flow rate was increased because of decrease in residence time. Therefore, in this part, the synthesized MWCNTs at the nitrogen flow rate of 50 mL/min with large tube diameters were found. While, at higher nitrogen

flow rate, the tube diameters of the synthesized MWCNTs significantly decreased because at higher nitrogen flow rate, the residence time was shorter, leading smaller size of the Fe nanoparticles as discussed above.

Increase in the nitrogen flow rate also resulted in significant decrease in the carbon yield. At the nitrogen flow rate of 50 mL/min, the residence time for contacting of the catalytic nanoparticles in liquid phase and carbon atoms was the maximum, leading to the highest yield of the carbon products. However, the maximum residence time for the contacting of the molten catalytic nanoparticles and the carbon atoms was too much, leading to excess carbon atoms could diffuse into the catalytic nanoparticles and then the catalytic nanoparticles were no longer activate the carbon atoms to form the CNTs. It is a reasonable that why the morphologies of the carbon nanoparticles synthesized at the lowest nitrogen flow rate were warm-like MWCNTs with the lowest purity and crystallinity compared to those at higher nitrogen flow rate. While decreasing of the carbon yield was taken place by decreasing of the residence time when the nitrogen flow rate was increased, leading to lower contacting of the catalytic nanoparticles and carbon atoms (Chaisitsak, Nukeaw and Tuantranont, 2007).
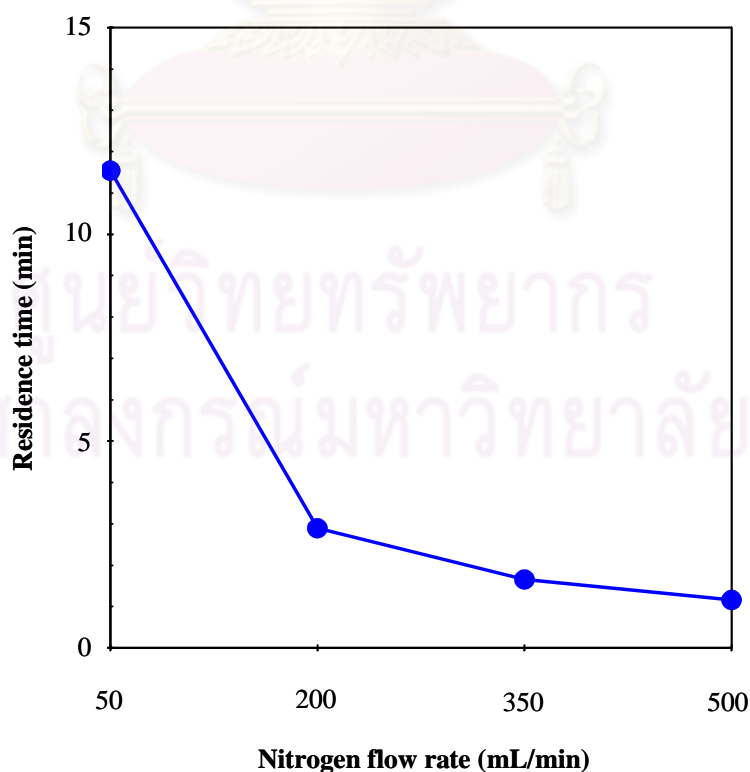
Figure 4.20 Residence time by varying nitrogen flow rate.

4.2.2 Effect of synthesizing temperature

In this part, the effect of the synthesizing temperature on the quality and quantity of the synthesized carbon nanoparticles was studied at condition of nitrogen flow rate of 350 mL/min and glycerol to ferrocene molar ratio at 5 to 1.

Zone 1

SEM images as shown in Figure 4.21 revealed the carbon nanoparticles deposited at zone 1 with different synthesizing temperatures. At the synthesizing temperature of 800 ºC, the morphology of the synthesized carbon nanoparticles shown in Figure 4.21(a) was combination of the MWCNTs with outer diameters of the tubes in range of 30-80 nm and some of amorphous carbon. The MWCNTs with bigger outer diameter were clearly found at higher synthesizing temperature. At the synthesizing temperature of 850 ºC, the uniform MWCNTs with outer diameter and length of the tubes in range of 50-125 nm and more than 10 nm, respectively were synthesized shown in Figure 4.21(b). While the synthesized carbon nanoparticles at the synthesizing temperature of 900 ºC were combination of the MWCNTs with the diameters and length of the tubes in range of 90-190 nm and more than 10 nm, respectively and deposited amorphous carbon on the outer wall of the synthesized MWCNTs as shown in Figure 4.21(c).
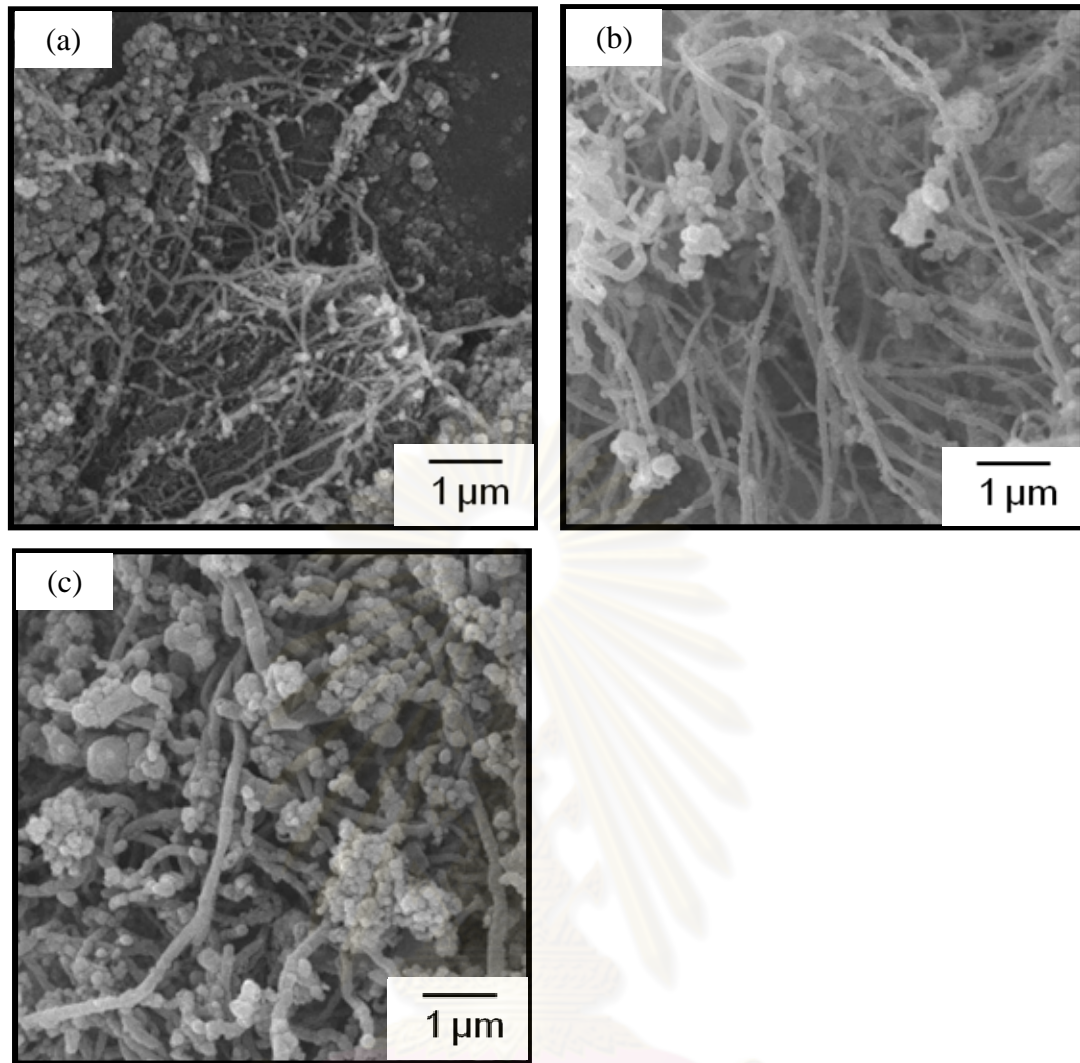
Figure 4.21 SEM images of the MWCNTs deposited at zone 1 with different synthesizing temperatures: (a) 800 ℃, (b) 850 ℃ and (c) 900 ℃

Zone 2

SEM images as shown in Figure 4.22 revealed the carbon nanoparticles deposited at zone 2 with different synthesizing temperatures. At the synthesizing temperature of 800 ℃, the synthesized carbon nanoparticles shown in Figure 4.22(a) were straight MWCNTs with outer diameters of the tubes in range of 40-80 nm. While larger outer diameters of the MWCNTs were found at higher the synthesizing temperatures. At the synthesizing temperature of 850 ℃, the MWCNTs with outer diameters in range of 60-190 nm, respectively were synthesized as shown in Figure 4.22(b). At the synthesizing temperature of 900 ℃, the MWCNTs with outer diameters in range of 180-320 nm were synthesized as shown in Figure 4.22(c).
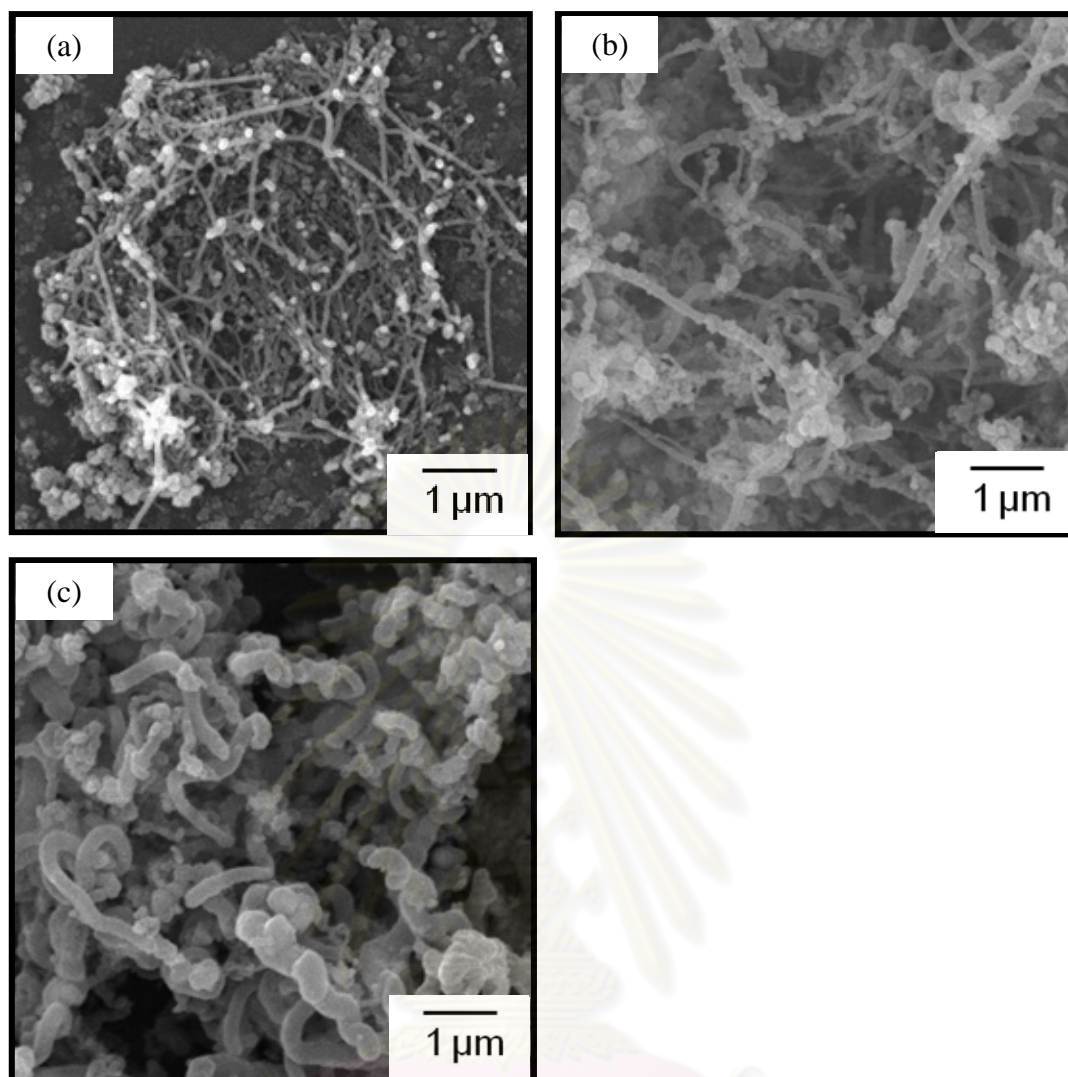
Figure 4.22 SEM images of the MWCNTs deposited at zone 2 with different synthesizing temperatures: (a) 800 ℃, (b) 850 ℃ and (c) 900 ℃.

Zone 3

SEM images the carbon nanoparticles deposited at zone 3 with different synthesizing temperatures were shown in Figure 4.23. At the synthesizing temperature of 800 ℃, the morphology of the synthesized carbon nanoparticles shown in Figure 4.23(a) was the carpet-like MWCNTs with outer diameters of the tubes in range of 40-80 nm. The bigger diameters of the MWCNTs were clearly seen at higher synthesizing temperatures. At the synthesizing temperature of 850 ℃, the straight MWCNTs with outer diameters and length of the tubes in range of 80-90 nm and more than 15 μm, respectively were synthesized as shown in Figure 4.23(b). At the synthesizing temperature of 900 ℃, the synthesized carbon nanoparticles were

combination of the straight MWCNTs with the outer diameters of the tubes in range of 250-340 nm and helical MWCNTs as shown in Figure 4.23(c).
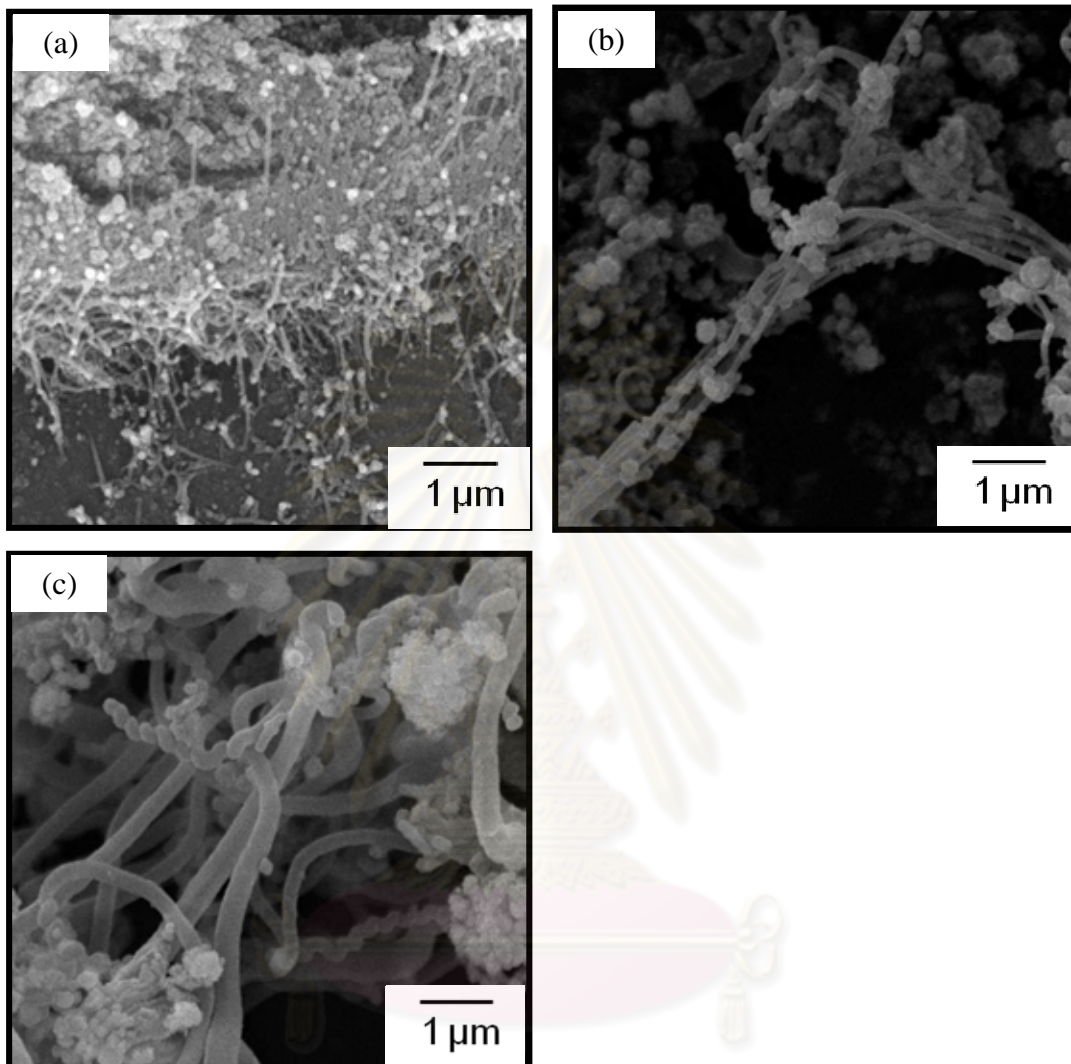
Figure 4.23 SEM images of the MWCNTs deposited at zone 3 with different synthesizing temperatures: (a) 800 ℃, (b) 850 ℃ and (c) 900 ℃.

The experimental results revealed that the tube diameters were increased when the synthesizing temperature was increased. The increase in the synthesizing temperature resulted in higher aggregation of the Fe nanoparticles (Stanek et al., 1995), leading to larger sizes of the Fe nanoparticles. Referring to above discussion, the tube diameters were controlled by the sizes of the Fe nanoparticles. Therefore, in this part, the larger sizes of the Fe nanoparticles at higher synthesizing temperature resulted in the larger tube diameters.

Raman spectra of the MWCNTs deposited at zone 1, zone 2 and zone 3 with different synthesizing temperatures exhibited their strong responses including D peak and G peak as same as the MWCNTs synthesized at different nitrogen flow rates. The I_D/I_G ratios of the synthesized MWCNTs with different synthesizing temperatures were shown in Figure 4.24.
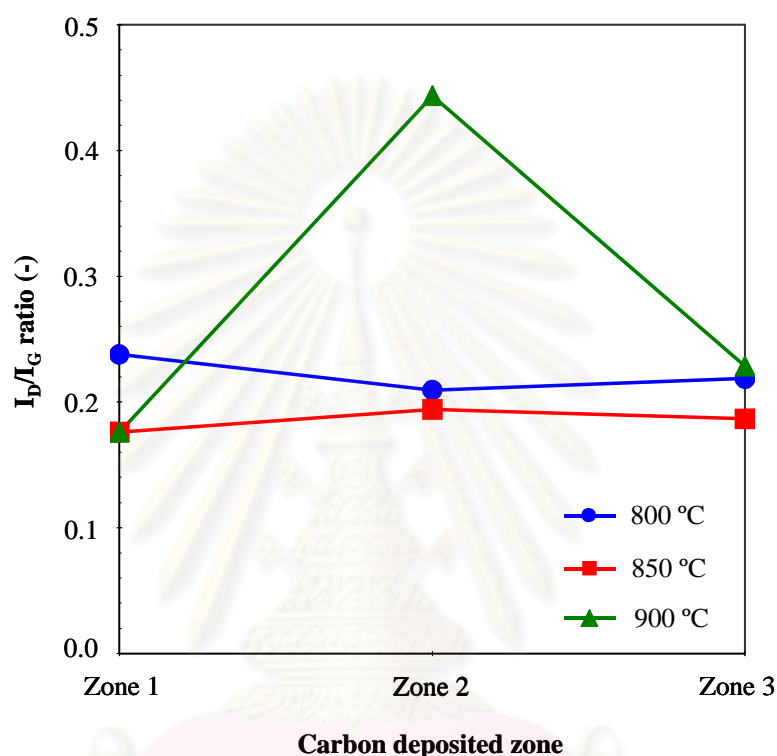
Figure 4.24 I_D/I_G ratios of the synthesized MWCNTs at different synthesizing temperatures.

The I_D/I_G ratios revealed that the synthesizing temperature strongly affected on crystallinity and purity of the synthesized carbon nanoparticles. At the synthesizing temperature of 800 ℃, the I_D/I_G ratios of the carbon nanoparticles deposited at zone 1, zone 2 and zone 3 were 0.24, 0.21 and 0.22, respectively. It could be clearly observed that, at the synthesizing temperature of 850 ℃, the I_D/I_G ratios of the carbon nanoparticles were few decreased compared to those synthesized at the temperature of 800 ℃. At the synthesizing temperature of 850 ℃, the I_D/I_G ratios carbon nanoparticles deposited at zone 1, zone 2 and zone 3 were 0.18, 0.19 and 0.19, respectively. While, at the synthesizing temperature of 900 ℃, the I_D/I_G ratio of the carbon nanoparticles at zone 1 and zone 3 were nearly the same as those of

synthesizing at the temperatures of 800 and 850 ºC which reported above. However, the I_D/I_G ratio of the carbon nanoparticles at zone 2 was significantly increased at the ratio of 0.44. Therefore, in this work, the synthesizing temperature of 850 ºC was found to be the optimal temperature for the synthesis of the CNTs.

From the experimental results, at the synthesizing temperature of 900 ºC, the I_D/I_G ratio of the carbon nanoparticles at zone 2 was increased significantly because decomposition of glycerol was higher than that of the synthesizing temperature of 800 and 850 ºC, leading to the Fe nanoparticles surrounded by higher amount of carbon atoms. These carbon atoms could diffuse continuously although the Fe catalyst was saturated by those former carbon atoms. Therefore, excess carbon atoms could not be dissolved into the Fe catalyst. Therefore, crystalline carbon could not be formed, leading to increase in the I_D/I_G ratio.

The carbon yields of the synthesized carbon nanoparticles at different synthesizing temperatures were shown in Figure 4.25. When the synthesizing temperature was increased from 800 to 850 and 900 ºC, the carbon yield was increased from 2.2 to 3.0 and 3.6 %, respectively.
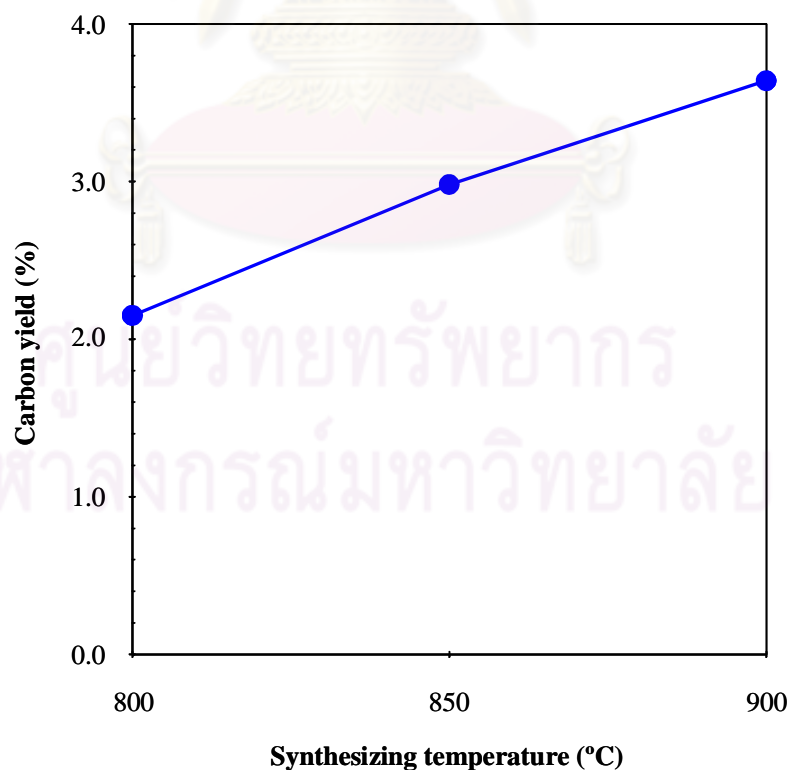
Figure 4.25 Yields of the synthesized carbon nanoparticles at different synthesizing temperatures

Lee et al., 2002 proposed alternative kinetic models of carbon nanoparticle formation and growth based on an assumption that the rate of the carbon nanoparticle formation could be assumed as a zero-order reaction. The rate constant of CNTs in equation 4.5 shows that increasing of synthesizing temperature makes increasing of rate constant of the CNTs as shown in Figure 4.26. Therefore, the increasing of the synthesizing temperature could promote the reaction rate of the formation of the CNTs which in term affected their yields.

$$-\ln k_{CNTs} = -3.8 + 1.51 \times \frac{10^4}{T} \qquad (4.5)$$

where k_{CNTs} = Rate constant of the CNTs (min^{-1})

T = Synthesizing temperature (K)
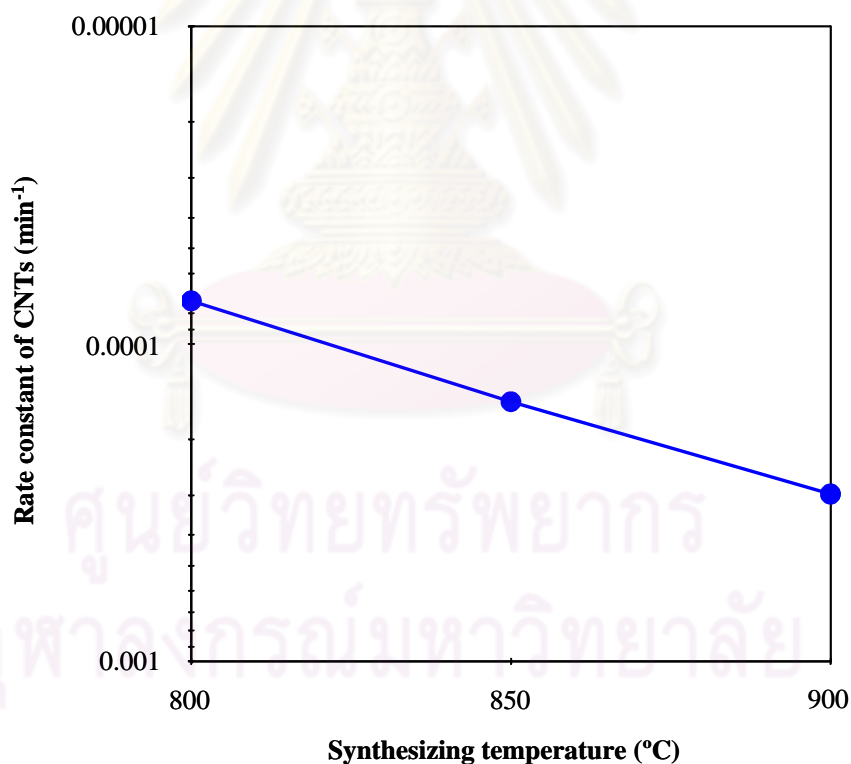
Figure 4.26 Rate constant of CNTs by varying synthesizing temperature

4.2.3 Effect of glycerol to ferrocene molar ratio

In this part, the effect of glycerol to ferrocene molar ratio on the quality and quantity of the synthesized carbon nanoparticles was studied at condition of synthesizing temperature of 800 ℃ and nitrogen flow rate of 350 mL/min.

Zone 1
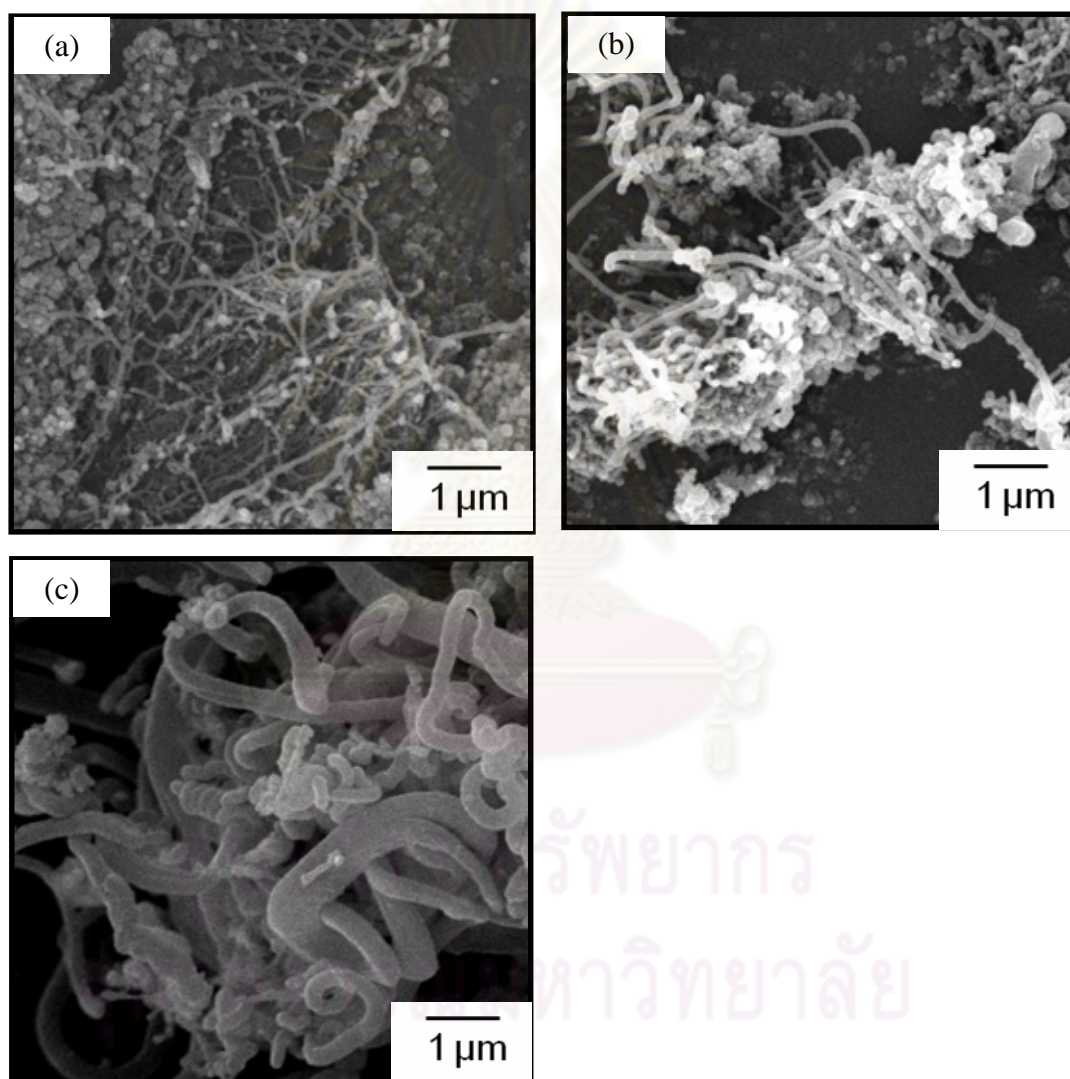
Figure 4.27 SEM images of the carbon nanoparticles deposited at zone 1 with different molar ratios of glycerol to ferrocene: (a) 5/1, (b) 10/1 and (c) 20/1.

SEM images as shown in Figure 4.27 revealed the carbon nanoparticles deposited at zone 1 with different molar ratios of glycerol to ferrocene. At the ratio of 5/1, the morphology of the synthesized carbon nanoparticles shown in

Figure 4.27(a) was uniform carpet-like MWCNTs with outer diameters of the tubes in range of 30-80nm. While, increasing of molar ratios of glycerol to ferrocene, the tubes with larger outer diameters were clearly observed. At the molar ratio of 10/1, the MWCNTs with outer diameter of the tubes in range of 50-125 nm were synthesized as shown in Figure 4.27(b). While at the molar ratio of 20/1, the tubes as shown in Figure 4.27(c) had the tube diameters larger than 250 nm.

Zone 2
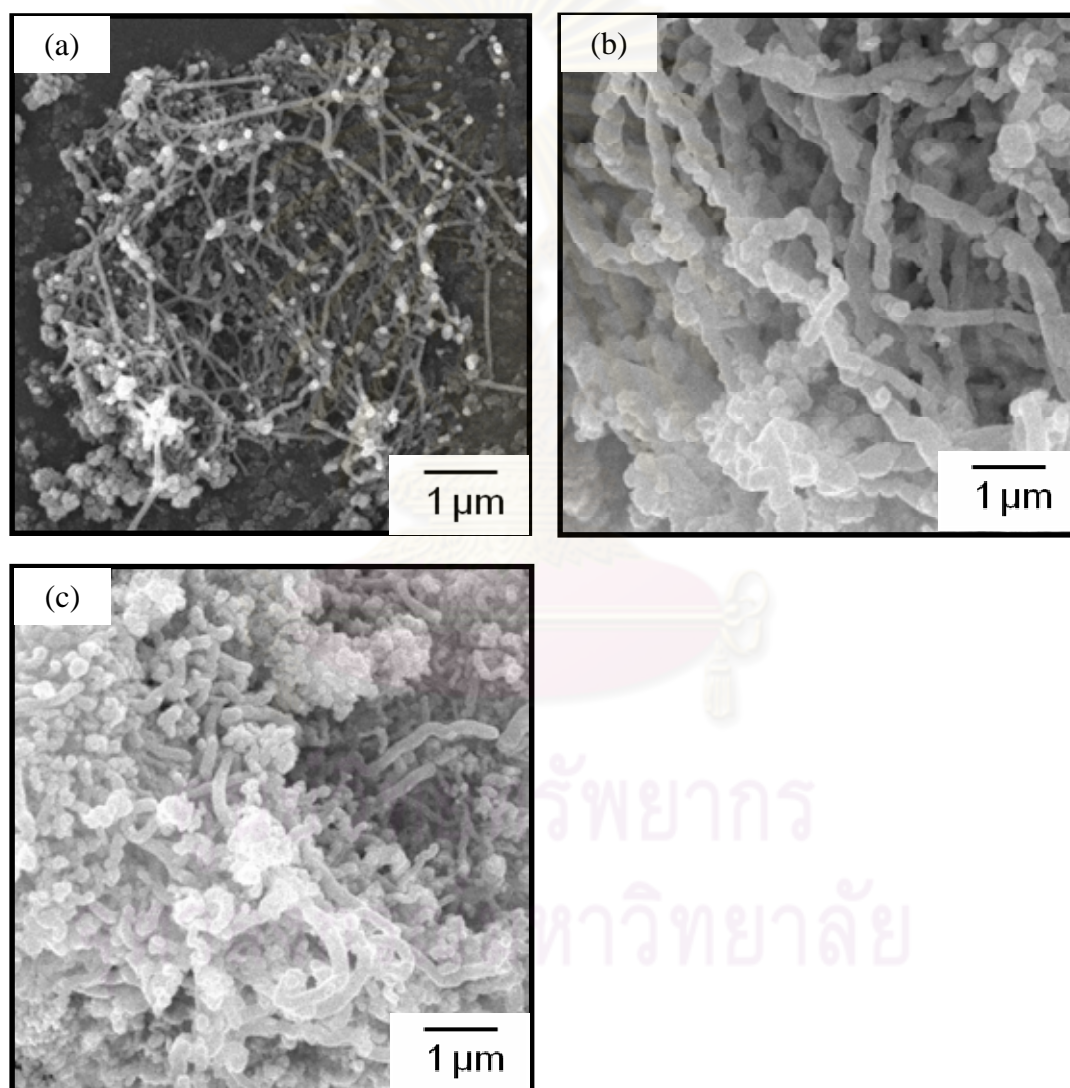
Figure 4.28 SEM images of the carbon nanoparticles deposited at zone 2 with different molar ratios of glycerol to ferrocene: (a) 5/1, (b) 10/1 and (c) 20/1.

SEM images as shown in Figure 4.28 revealed the carbon nanoparticles deposited at zone 2 with different molar ratios of glycerol to ferrocene.

At the ratio of 5/1, the synthesized carbon nanoparticles shown in Figure 4.28(a) were straight MWCNTs with outer diameters of the tubes in range of 40-80 nm. The MWCNTs at the ratio of 10/1 were synthesized which those outer diameters about 300 nm as shown in Figure 4.28(b). At the molar ratio of 20/1, the morphology of the synthesized carbon nanoparticles shown in Figure 4.28(c) was warm-like MWCNTs with outer diameters of the tubes in range of 100-250 nm, respectively.

Zone 3
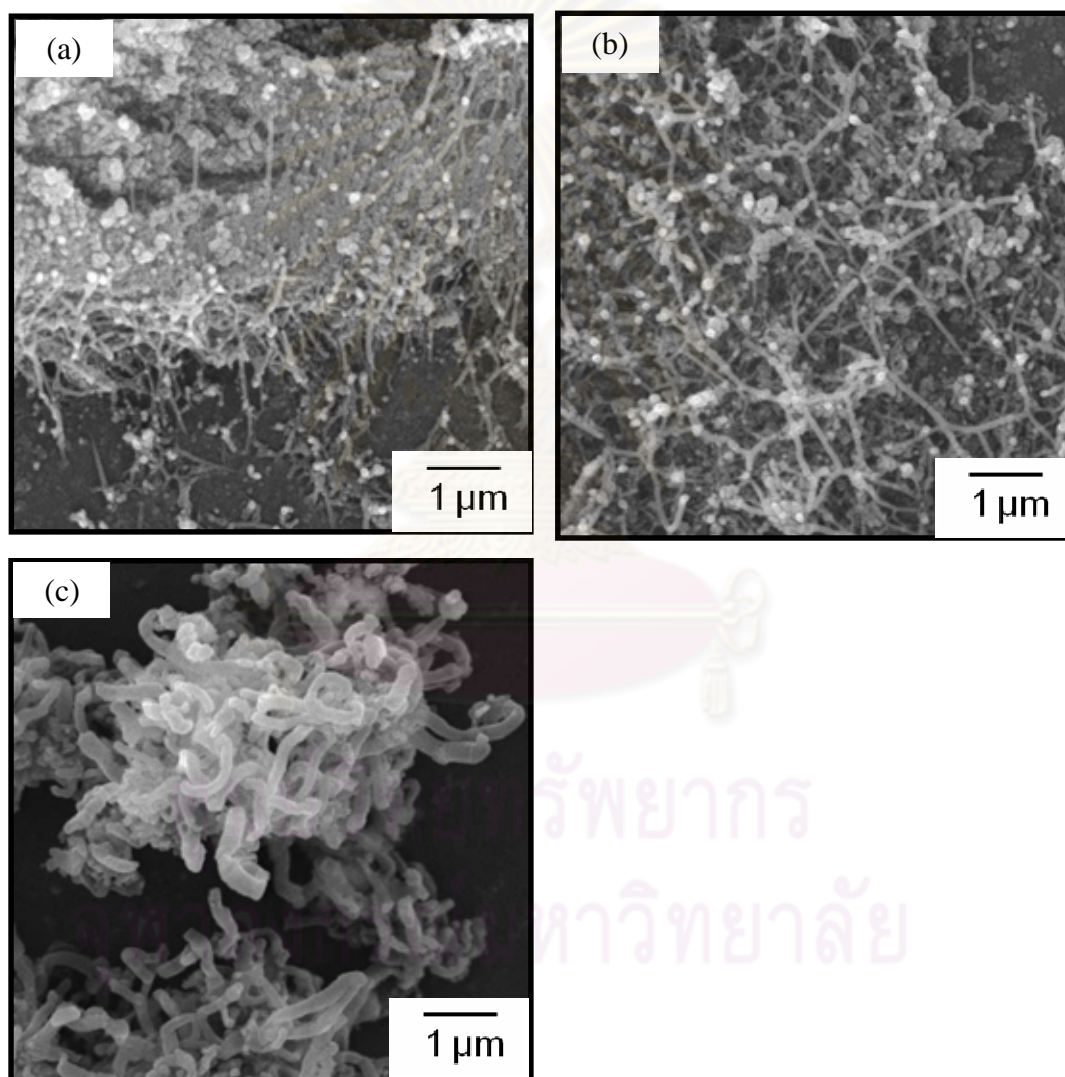
Figure 4.29 SEM images of the carbon nanoparticles deposited at zone 3 with different molar ratios of glycerol to ferrocene: (a) 5/1, (b) 10/1 and (c) 20/1.

SEM images the carbon nanoparticles deposited at zone 3 with different molar ratios of glycerol to ferrocene were shown in Figure 4.29. At the ratio

of 5/1, the morphology of the synthesized carbon nanoparticles shown in Figure 4.29(a) was the carpet-like MWCNTs with outer diameters of the tubes in range of 40-80 nm. The bigger diameters of the MWCNTs were synthesized at higher ratios of glycerol to ferrocene. At the ratio of 10/1, the straight MWCNTs with outer diameter of the tubes in range of 50-100 nm were synthesized as shown in Figure 4.29(b). While, at the ratio of 20/1, the curvature of MWCNTs with the outer diameters of the tubes about 125 nm were synthesized shown in Figure 4.29(c).

Raman spectra of the MWCNTs deposited at zone 1, zone 2 and zone 3 with different molar ratios of glycerol to ferrocene exhibited their strong responses of D peak and G peak. The I_D/I_G ratios of the synthesized MWCNTs with different molar ratios of glycerol to ferrocene were shown in Figure 4.30.
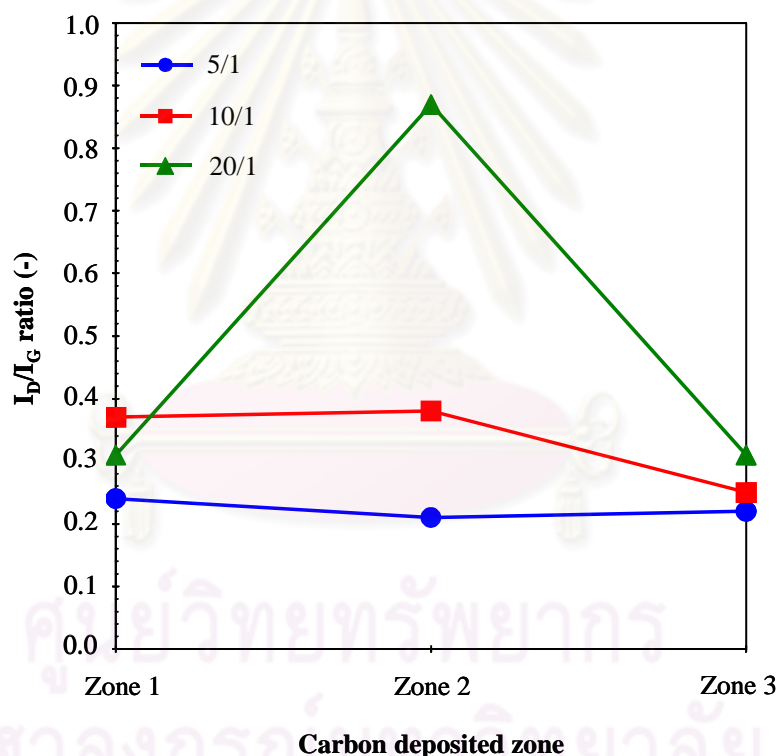
Figure 4.30 I_D/I_G ratios of the synthesized MWCNTs at different molar ratios of glycerol to ferrocene.

The I_D/I_G ratios revealed that the molar ratio of glycerol to ferrocene also strongly affected on crystallinity and purity of the synthesized carbon nanoparticles. At the molar ratio of 5/1, the I_D/I_G ratios of the carbon nanoparticles deposited at zone 1, zone 2 and zone 3 were 0.24, 0.21 and 0.22, respectively. It could

be observed that the I_D/I_G ratios of the carbon nanoparticles synthesized at higher ratio of glycerol to ferrocene were increased, especially the carbon nanoparticles deposited at zone 2 with the molar ratio of 20/1. At the molar ratio of 10/1, the I_D/I_G ratios of the carbon nanoparticles deposited at zone 1, zone 2 and zone 3 were 0.37, 0.38 and 0.25, respectively. While, at the molar ratio of 20/1, the I_D/I_G ratios of the carbon nanoparticles at zone 1, zone 2 and zone 3 were 0.31, 0.87 and 0.31, respectively. Therefore, in this work, the molar ratio of 5/1 was found to be the optimal ratio for the synthesis of the MWCNTs.

The carbon yields of the synthesized carbon nanoparticles at different molar ratios of glycerol to ferrocene were shown in Figure 4.31. At the molar ratio of glycerol to ferrocene was 5/1, the carbon yield was 2.2 %. The yield was decreased to 1.9 and 1.5 % when the molar ratio was increased to 10/1 and 20/1, respectively.
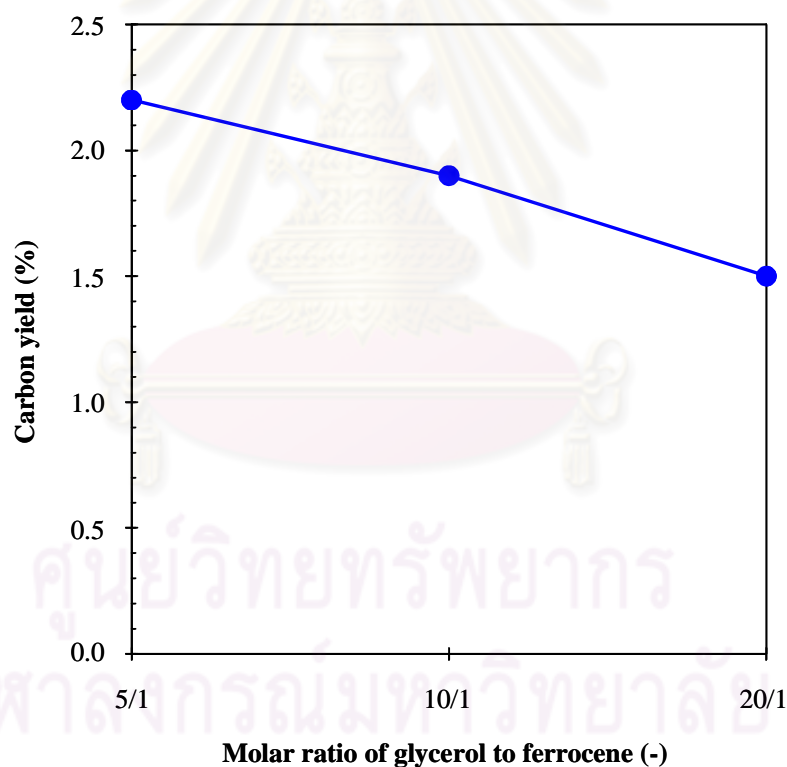
Figure 4.31 Yields of the synthesized carbon nanoparticles at different molar ratios of glycerol to ferrocene.

It is well known that catalytic nanoparticles such as Fe, Ni and Co and their mixture, are very important for the formation of the CNTs. The formation of the CNTs consists of diffusion and dissolution of carbon atom into the catalytic

nanoparticles, and precipitation to form the tubes, respectively. The diffusion and precipitation processes are competitor for each other. It means that if the diffusion process takes place with its rate slower than that of the precipitation process, the diffusion process is rate limiting step, leading to continuous CNT formation with less amount of amorphous carbon. On the other hand, the precipitation process is rate limiting step if the rate of precipitation takes place slower than the rate of diffusion. Therefore, at first, continuous feeding of the carbon atoms into the catalytic particles makes the formation of the CNTs with larger diameters. Finally, the continuous feeding leads excess amount of the carbon atoms into the catalytic nanoparticles. Therefore, the catalytic nanoparticles are not active, leading to the formation of shorter and larger diameters of the CNTs and also amorphous carbon can be taken place.

In this part, the C atoms were 15, 30 and 60 times to Fe atoms when the molar ratio of glycerol to ferrocene was 5/1 to 10/1 and 20/1, respectively which the atomic ratio of C to Fe was significantly increased. At higher molar ratio of glycerol and ferrocene, especially in case of the ratio of 20/1, the carbon atoms was too much, leading to the tubes had larger diameters and shorter than those at the molar ratio of 5/1. Therefore, it was possible to conclude that the formation of the MWCNTs at the ratio of 20/1 was controlled by the precipitation process which could be confirmed by SEM images and the I_D/I_G ratios.

Although diffusion of the C atoms was increased at higher molar ratio of glycerol to ferrocene, the yield of the synthesized carbon products was decreased. The increasing of the C atoms with the same of the Fe atoms increased the diffusion rate of the C atoms. When the diffusion was much faster than the precipitation of the C atoms to form the tubes, poisoning of the Fe particles took place, which the Fe particles were not activate the C atoms to form the tube. The remaining of the C atoms could not dissolve into the Fe particles, leading to, the tubes were not formed. Therefore, the yield of the synthesized products was decreased at higher molar ratio of glycerol to ferrocene.
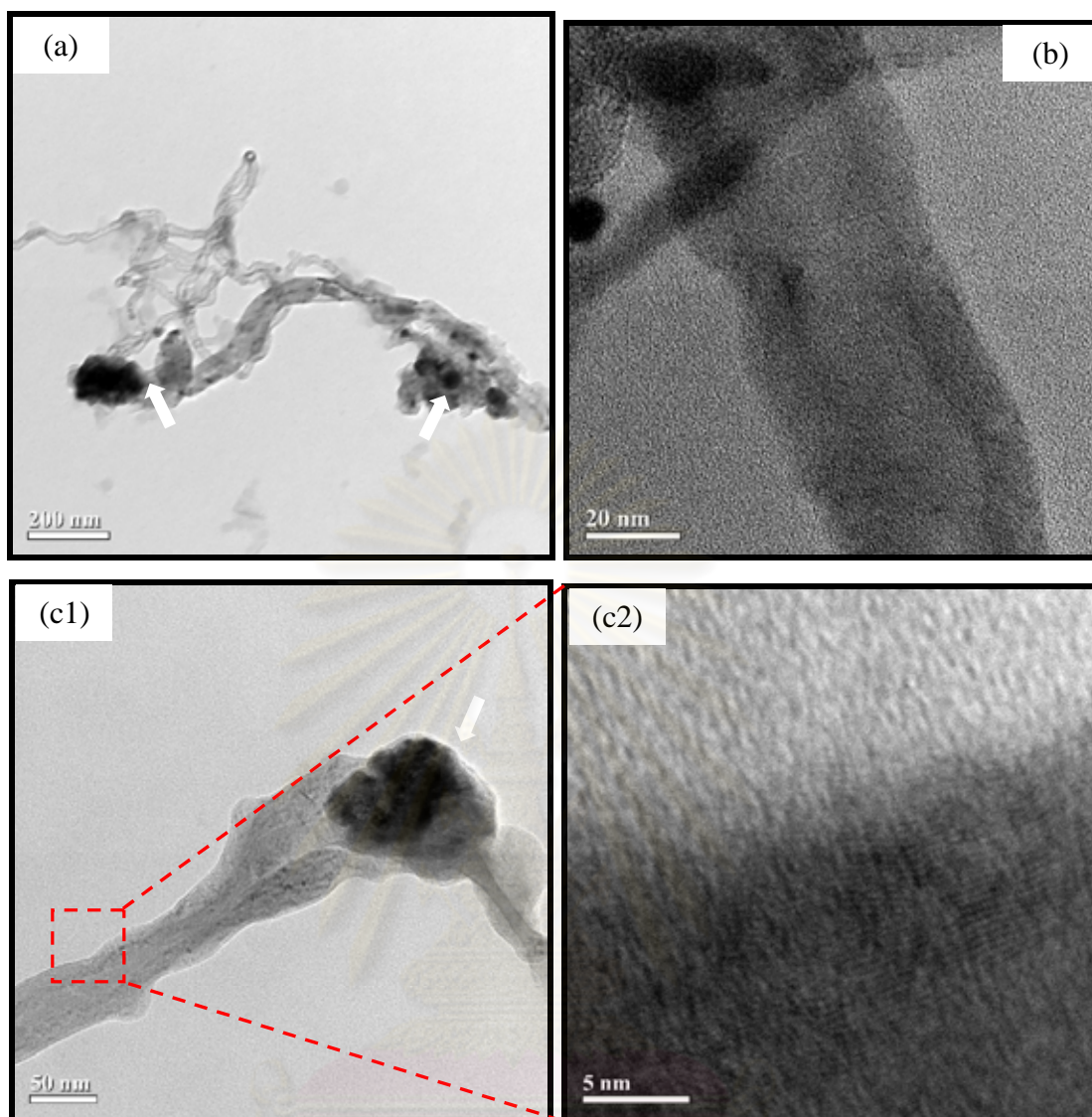
Figure 4.32 TEM images of the synthesized MWCNTs under the condition of the nitrogen flow rate of 350 mL/min, the synthesizing temperature of 800 ºC and the molar ratio of glycerol to ferrocene of 5/1 at different deposited positions: (a) zone 1, (b) zone 2 and (c1) and (c2) zone 3.

TEM images of the MWCNTs deposited at different positions within the quartz tube reactor were shown in Figure 4.32. Fe nanoparticles, indicated with arrowhead, were at the one tip of the MWCNTs. High magnified TEM image of the MWCNTs as shown Figure 4.32(c2) revealed the tubes were made of parallel graphene planes oriented along the tube axis with the interplanar distance between two adjacent graphene planes about 0.34 nm which is close to that of the (002) interplanar distance in graphite, i.e. 0.335 nm. Furthermore, it could be clearly observed the amorphous carbon covered on the outer wall of the tubes.

XRD patterns of the synthesized MWCNTs shown in Figure 4.33 consisted of X-ray diffraction peak at 26.3° could be assigned to the (002) planes of hexagonal graphite structure with an interplanar distance of 0.35 nm while another peak at 43.7 ° indicates that the iron nanoparticles exhibited the (111) plane of the face-centered cubic (fcc) γ-Fe. In addition, it could also be observed the existence of Fe were body-centered cubic (bcc) α-Fe (110) at 44.7° (Cheng et al., 2009). Furthermore, a large fraction of orthorhombic cementite Fe$_3$C phase was also found in the XRD patterns.
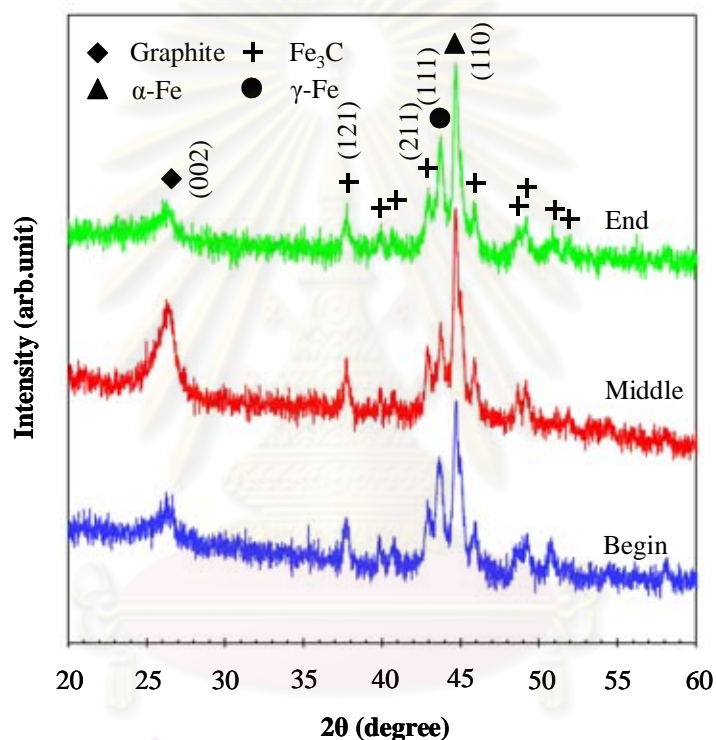
Figure 4.33 XRD patterns of the synthesized MWCNTs under the condition of the nitrogen flow rate of 350 mL/min, the synthesizing temperature of 800 ºC and the molar ratio of glycerol to ferrocene of 5/1 at different deposited positions.

From Fe-C phase diagram as shown in Figure 4.34, it could be clearly seen that γ-Fe (in γ phase and γ + Fe$_3$C phase) were mostly transformed into α-Fe during the cooling down phase because α-Fe is the thermodynamically stable phase at room temperature (Cheng et al., 2009). This phenomenon was consistent with the appearance of small fraction of the γ-Fe compared to the α-Fe in the XRD patterns as shown in Figure 4.33. While the Fe$_3$C is not stable at high temperature, therefore, the decomposition of the carbide into α-Fe and C atoms was occur, leading to the

precipitation of the C atoms to form the CNTs at the surface of the Fe particles (Snoeck, Froment and Fowles, 1997).
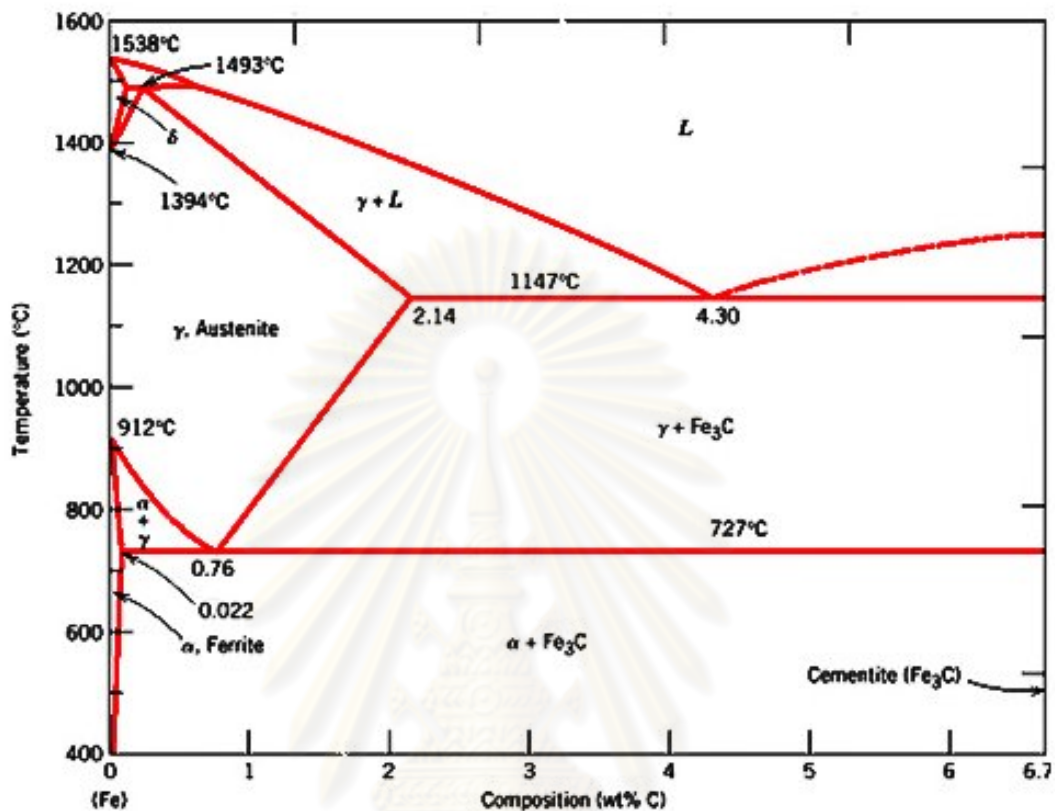
Figure 4.34 Fe-C phase diagram

(http://www.docstoc.com/docs/56224939/Iron-Carbon-Phase-Diagram-(a-review)-see-Callister-Chapter-9).

4.2.4 Possible mechanisms

Based on above experimental results, it could be realized that the formation mechanisms of the carbon nanoparticles was strongly dependence on the existence of the Fe catalytic nanoparticles generated from decomposition of ferrocene as well as their diffusion, dissolution and precipitation processes. The formation mechanisms, proposed here, was believed that vapor-liquid-solid (VLS) growth mechanisms of carbon catalyzed by molten Fe nanoparticles consists of diffusion, dissolution and precipitation of the carbon atoms (Weissker et al., 2010) as shown in Figure 4.35. At first, the mixture of glycerol and ferrocene as the carbon and Fe precursors was vaporized by heat transfer from the electrical furnace. The vaporized

precursors were instantly introduced by nitrogen gas into the maximum temperature zone, simultaneously with decomposition of the vaporized precursors to form carbon and Fe vapors. The Fe vapors initially formed nuclei, after that the nuclei condensed and coagulated to form molten Fe particles, respectively. The C vapors around the molten Fe diffused on the surface of the molten Fe and dissolved until saturation inside the Fe particles, leading to form γ-Fe and an intermetallic compound of metastable Fe_3C in carbon diffusion, dissolution and saturation of carbon process, respectively. The γ-Fe and Fe_3C were then transformed and decomposed into α-Fe and C atoms, respectively. Finally, the C atoms were precipitated to form the CNTs at the surface of the Fe particles.

Referring to these experimental results of the synthesis of the SWCNTs by laser ablation of C/Ni/Co rod and the MWCNTs by CVD of glycerol and ferrocene, it could be clearly observed that the formation mechanisms of both CNTs (SWCNTs and MWCNTs) were vapor-liquid-solid (VLS) mechanisms, although their carbon and catalyst sources were produced differently. Furthermore, it also revealed that the formation mechanisms of the CNTs consist of the diffusion, dissolution and precipitation processes. The dissolution of the C atoms into the catalytic metals was related to solubility of the C atoms into the metals to form carbon-metal alloys. Therefore, selection of proper catalyst for the synthesis of the CNTs was significantly considered.
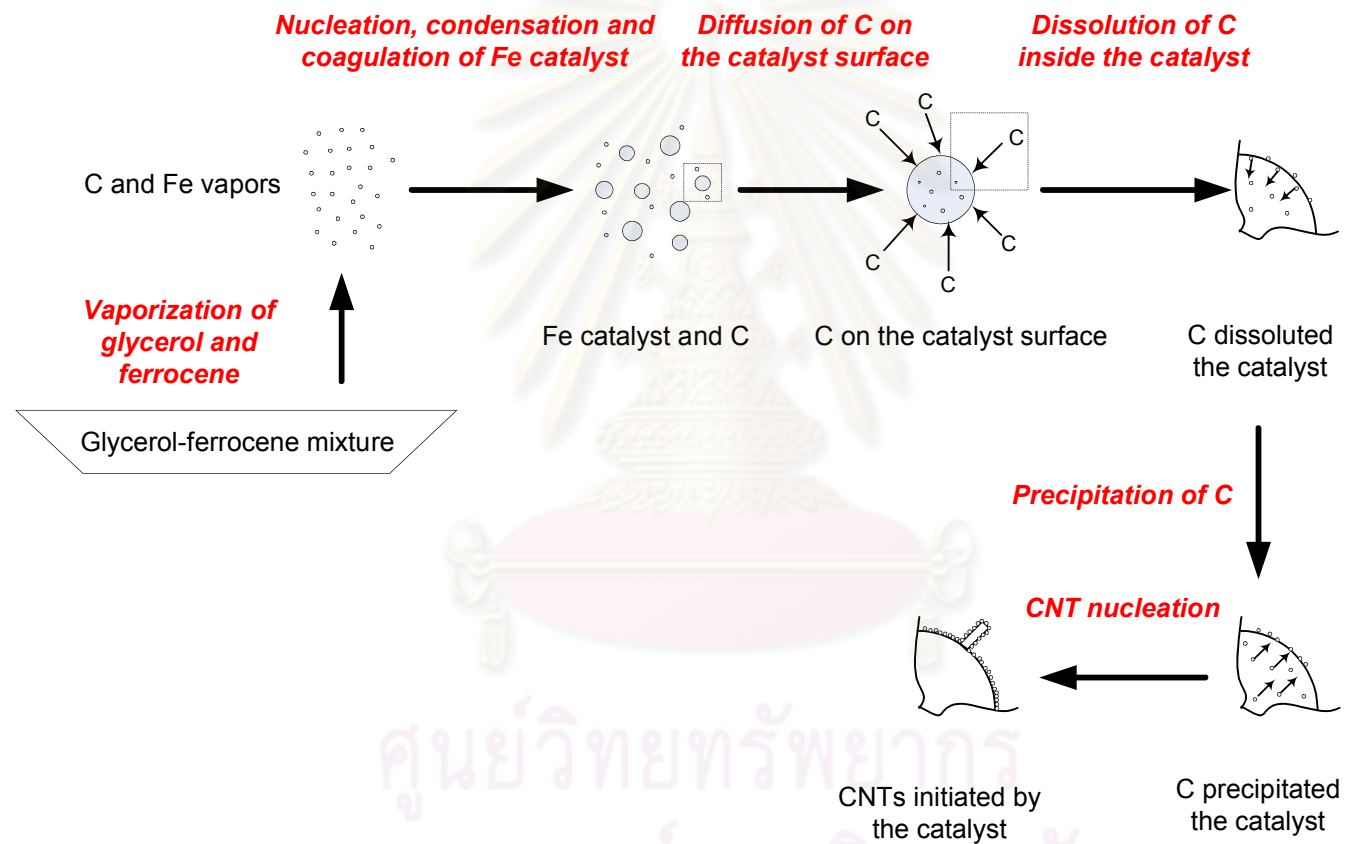
Figure 4.35 Vapor-liquid-solid mechanisms of the formation of the MWCNTs by CVD of glycerol and ferrocene.

4.3 Synthesis of the ZnO nanoparticles by oxidation of Zn

Referring to many experimental results reported in other previous works, this part has set its aim to study effect of synthetic parameters on the morphology, size and yield of the ZnO nanoparticles synthesized by the oxidation of pure Zn powder. Effect of synthesizing temperature, nitrogen flow rate and oxygen flow rate on the morphology, size and yield of the synthesized ZnO nanoparticles were thoroughly investigated and then reported and discussed in this part.

From the previous part of the synthesis of the carbon nanoparticles (see page 56), it could be clearly observed that the temperature gradients and velocity gradients took place throughout the quartz tube reactor and could affect on the formation of the carbon nanoparticles, leading to the study of the synthesized carbon nanoparticles at 3 different zones including zone 1 (0-15 cm from inlet) where the temperature increased from the lowest to the highest, zone 2 (15-45 cm from inlet) where the temperature was the highest and zone 3 (45-60 cm from inlet) where the temperature decreased from the highest to the lowest. In this part, the temperature gradients and velocity gradients could also affect on the formation of the ZnO nanoparticles. Therefore, the synthesized ZnO nanoparticles were also distinguish studied into 3 zones as zone 1, zone 2 and zone 3. However, it should be noted that few ZnO nanoparticles deposited at zone 1. Therefore, in this part, the synthesized ZnO nanoparticles were only studied at zone 2 and zone 3.

4.3.1 Effect of nitrogen flow rate

The effect of nitrogen flow rate on the formation of the synthesized ZnO nanoparticles was studied in a range of 200, 350 and 500 mL/min under condition of the synthesizing temperature of 800 ℃ and O_2 flow rate of 100 mL/min.
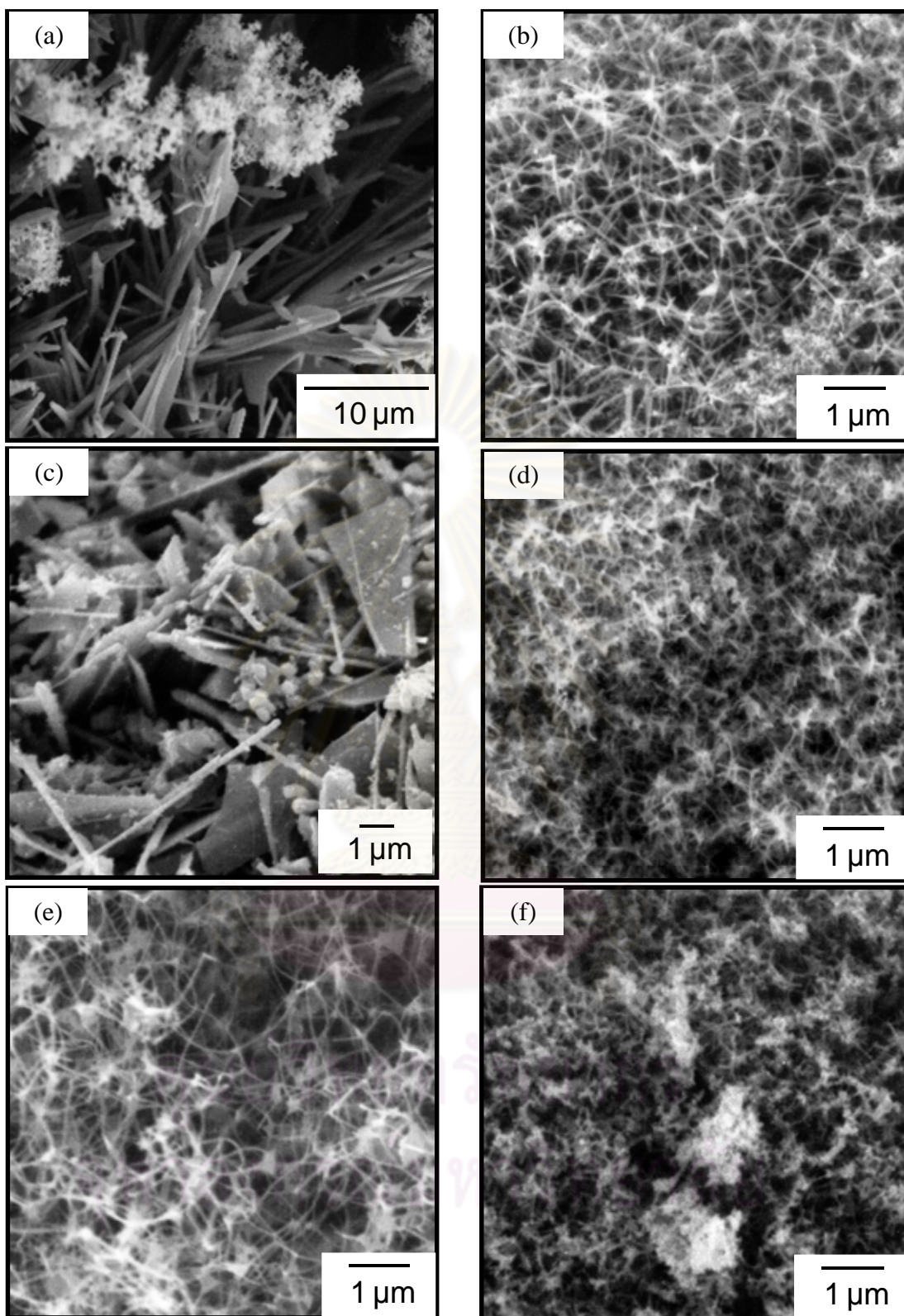
Figure 4.36 The synthesized ZnO deposited at zone 2 and zone 3 with different N_2 flow rates: (a) and (b) 200 mL/min, (c) and (d) 350 mL/min and (e) and (f) 500 mL/min.

Morphologies of the ZnO nanoparticles deposited at the zone 2 and zone 3 with different nitrogen flow rates were shown in Figure 4.36. At nitrogen flow rate of 200 mL/min, the synthesized ZnO deposited at zone 2 as shown in Figure 4.36(a) was rod-like microstructure with the diameter about 100 nm and the length more than 10 um. Furthermore, few amount of agglomerated nanoparticle was also found. While, the synthesized ZnO deposited at zone 3 as shown in Figure 4.36(b) was uniform tetrapod nanostructure with the diameters and length of pod about 60-80 nm and 500-600 nm, respectively.

At nitrogen flow rate of 350 mL/min, the morphology of ZnO deposited at zone 2 as shown in Figure 4.36(c) was combination of various structures including spherical particles with diameters more than 200 nm, rod-like microstructure with the diameter about 100 nm and the length more than 5 um and micro-sheets. While, the ZnO deposited at zone 3 as shown in Figure 4.36(d) was uniform tetrapod nanostructure with the diameters and length of pod about 50-60 nm and 320-340 nm, respectively.

At nitrogen flow rate of 500 mL/min, the morphology of ZnO deposited at zone 2 and zone 3 as shown in Figure 4.36(e) and (f), respectively was the same morphology of tetrapod ZnO. However, their diameter and length were significantly different. The diameter and length of the ZnO deposited at zone 2 were about 30-40 nm and more than 800 nm, respectively. While those of the ZnO deposited at zone 3 were about 50-60 nm and 160-180 nm, respectively.

It could be clearly observed that the nitrogen flow rate affected on the morphologies of the ZnO deposited on the zone 2 of the quartz tube reactor. While the nitrogen flow rate did not affect on the morphology but on the diameters and length of the tetrapod ZnO deposited at zone 3 which were significantly decreased.

ZnO yields could be defined in equation 4.6

$$ZnO\ yield\ (\%) = \frac{W_{ZnO,2} + W_{ZnO,3}}{W_{Zn}} \times 100 \tag{4.6}$$

where $W_{ZnO,2}$ = Weight of synthesized ZnO at zone 2

                     $W_{ZnO,3}$ = Weight of synthesized ZnO at zone 3

Yields of the synthesized ZnO nanoparticles at different nitrogen flow rates were shown in Figure 4.37. At the nitrogen flow rate of 200 mL/min, the ZnO yield was 61 %. While the yield significantly decreased as 52 and 37 % at the nitrogen flow rate of 350 and 500 mL/min, respectively.
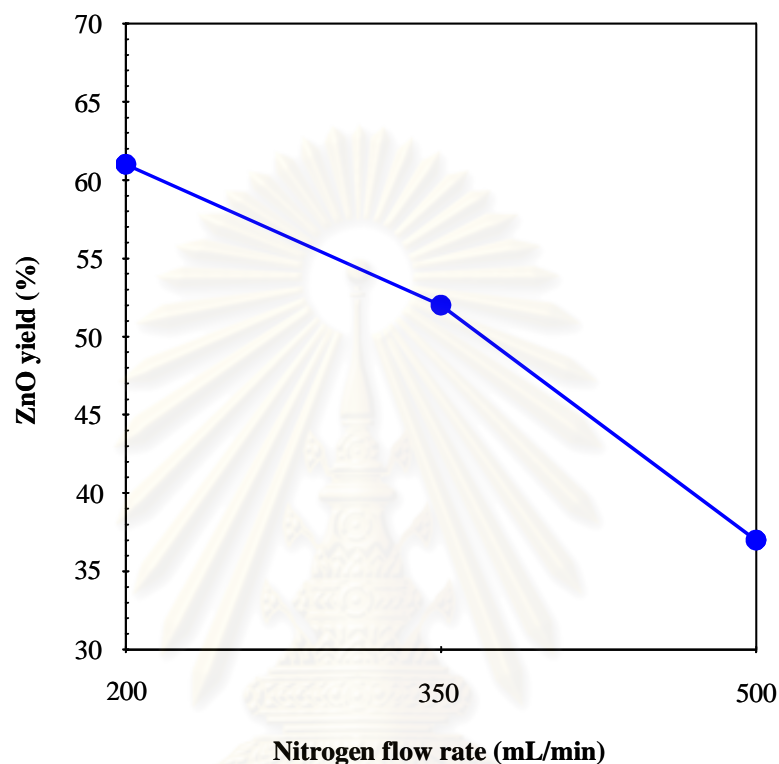
Figure 4.37 Yields of the synthesized ZnO nanoparticles at different nitrogen flow rates.

The nitrogen flow rate was found to be a main parameter of this study which direct affected to the formation of the synthesized ZnO nanostructures. Increase in the nitrogen flow rate decreased residence time within the quartz tube reactor. Furthermore, increase in the nitrogen flow rate also diluted oxygen, leading to partial pressure of oxygen was decreased.
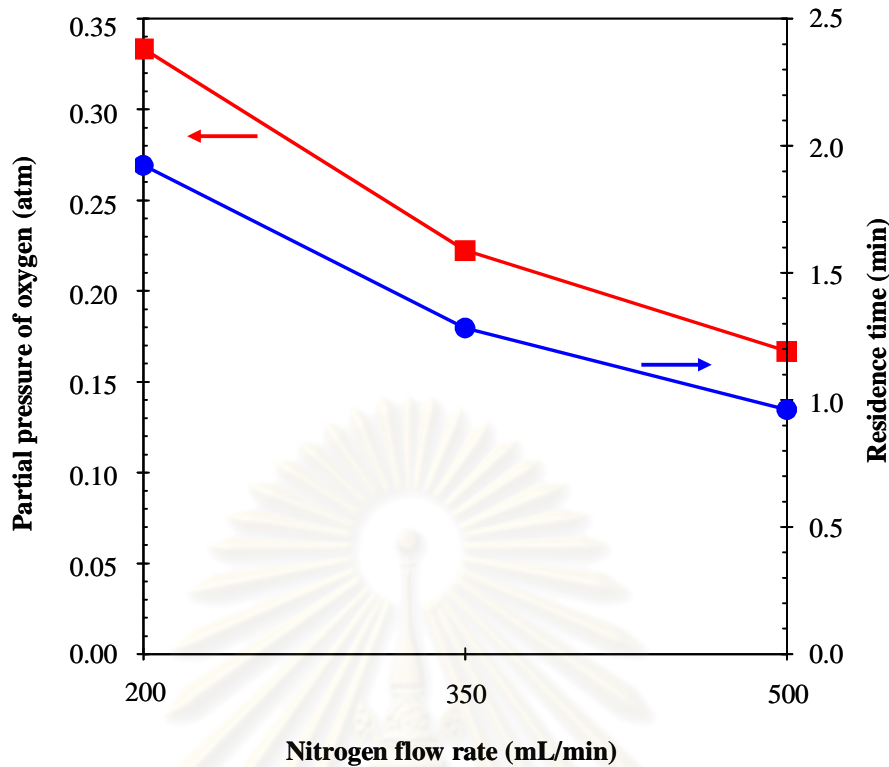
Figure 4.38 Partial pressure of oxygen and residence time by varying nitrogen flow rate.

The partial pressure of oxygen inside the quartz tube reactor was decreased from 0.33 to 0.22 and 0.17 atm, while residence time was also decreased from 1.9 to 1.3 and 1.0 min when the nitrogen flow rate was increased from 200 to 350 and 500 mL/min, respectively as shown in Figure 4.38.

The ZnO could be synthesized by oxidation of zinc as shown in equation 4.7.

$$Zn \ (s) + 1/2O_2 \rightarrow ZnO \ (s) \tag{4.7}$$

From kinetic consideration (Delalu et al., 2000), conversion of the synthesized ZnO from the oxidation can be defined by expression 4.8.

$$\alpha = \frac{m_{Zn}^0 - m_{Zn}^t}{m_{Zn}^0} \tag{4.8}$$

where　　　α　=　Conversion of the ZnO

$$m^0_{Zn} = \text{Initial mass of zinc } (t = 0)$$

$$m^t_{Zn} = \text{Mass of zinc at time t } (t > 0)$$

The experiments were assumed isothermally. Furthermore, Zn was also approximated as spherical particles. Under the conditions, designation by r_0, r_1 and r_2, the initial radius of Zn particle, of the reaction interface (metal/oxide) and of the oxide layer, respectively as shown in Figure 4.39.
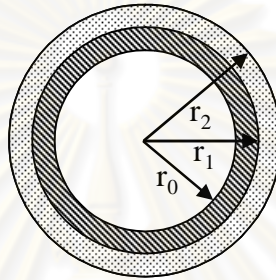
Figure 4.39 Diffusion of oxygen through Zn spherical particle.

We demonstrate the following relations:

$$r_1 = r_0 (1 - \alpha)^{1/3} \tag{4.9}$$

$$r_2 = r_0 (1 + \alpha(\Delta - 1))^{1/3} \tag{4.10}$$

$$\Delta = \frac{V_{ZnO}}{V^0_{Zn} - V_{Zn}} \tag{4.11}$$

where Δ = Coefficient of Pilling and Bedworth (Moore et al., 1962)

V_{ZnO} = Volume of ZnO

V^0_{Zn} = Initial volume of Zn

V_{Zn} = Volume of Zn

The conversion, α, could be derived with respect to time as shown in equation 4.12.

$$\frac{d\alpha}{dt} = -\frac{2}{m_{Zn}^0}\frac{dm_{O_2}}{dt} \tag{4.12}$$

Assuming, the diffusion of the reactants through the thickness of the oxide layer was the limiting factor. Fick's Law of O_2 as shown in equation 4.13, respectively are substituted into equation 4.12.

$$N_{O_2}S_1 = -D_{O_2}S_1\left\{\frac{dC_{O_2}}{dr}\right\}_{r=r_1} \tag{4.13}$$

where

N_{O_2} = Diffusion flux of O_2

D_{O_2} = Diffusion coefficient

S_1 = Surface area of the reaction interface = $4\pi r_1^2$

$\left\{\dfrac{dC_{O_2}}{dr}\right\}_{r=r_1}$ = Local concentration gradient of O_2

Therefore, equation 4.12 could be reduced into following rate equation as shown in equation 4.14:

$$\frac{d\alpha}{dt} = \frac{2}{m_{Zn}^0}D_{O_2}4\pi r_1^2\left\{\frac{dC_{O_2}}{dr}\right\}_{r=r_1} \tag{4.14}$$

The relation could be integral if r_1 and the concentration gradient of O_2 at $r = r_1$ are expressed as function of α. From the lack of accumulation of reactant in the reaction zone (steady-state hypothesis), equation 4.14 could be deduced into equation 4.15.

$$r^2\left\{\frac{dC_{O_2}}{dr}\right\} = r_1^2\left\{\frac{dC_{O_2}}{dr}\right\}_{r=r_1} \tag{4.15}$$

From the limiting conditions;

(i) $C_{O_2} = C_{O_2}^i = 0$ for $r = r_1$ where i is initial condition

(ii) $C_{O_2} = C_{O_2}^e$ for $r = r_2$ where e is equilibrium condition

Therefore, local concentration gradient of O_2 could be deduced as shown in equation 4.16.

$$\left\{ \frac{dC_{O_2}}{dr} \right\}_{r=r_1} = \frac{r_2}{r_1(r_2 - r_1)} C_{O_2}^e \tag{4.16}$$

Substitution of equation 4.16 into equation 4.14, a differential equation dependence only on the variables α and t could be obtained as shown in equation 4.17.

$$\frac{d\alpha}{dt} = \frac{8\pi D_{O_2} C_{O_2}^e}{m_{Zn}^0} \left[\frac{1}{r_0(1-\alpha)^{1/3}} - \frac{1}{r_0(1-\alpha(\Delta - 1))^{1/3}} \right] \tag{4.17}$$

After integration, the final equation could be obtained as shown in equation 4.18.

$$\frac{\Delta}{\Delta - 1} - (1-\alpha)^{2/3} - \frac{1}{\Delta - 1}\left[1 + \alpha(\Delta - 1)\right]^{2/3} = \frac{D_{O_2} C_{O_2}^e}{d_{Zn} r_0^2} \tau \tag{4.18}$$

where d_{Zn} =   Density of Zn

One can define:

$$k_{Zn}^0 = \frac{D_{O_2} C_{O_2}^e}{d_{Zn} r_0^2} \tag{4.19}$$

k_{Zn}^0 is proportional to the diffusion constant, could be related to the observed rate constant of the reaction (Delalu et al., 2000). Therefore, the time necessary to totally consume Zn ($\alpha = 1$) was equal to:

$$\tau = \frac{1}{k_{Zn}^0} \frac{\Delta}{\Delta - 1} \left[1 - \frac{[1 + \alpha(\Delta - 1)]^{2/3}}{\Delta} \right] \tag{4.20}$$

The necessary time as shown in equation 4.20 was function of various parameters including conversion of the ZnO or α. Therefore, increase in nitrogen flow rate or decrease in residence time resulted in lower diffusion of O_2 into the surface of the Zn spherical particles, leading to decrease in diameters and length of the ZnO pods.

4.3.2 Effect of synthesizing temperature

In this part, the effect of synthesizing temperature at 800, 850 and 900 ºC on the formation of the synthesized ZnO was studied at constant N_2 flow rate of 500 mL/min and O_2 flow rate of 100 mL/min.

At synthesizing temperature of 800 ºC, the ZnO deposited at zone 2 shown in Figure 4.40(a) was tetrapod ZnO structure with diameters and length of pod about 30-40 nm and more than 800 nm, respectively. While, the ZnO deposited at zone 3 as shown in Figure 4.40(b) was also tetrapod nanostructure with smaller diameters and shorter length of pod about 50-60 and 160-180 nm, respectively.

As same as the results of the ZnO synthesized at the synthesizing temperature of 800 ºC, the morphology of the synthesized ZnO at the synthesizing temperature of 850 ºC was also tetrapod ZnO structure shown in Figure 4.40(c) and (d). The diameters and length of the pod from the zone 2 as shown in Figure 4.40(c) were about 100 nm and 500-600 nm, respectively. While, those of the pod at zone 3 as shown in Figure 4.40(d) were about 50-60 and 440-560 nm, respectively.
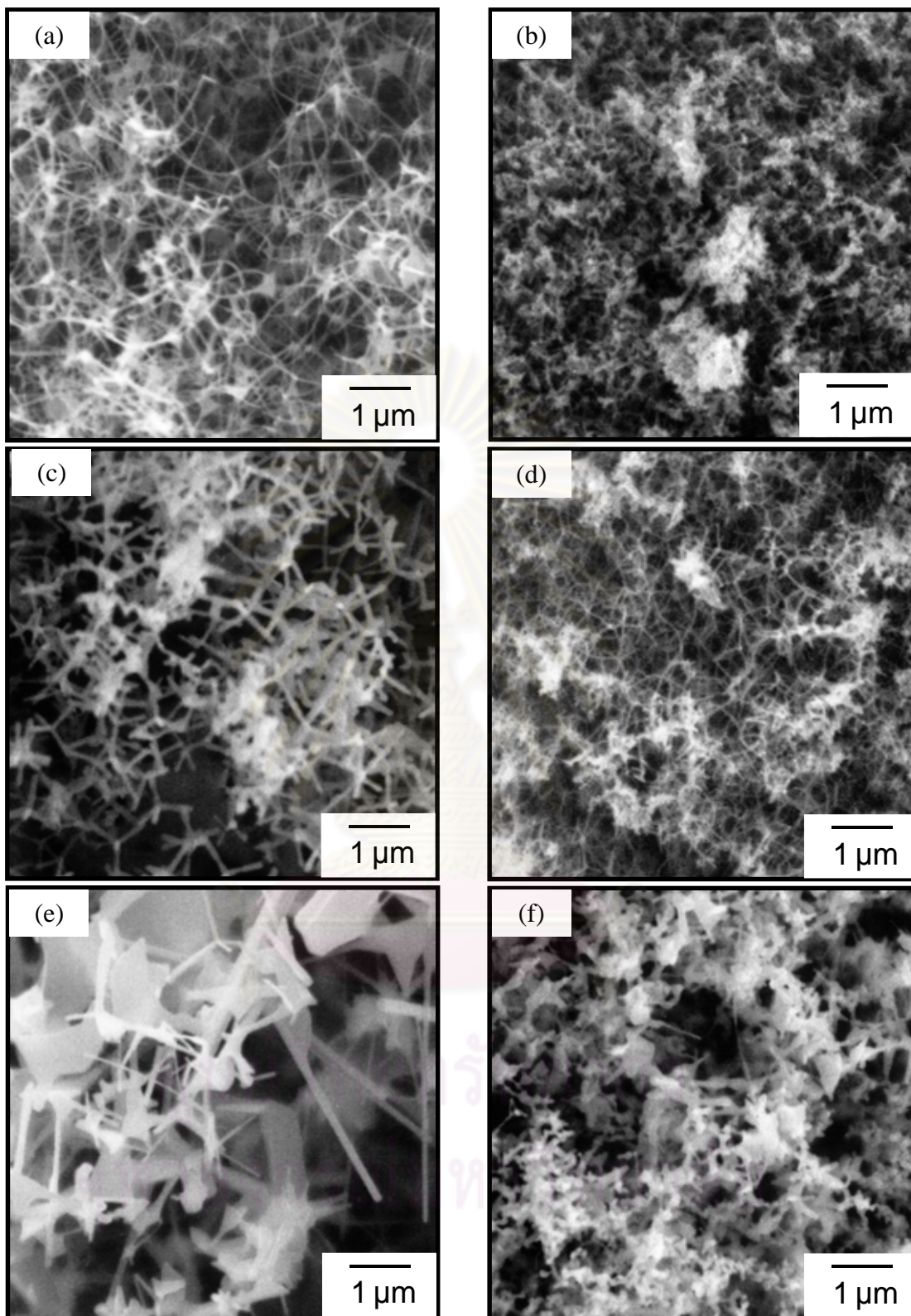
Figure 4.40 The synthesized ZnO deposited at zone 2 and zone 3 with different synthesizing temperatures: (a) and (b) 800 ℃, (c) and (d) 850 ℃ and (e) and (f) 900 ℃.

At synthesizing temperature of 900 ºC, the morphology of the ZnO deposited at zone 2 and zone 3 as shown in Figure 4.40(e) and (f), respectively were significantly different. The morphology of the ZnO deposited at zone 2 shown in Figure 4.40(e) was combination of various structures such as rod-like structure with the diameters about 100 nm and length about 3 um, micro-sheets and tetrapod structure. These might be caused by overgrowth of lamellae (Zhou, Liu and Hu, 2005) which can take place at high synthesizing temperature. While the morphology of ZnO deposited at zone 3 as shown in Figure 4.40(f) was agglomerated particles with primary diameters about 100-200 nm. Furthermore, few amount of rod-like structure was also found.

It was clearly observed that the ZnO deposited at zone 2 and zone 3 was still tetrapod structure although the synthesizing temperature was increased from 800 to 850 ºC. However, the increasing of these temperatures resulted inn increasing of the diameters and length of the pod of ZnO. While the morphologies of the ZnO synthesized at the synthesizing temperature of 900 ºC was significant changed.
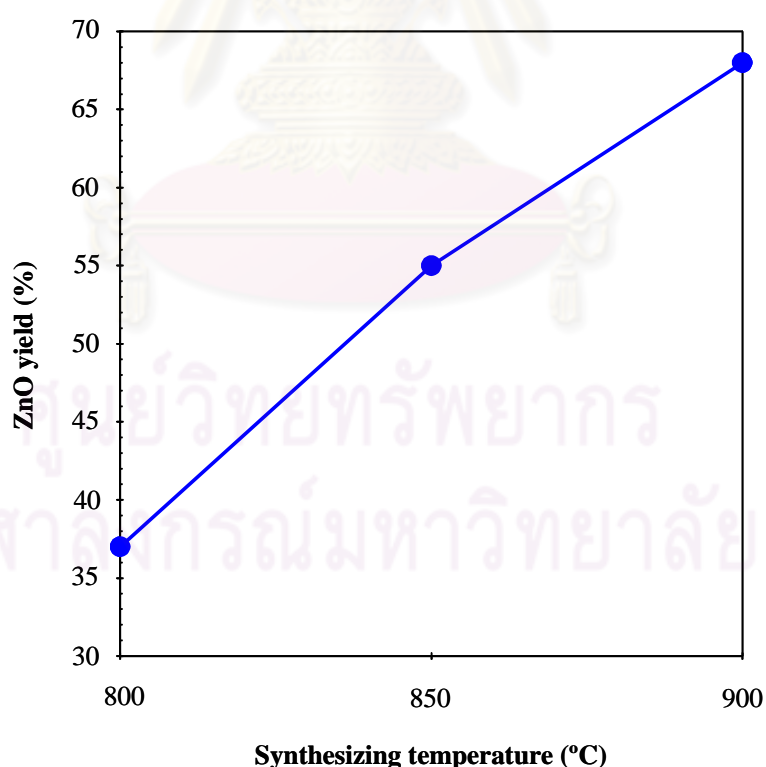
Figure 4.41 Yields of the synthesized ZnO nanoparticles at different synthesizing temperatures

Yields of the synthesized ZnO nanoparticles at different synthesizing temperatures were shown in Figure 4.41. At the synthesizing temperature of 800 ℃, the ZnO yield was 37 %. While the yield significantly increased as 55 and 68 % at the synthesizing temperatures of 850 and 900 ℃, respectively.

Rate constant of zinc oxidation (Delalu et al., 2000) shown in equation 4.21 revealed that increase in the synthesizing temperature exhibited rate constant of zinc as shown in Figure 4.42. Therefore, the increase in the synthesizing temperature could promote the reaction rate of ZnO formation.

$$-\ln k_{Zn} = -10.3 + 1.56 \times \frac{10^4}{T} \hspace{2cm} (4.21)$$

where k_{Zn} = Rate constant of zinc oxidation (min^{-1})

 T $\phantom{k_{Zn}}$ = Synthesizing temperature (K)
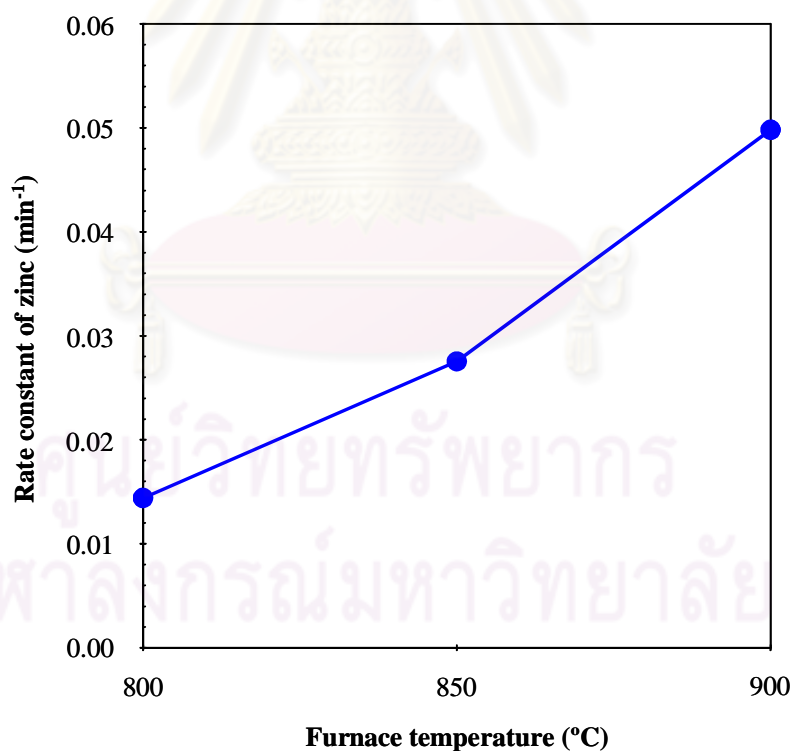
Figure 4.42 Rate constant of zinc by varying synthesizing temperature.

From above experimental results, morphology of synthesized ZnO nanoparticles changed from tetrapod structure to combination of various structures

such as rod-like structure, micro-sheet and tetrapod structure as shown in Figure 4.40(e) and agglomerated particles with rod like structure as shown in Figure 4.40(f) when the synthesizing temperature were changed from 800 and 850 ºC to 900 ºC. Therefore, morphology, size and yield of the synthesized ZnO depend upon partial pressure of zinc vapor and kinetic reaction of ZnO.

4.3.3 Effect of oxygen flow rate

In this part, the effect of oxygen flow rate on the formation of the synthesized ZnO was studied at N_2 flow rate of 500 mL/min and synthesizing temperature of 800 ºC.

From SEM images as shown in Figure 4.43, morphology of the synthesized ZnO was also tetrapod nanostructure although the oxygen flow rate was increased from 100 to 150 mL/min. At oxygen flow rate of 100 mL/min, the diameter and length of pod deposited at zone 2 were about 30-40 nm and 800 nm, respectively as shown in Figure 4.43(a). The diameter and length of the pods deposited at zone 3 were in range of 50-60 nm and 160-180 nm, respectively as shown in Figure 4.43(b).

At oxygen flow rate of 150 mL/min, the diameter and length of pod deposited at zone 2 were about 50-60 nm and 310-370 nm, respectively as shown in Figure 4.43(c). The diameters and length of pod deposited at zone 3 were about 35-55 nm and 140-150 nm, respectively as shown in Figure 4.43(d).

From these results, it could be clearly observed that the oxygen flow rate only affected on the size of the ZnO deposited on the zone 2 and zone 3 of the quartz tube reactor. Based on the assumption of oxygen diffusion into Zn spherical particle shown in Figure 4.39, diffusion rate of oxygen at higher oxygen flow rate were faster. Therefore, nucleation process was relative high rate, leading to more generated nuclei. Under this condition, the lateral growth of the originally formed oxide particles is inhibited to a certain degree, resulting in small oxide size. On the other hand, the supply of oxygen to the surface of the Zn particle was highly limited under lower oxygen partial pressure since there was little oxygen in the atmosphere. Therefore, the surface reaction will be dominated by the continuing growth of the oxide particles already formed, leading to a relatively larger size (Gao et al., 2003).
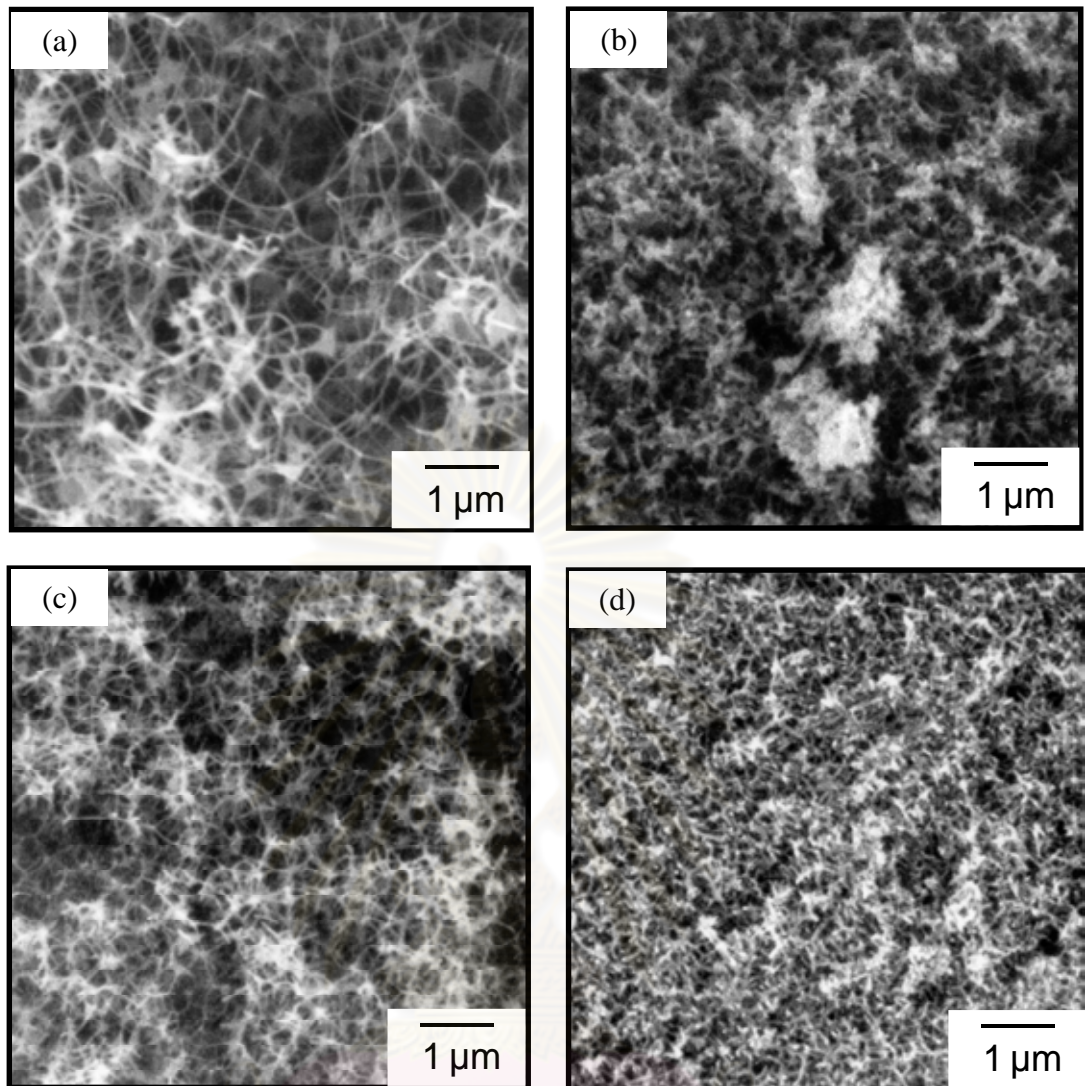
Figure 4.43 The synthesized ZnO deposited at zone 2 and zone 3 with different O_2 flow rates: (a) and (b) 100 mL/min, (c) and (d) 150 mL/min.

TEM image as shown in Figure 4.44 exhibited individual ZnO tetrapods which each pod was extended from the central part. Inset indicated selected area electron diffraction (SAED) which revealed a single-crystalline structure of the one leg of the synthesized ZnO.
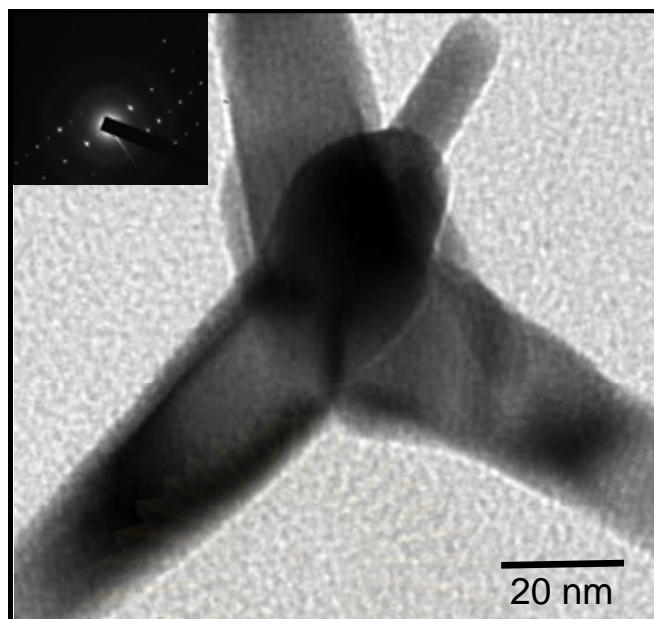
Figure 4.44 TEM image of the synthesized ZnO.
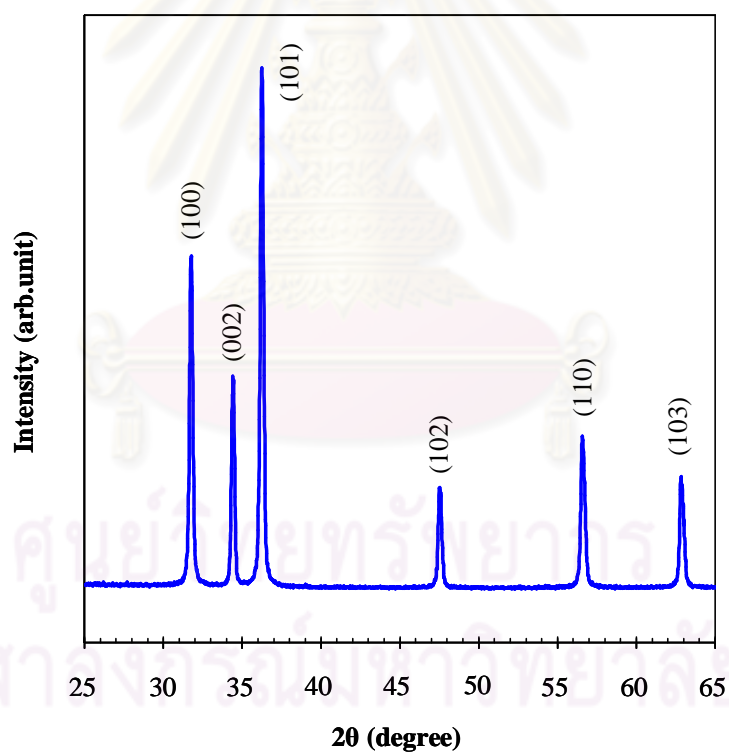
Figure 4.45 XRD pattern of the synthesized ZnO.

XRD pattern of the synthesized tetrapod ZnO was shown in Figure 4.45 which the diffraction peaks of the tetrapod ZnO were shape and narrow half width, while the peaks of other impurity phase were not found. The main peaks of the synthesized ZnO appeared at 31.8º, 34.3º and 36.2º that were typical diffraction peaks

from hexagonal ZnO planes of (100), (002) and (101), respectively. As indexed in Figure 4.42, all other peaks also matched the hexagonal ZnO structure with lattice constants of a = 3.250 Å and c = 5.207 Å. This indicated that the synthesized ZnO was composed of wurtzite structural ZnO.

4.3.4 Possible mechanisms

To explain the mechanisms for the formation of the synthesized tetrapod ZnO, the vapor-solid (VS) mechanisms was proposed which consisted of 2 stages: nucleation and growth stages.

Nucleation at the initial stage is a crucial role on the formation of the tetrapod ZnO (Xu and Sun, 2005). It was clearly seen that there was a knot in the center of the tetrapods as shown in Figure 4.44. The Zn vapor at high temperature diffused and immediately oxidized the environment of oxygen. The process of the initial nucleation was combination of diffusion, collision of atoms and reaction between the vapor molecules (including vapor Zn and O_2). When the supersaturation increase to a level at which nuclei formed, the produced ZnO nuclei grown to sizes larger than the critical size. The ZnO nuclei formed homogeneous as carried by the gas phase.

According to the octa-twin nucleus model (Takeuchi et al., 1994), ZnO nuclei formed in an environment of oxygen are octa-twin nuclei which consists of eight tetrahedral-shape crystals, each consists of three $\{11\bar{2}2\}$ pyramidal facets and one (0001) basal facet. The eight tetrahedral crystals are connected together by making the pyramidal faces contact one with another to form an octahedron. The surfaces of the octa-twin are all basal planes. An important additional condition is that every twin is of the inversion type including the polarities of the twinned crystals are not mirror-symmetric with respect to the contact plane but anti-symmetric. Therefore, the eight basal surfaces of the octa-twin are alternately the plus (0001) surface (+c) and the minus surface (-c), as shown in Figure 4.46.
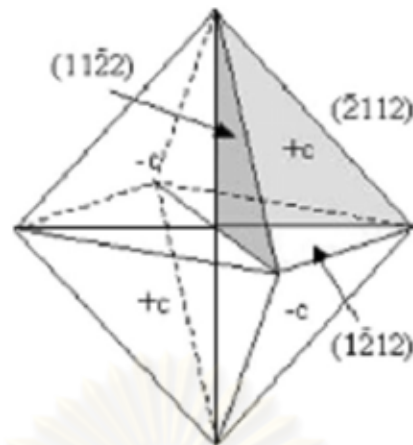
Figure 4.46 Octa-twin ZnO nuclei (Takeuchi et al., 1994)

The formation of the tetrapod structure has to do with the following two factors based on the octa-twin nucleus. It was known through the study of ZnO nanowires and nanobelts (Pan, Dai, and Wang, 2001), [0001] was the fastest growth direction in the formation of these structures. The octa-twin had 4 positive charged (0001) surfaces and 4 negative charged (0001) surfaces. The positive charged surfaces were likely to terminated with Zn, which might be favorable sites to attract vapor species, leading to the growth of whiskers along four [0001] directions.

4.4 Synthesis of the ZnO/MWCNT composites by single-step gas phase reaction

4.4.1 Investigation of thermodynamics

In this part, ZnO nanoparticles and carbon nanoparticles with iron nanoparticles inside were expected to be main compounds of the ZnO/MWCNT composites. The synthesis of the ZnO/MWCNT composites within a single-step process was more complexity than the isolated synthesis process of the ZnO nanoparticles and carbon nanoparticles. During the formation of the ZnO nanoparticles, introduced O_2 into the synthesis system was important for reacting with vaporized Zn under high synthesizing temperature. However, the introduced O_2 could possible react with the other elements including C and Fe which in form of encapsulated Fe in carbon nanoparticles. Oxidation of related elements within the synthesis system of the ZnO/MWCNT composites was carefully considered including oxidation of zinc, oxidation of carbon and oxidation of iron as shown in equation 4.22, 4.23(a)-(b), and 4.24(a)-(c), respectively.

Oxidation of zinc;

$$2Zn + O_2 = 2ZnO \tag{4.22}$$

Oxidation of carbon;

$$C + O_2 = CO_2 \tag{4.23a}$$

$$2C + O_2 = 2CO \tag{4.23b}$$

$$2CO + O_2 = 2CO_2 \tag{4.23c}$$

Oxidation of iron;

$$2Fe + O_2 = 2FeO \tag{4.24a}$$

$$\frac{3}{2}Fe + O_2 = \frac{1}{2}Fe_3O_4 \tag{4.24b}$$

$$4Fe_3O_4 + O_2 = 6Fe_2O_3 \qquad (4.24c)$$

Gibb free energy of reaction (ΔG) which is thermodynamic potential was considered for each oxidation. A negative value for ΔG indicates that a reaction can proceed spontaneously (Gaskell, 1981). Standard free energy change of oxidation ($\Delta G°$) of related elements at different synthesizing temperatures was revealed from Ellingham diagram as shown in Figure 4.47.
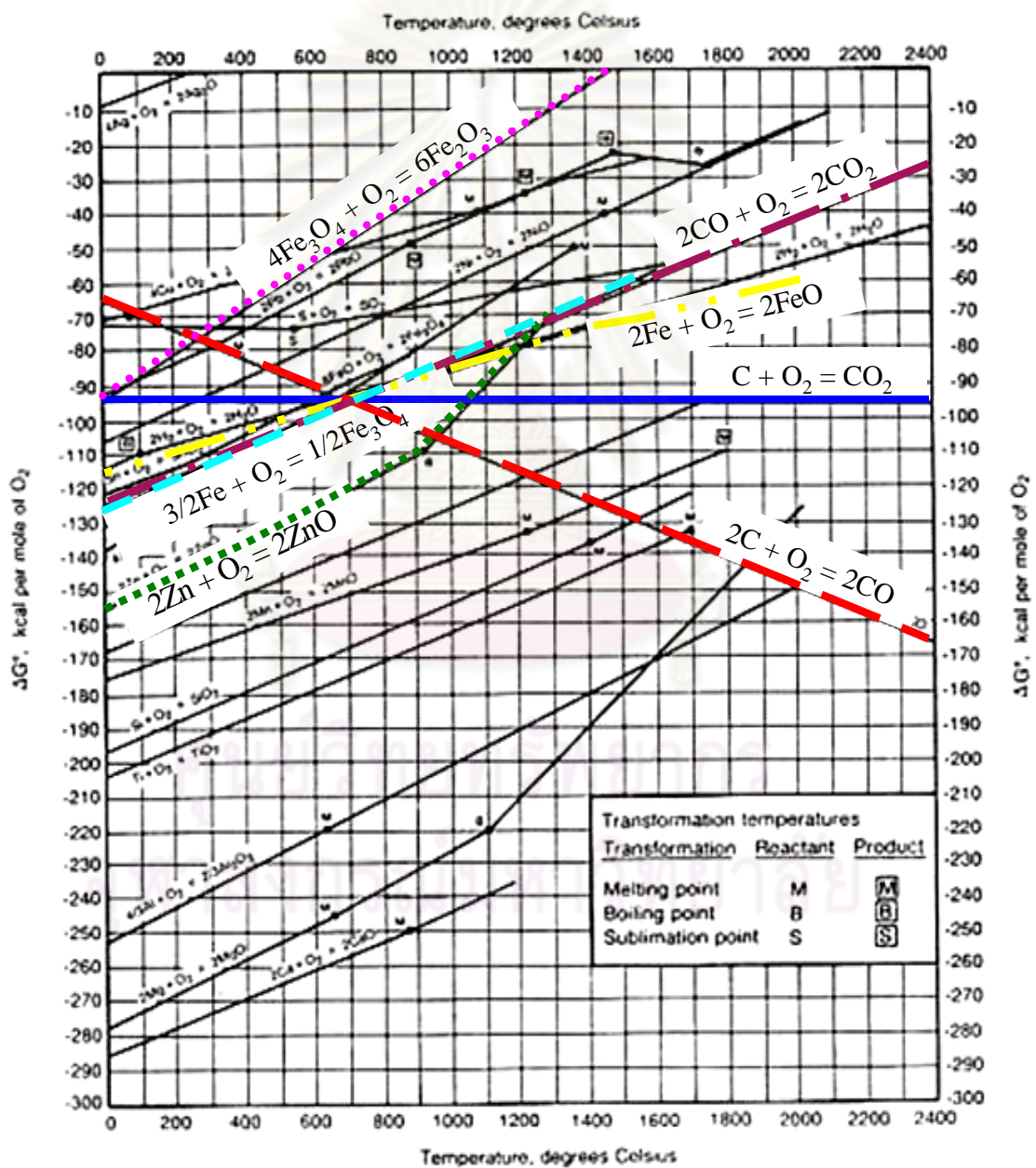
Figure 4.47 Ellingham diagram for oxides of Zn, C and Fe.

(http://www.nss.org/settlement/nasa/spaceresvol3/images/pmofld-fig33.jpg)

From Figure 4.47, it could be clearly seen negative value of ΔG° of the oxidation of Zn, C and Fe over wide ranges of the synthesizing temperature. At any synthesizing temperature, highly negative value of ΔG° shows more spontaneous reaction. Therefore, at the same synthesizing temperature, the oxidation of Zn, C and Fe could simultaneously take place within this system with different abilities. Decreasing of the synthesizing temperature commonly exhibit the highly negative value of ΔG° of oxidation. However, oxidation of CO as shown in equation 4.23b shows highly negative value of ΔG° at higher synthesizing temperature. While, complete oxidation of C as shown in equation 4.23a reveals constant negative value of ΔG° although the temperature is increased.

ΔG° of the oxidation of Zn, C and Fe at the synthesizing temperatures of 800 and 900 °C was shown in Table 4.1. It could be clearly observed that, at the synthesizing temperatures of 800 and 900 °C, the negative value of ΔG° of the Zn oxidation was the highest, leading to the oxidation of Zn could take place easily compared to the oxidation of the other elements.

Table 4.1 Standard free energy change of oxidation of Zn, C and Fe at different synthesizing temperatures

Reaction	ΔG° (kcal/mol of O_2)	
	T = 800 °C	T = 900 °C
$2Zn + O_2 = 2ZnO$	-115	-110
$C + O_2 = CO_2$	-93	-93
$2C + O_2 = 2CO$	-96	-102
$2CO + O_2 = 2CO_2$	-92	-88
$2Fe + O_2 = 2FeO$	-92	-89
$3/2Fe + O_2 = 1/2Fe_3O_4$	-92	-88
$4Fe_3O_4 + O_2 = 6Fe_2O_3$	-42	-35

The major oxidation of carbon nanoparticles could be considered into 2 reactions including complete and incomplete oxidation of carbon nanoparticles, while oxidation of CO which is sequentially reaction of the incomplete oxidation was considered as minor oxidation. At the synthesizing temperature of 800 and 900 °C, the negative value of ΔG° of the complete oxidation was the same of 93 kcal/mol. While,

the negative value of ΔGº of the incomplete oxidation was higher at higher synthesizing temperature. Therefore, decrease in oxidation of carbon could be taken place by decrease in the synthesizing temperature. Because of iron nanoparticles encapsulated in the carbon nanoparticles, the oxidation of the iron nanoparticles was also taken place unavoidable after partial oxidation of the carbon nanoparticles. The oxidation of the iron nanoparticles could be initiated by 2 major oxidations as shown in equation 4.24a and 4.24b, respectively.

4.4.2 Effect of synthesizing temperature

From clues of the thermodynamic data, it could be clearly realized that, among various parameters of the synthesizing temperature, nitrogen flow rate, oxygen flow rate and glycerol to ferrocene molar ratio, the synthesizing temperature was the major parameter of this study. Therefore, in this part, the effect of synthesizing temperature on the formation of the synthesized ZnO/MWCNT composites was studied under the same condition of nitrogen flow rate and oxygen flow rate of 500 and 100 mL/min, respectively and glycerol to ferrocene molar ratio of 5 to 1. From preliminary study, it should be noted that color of products deposited at zone 3 was found to be gray color which was the combination of black color of the synthesized MWCNTs and white color of the synthesized ZnO nanoparticles. The gray color could be implied that the synthesized products might be the ZnO/MWCNT composites. Therefore, the synthesized products at zone 3 were kept and characterized and then reported and discussed in this part.

Synthesizing temperature of 800 ºC

Morphology of the synthesized products at the synthesizing temperature of 800 ºC was shown in Figure 4.48.

Figure 4.48 SEM images of the synthesized products at the synthesizing temperature of 800 ºC.

The typical SEM images as shown in Figure 4.48(a) revealed the MWCNT bundles coated with ZnO nanoparticles. The synthesized MWCNTs exhibit relatively uniform diameter and length with a high aspect ratio. Figure 4.48(b) exhibited a highly magnified SEM image of the composites of which the estimated diameter is 60–70 nm. The coated layer on the surface of the MWCNTs consisted of a large number of much smaller ZnO nanoparticles.

Referring to the synthesized MWCNTs within the isolated synthesis of the MWCNTs (see page 62) under the same condition of the nitrogen flow rate of 500 mL/min, the synthesizing temperature of 800 ºC and glycerol to ferrocene molar ratio of 5/1, the synthesized carbon nanoparticles at zone 3 were the MWCNTs with tube diameter about 50 nm. It could be clearly observed that the synthesized MWCNTs within the composite synthesis system were similarity of the tube diameter ranges.

Under the same condition of the nitrogen flow rate of 500 mL/min, the oxygen flow rate of 100 mL/min and the synthesizing temperature of 800 ºC, the synthesized ZnO nanoparticles at zone 3 of the isolated synthesis system of the ZnO nanoparticles (see page 87) were tetrapod structure which their pod diameter and length were about 50-60 nm and 160-180 nm, respectively. It could be clearly observed that morphology of the synthesized ZnO nanoparticles of the composite synthesis system were significantly changed from the tetrapod structure of the isolated synthesis system into spherical structure with diameter in range of 20-30 nm.

XRD pattern of the synthesized products at the synthesizing temperature of 800 ºC shown in Figure 4.49 consisted of a peak from (002) planes of hexagonal graphite structure at $2\theta = 27º$ and main peaks from (100), (002), (101), (102) and (110) planes at $2\theta = 31.8º$, $34.3º$, $36.2º$, $47.5º$ and $57.6º$, respectively which corresponded to typical diffraction peaks from hexagonal ZnO with lattice constants of a = 3.250 Å and c = 5.207 Å. This indicated that the synthesized ZnO was composed of wurtzite structural ZnO. It could be clearly observed that the diffraction peaks were combination of the peak of the MWCNTs as shown in Figure 4.33 and the ZnO nanoparticles as shown in Figure 4.45. Furthermore, response of α-Fe$_2$O$_3$ was also found at $2\theta = 54.3º$. Any response of (111) plane of the face-centered cubic (fcc) γ-Fe at $2\theta = 43.7$ ° and (110) plane of body-centered cubic (bcc) α-Fe at $2\theta = 44.7º$ was found in the composites. Furthermore, any orthorhombic cementite Fe$_3$C phase was also found in the XRD pattern. Referring to the XRD pattern of the synthesized MWCNTs as shown in Figure 4.33, it could be clearly observed that crystal phase of the Fe nanoparticles were the combination of γ-Fe, α-Fe and Fe$_3$C phases while the crystal phase of the Fe nanoparticles of the synthesized products within the ZnO/MWCNT composite synthesis system was α-Fe$_2$O$_3$ phase. Therefore, it could be realized that the Fe nanoparticles in γ-Fe, α-Fe and Fe$_3$C phases of the synthesized products within the ZnO/MWCNT composite synthesis system was oxidized into the iron form.
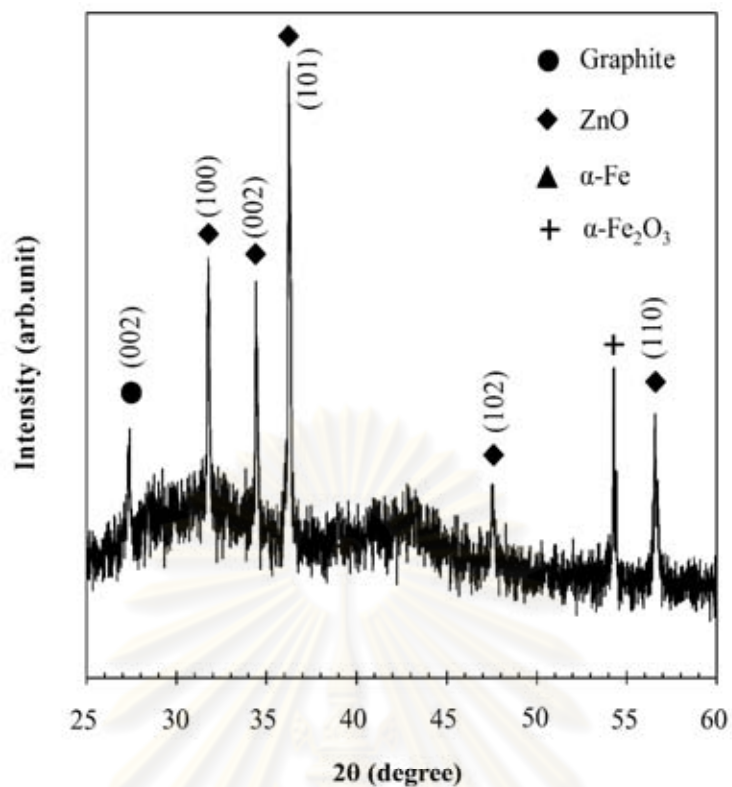
Figure 4.49 XRD pattern the synthesized products at the synthesizing temperature of 800 ℃.

Synthesizing temperature of 900 ℃

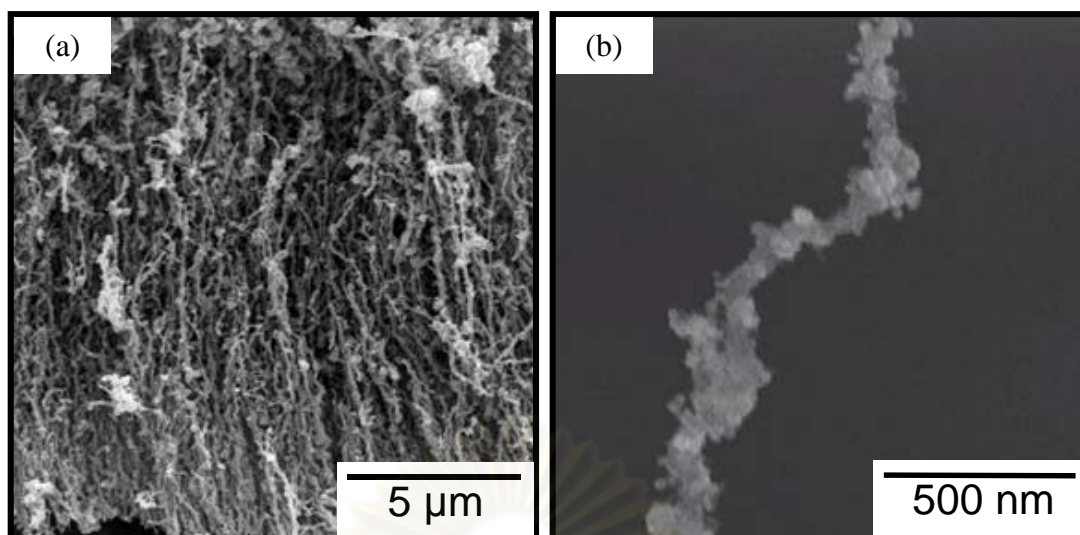Morphology of the synthesized products at the synthesizing temperature of 900 ℃ was shown in Figure 4.50. The typical SEM image and its highly magnified SEM image as shown in Figure 4.50(a) and (b), respectively, clearly exhibited agglomerated particles with primary diameters about 100-200 nm, while any of MWCNTs was observed.
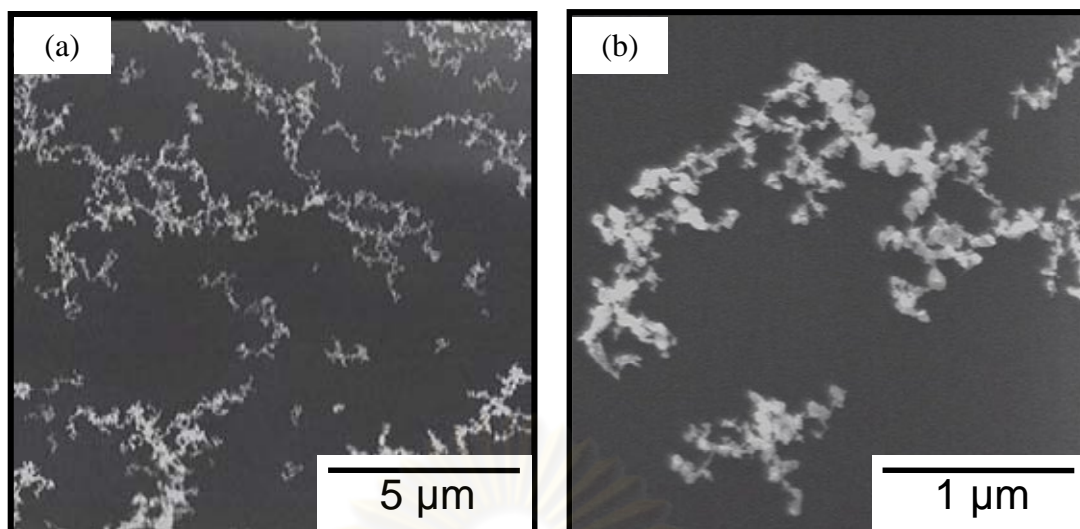
Figure 4.50 SEM images of the synthesized products at the synthesizing temperature of 900 ºC.

The XRD pattern of the synthesized products at the synthesizing temperature of 900 ºC was shown in Figure 4.51. It exhibited (100), (002), (101), (102) and (110) planes of the synthesized ZnO at $2\theta = 31.8°$, $34.4°$, $36.2°$, $47.4°$ and $57.6°$, respectively which corresponded to typical diffraction peaks from hexagonal ZnO with lattice constants of a = 3.250 Å and c = 5.207 Å. This indicated that the synthesized ZnO was composed of wurtzite structural ZnO. However, it could be also observed responses of pure Zn at $2\theta = 39.3°$ and $43.1°$ which could recognize non-oxidation of the vaporized Zn. Furthermore, response of α-Fe_2O_3 was revealed at $2\theta = 54.3°$, while pure Fe were also exhibited at $2\theta = 54.3°$. However, any response of C could be found which could indicate that most of carbon nanoparticles reacted with the introduced O_2.
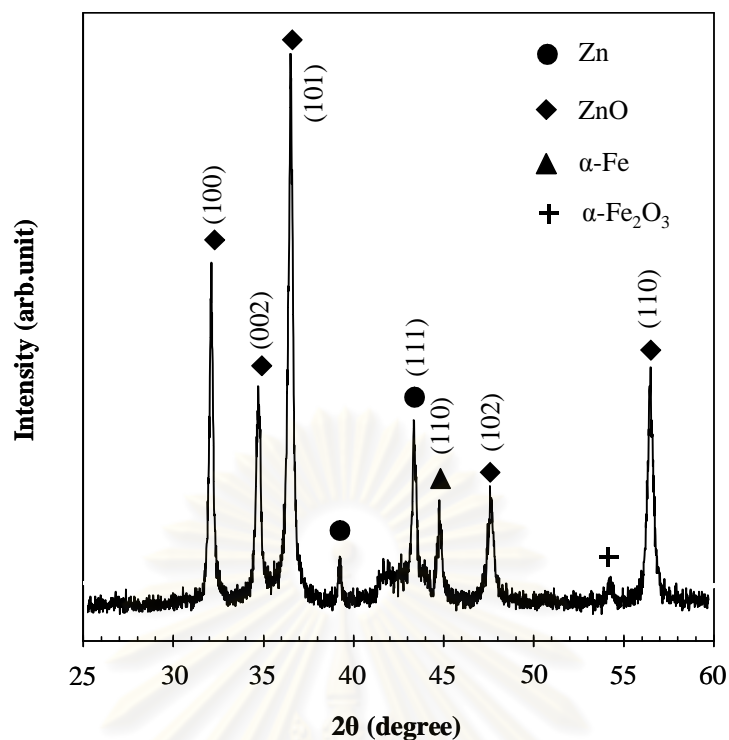
Figure 4.51 XRD pattern the synthesized products at the synthesizing temperature of 900 ℃.

The experimental results exhibited that the synthesizing temperature affected on the formation of the ZnO/MWCNT composites. From the XRD patterns, both of the synthesizing temperatures, the ZnO nanoparticles were formed. However, it could be clearly seen that at the synthesizing temperature of 900 ℃, extra response of Zn was observed. Referring to the isolated synthesis of the ZnO nanoparticles at the same condition of the N_2 flow rate, synthesizing temperature and O_2 flow rate of 500 mL/min, 900 ℃ and 100 mL/min, respectively, as reported and discussed above (see page 91), this could identify that within the composite synthesis system, amount of O_2 for reacting with Zn was lower due to competitive oxidation of C and Fe atoms as shown in Figure 4.47, leading to the amount of O_2 was not enough for the oxidation of Zn and then remains of Zn were observed.

The XRD patterns also revealed the response of C from the MWCNTs within the synthesized composites at the synthesizing temperature of 800 ℃. However, the response of C was disappeared when the synthesizing temperature was increased to 900 ℃. The disappeared C peak exhibited that at the synthesizing temperature of 900 ℃, all MWCNTs were oxidized. Referring to Ellingham diagram as shown in Figure 4.47, the incomplete oxidation of C at higher temperature is found

to be more spontaneous due to its highly negative value of ΔG°. Therefore, at the synthesizing temperature of 900 ℃, the synthesized MWCNTs could be oxidized easier than those of 800 ℃. Furthermore, it could be implied that the synthesizing temperature of 900 ℃ was too high for the formation of the ZnO/MWCNT composites. Previous work (Misra et al., 2006) revealed the burning property of the MWCNTs by using Thermal Gravimatric Analysis (TGA). There could be found that the MWCNTs were initially oxidized around 400 ℃ and completely oxidized at 900 ℃, suggesting that at this temperature amorphous carbon was well as MWCNTs converted to gaseous form. Therefore, in this work, the disappearance of the synthesized MWCNTs within the composite synthesis system was caused by complete oxidation of the MWCNTs. After the complete oxidation of the MWCNTs at the synthesizing temperature of 900 °, the Fe nanoparticles inside the MWCNTs were exposed by surrounding O_2, leading to the formation of the iron oxide in form of α-Fe_2O_3 (Wu et al., 2009) simultaneous with the formation of the ZnO nanoparticles.

Although the XRD pattern of the synthesized composites at the synthesizing temperature of 800 ℃ exhibited the response of C from the MWCNTs, the compete oxidations of C and Fe unavoidably took place and simultaneously with the oxidation of Zn as shown in Figure 4.47. This could be assured by response of Fe_2O_3 which was from the oxidation of Fe. Therefore, these experimental results could inform that some of the MWCNTs were oxidized resulted in the Fe nanoparticles inside the MWCNTs were exposed to surrounding O_2 and then were simultaneous oxidized to form the iron oxide. Referring to TGA analysis as discussed above, it was well known that the MWCNTs were initially and completely oxidized around 400 and 900 ℃, respectively. Therefore, at the synthesizing temperature of 800 ℃, partial oxidation of the synthesized MWCNTs was occurred, leading to the appearance of the Fe_2O_3 of this work.

ZnO/MWCNT composite yield at the synthesizing temperature of 800 ℃ can be defined in equation 4.25.

$$ZnO/MWCNT \text{ composite yield } (\%) = \frac{W_{ZnO/MWCNT}}{W_{glycerol} + W_{ferrocene} + W_{Zn}} \times 100 \quad (4.25)$$

Where $W_{ZnO/MWCNT}$ = Weight of synthesized ZnO/MWCNT composites

$W_{glycerol}$	= Weight of glycerol
$W_{ferrocene}$	= Weight of ferrocene
W_{Zn}	= Weight of zinc

Yield of the ZnO/MWCNT composite which were synthesized at the synthesizing temperature of 800 ºC were 1.46 %.

TEM analysis of the synthesized ZnO/MWCNT composites at the synthesizing temperature of 800 ºC in Figure 4.52 revealed that the ZnO nanoparticles were well attached to the MWCNT surface. The narrow size distribution of the ZnO nanoparticles with an average particle size of 20–30 nm could be obtained. This was ascribed to the growth of the ZnO nanoparticles on the outer surface of MWCNTs after the oxidation of zinc vapor which took place after the formation of the MWCNTs (Beker et al., 2002)
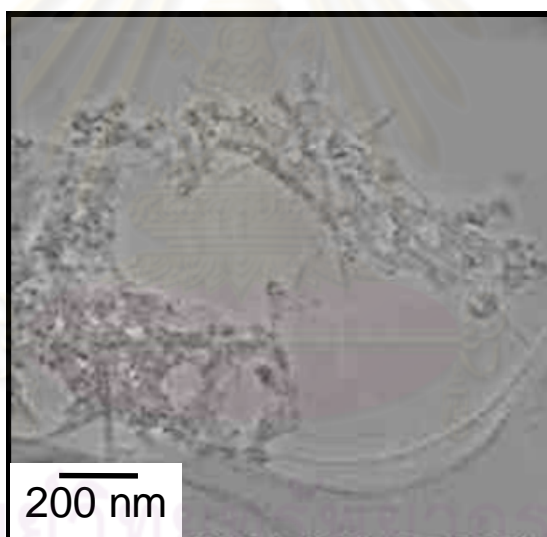
Figure 4.52 TEM image of the synthesized ZnO/MWCNT composites at the synthesizing temperature of 800 ºC.

FT-IR spectrum of the synthesized MWCNT/ZnO composites at the synthesizing temperature of 800 ºC was shown in Figure 4.53 which revealed surface chemistry of the MWCNT/ZnO composite. In the high frequency region, band around 3420 cm^{-1} could be assigned to the bending vibrations of adsorbed molecular water and stretching vibrations of OH groups. The peaks around 1600 cm^{-1} could be inferred as CO_2 stretching vibration. Furthermore, in the low frequency region, peak

around 500 cm^{-1} in ZnO/MWCNT composite was assigned to the Zn–O. From the FT-IR spectrum, it could be assured that the synthesized products at the synthesizing temperature of 800 ℃ were the ZnO/MWCNT composites.
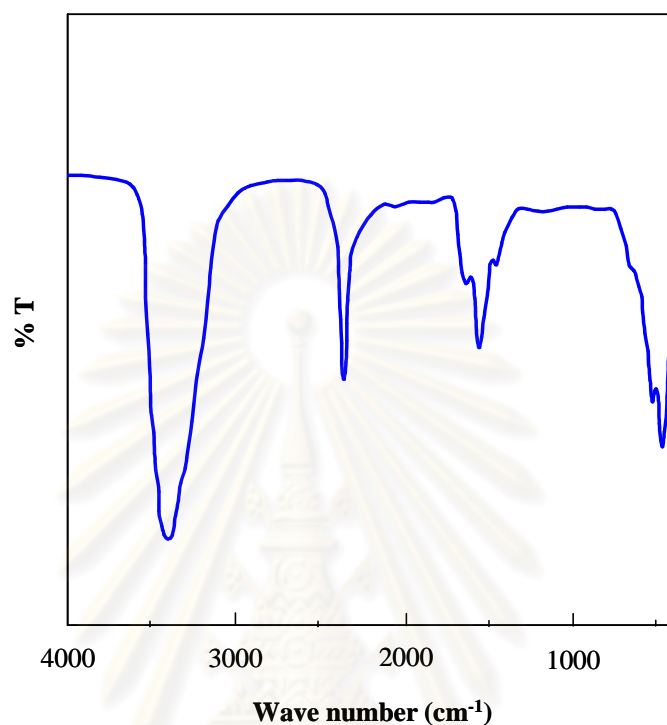
Figure 4.53 FT-IR spectrum of the synthesized ZnO/MWCNT composites at the synthesizing temperature of 800 ℃.

Furthermore, elemental composition of the synthesized products at the synthesizing temperature of 800 ℃ was also affirmed by EDX as shown in Figure 4.54. The presence of Zn, O, Fe and C peaks could reveal the existence of the ZnO nanoparticles on the surface of MWCNTs containing Fe nanoparticles inside (Chen et al., 2005). The Cu signal originated from the copper microgrid employed for the microscopic analysis. The elemental composition of the C, O and Zn atoms within the ZnO/MWCNT composite as shown in inset was 18.27, 41.66 and 40.07 %, respectively. It could be clearly observed that atomic ratio of the Zn to O was 1.04 which could identify that all of the vaporized Zn could react with the introduced O$_2$ to form the ZnO nanoparticles.
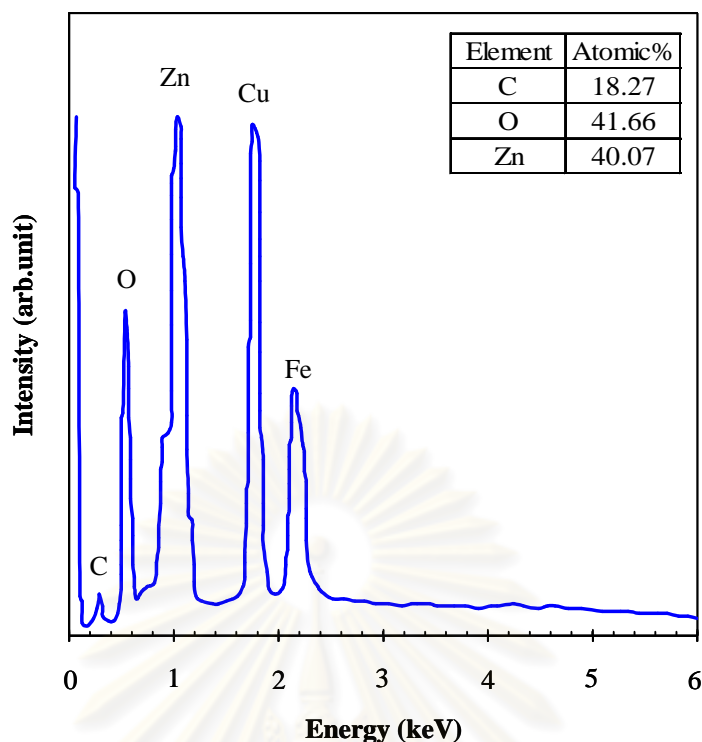
Figure 4.54 EDX pattern of the synthesized ZnO/MWCNT composites at the synthesizing temperature of 800 °C.

For comparison, the UV–vis absorbance of the synthesized MWCNTs, the synthesized ZnO and the synthesized ZnO/MWCNT composites dispersed in deionized water were depicted in Figure 4.55. In curve (a), a broad absorption peak at 262 nm was originated from the C=C structure of the synthesized MWCNTs (Chen et al, 2002). Meanwhile, the absorption peak at 368 nm in curve (b) would represent dispersion of the synthesized ZnO nanoparticles in deionized water. The absorption peak of the synthesized ZnO/MWCNT composites was dominated by the characteristic absorption of ZnO, which was observed at about 363 nm in curve (c). As light blue shift of the absorption band of the composites regarding to that of pure ZnO nanoparticles would be attributed to the quantum size effect of the synthesized ZnO nanoparticles.
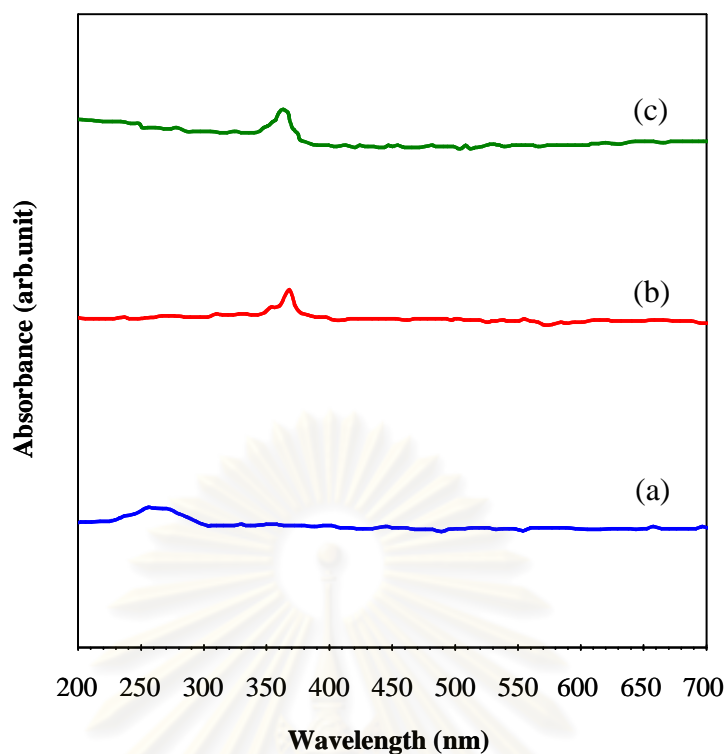
Figure 4.55 UV–visible absorbance of the samples in distillation water: (a) the synthesized MWCNTs, (b) the synthesized ZnO and (c) the synthesized ZnO/MWCNT composites.

4.4.3 Possible Mechanisms

Based on experimental results, it could be ascribed to the formation of the ZnO nanoparticles on the outer surface of MWCNTs after the oxidation of zinc vapor which took place after the formation of MWCNTs as shown in Figure 4.56.

The possible mechanisms, proposed here, were believed that, at the synthesizing temperature of 800 ºC, the MWCNTs which were synthesized firstly were surrounded by Zn vapor and O_2. Zn vapor was then oxidized by O_2 to form ZnO nanoparticles, while most of the MWCNTs were not oxidized, leading to appearance of the MWCNTs surrounded with ZnO nanoparticles. Finally, attachment of the ZnO nanoparticles on the outer surface of the MWCNTs was occured. The formation of the composites of ZnO nanoparticles and MWCNTs were formed.

At the synthesizing temperature of 900 ºC, the possible mechanisms were proposed that the synthesized MWCNTs which were surrounded by Zn vapor and O_2 were oxidized by O_2 simultaneously with the oxidation of Zn vapor, leading to

complete disappearance of the MWCNTs. Iron catalytic nanoparticles inside the MWCNTs were then exposed to surrounding O_2 and oxidized to form α-Fe_2O_3 nanoparticles. Because of competition of the oxidation of Zn nanoparticles, MWCNTs and Fe nanoparticles, the introduced O_2 were not enough for remaining Zn. Therefore, some of Zn vapor were not used for the formation of ZnO nanoparticles. Finally, the ZnO nanoparticles, Zn nanoparticles and Fe_2O_3 nanoparticle were agglomerated each other to form agglomerated nanoparticles.
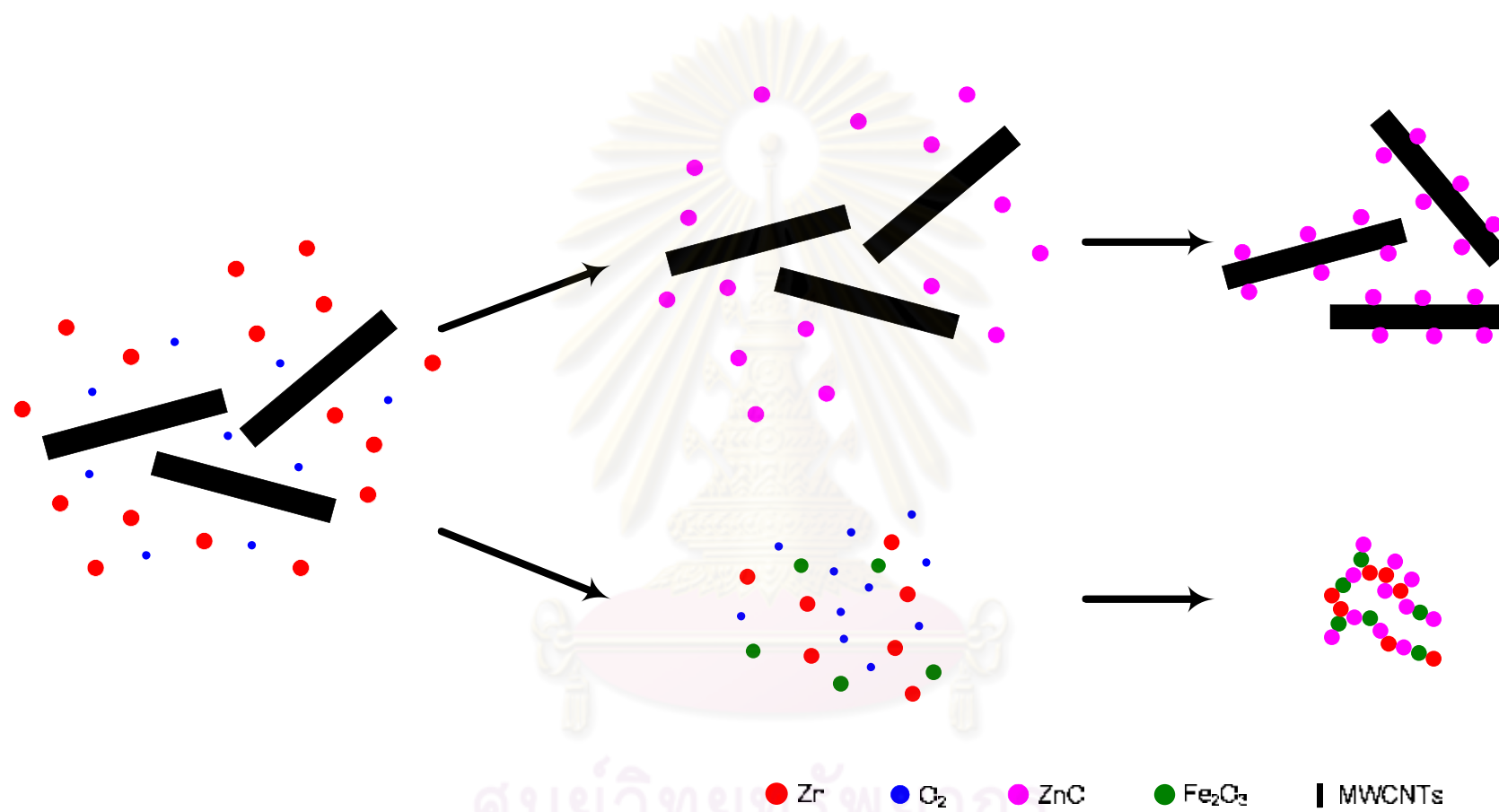
Figure 4.56 Possible mechanisms of the ZnO/MWCNT composites.

CHAPTER V

CONCLUSION AND RECOMMENDATION

In this work, the ZnO/MWCNT composites were synthesized by the single-step gas phase reaction. Glycerol and ferrocene were used as sources of carbon and iron catalyst, while pure zinc powder was used as zinc source. It was found that the synthesis of the composites by the combination of the formation of ZnO nanoparticles and carbon nanoparticles was more complicated than the isolated synthesis of the ZnO nanoparticles or the isolated of the carbon nanoparticles. Therefore, the isolated synthesis of ZnO nanoparticles and carbon nanoparticles was separately studied. The MWCNTs with high purity were synthesized by CVD of glycerol and ferrocene. Meanwhile, to understand the formation of MWCNTs, parallel study on synthesis of SWCNTs by pulsed Nd:YAG laser ablation was also investigated. ZnO nanoparticles were synthesized by oxidation of pure Zn in a tubular quartz reactor. Finally, the ZnO/MWCNT composites were then investigated under designated conditions by single-step gas phase reaction.

5.1 Analysis of the SWCNT synthesis by laser ablation

In this part, the airborne SWCNTs were synthesized by pulsed laser ablation of C/Ni/Co rod under atmospheric pressure. The effects of Nd:YAG pulsed laser intensity and temperature on the morphology, purity and crystallinity and size distributions of the synthesized products were studied. An increase in the laser intensity resulted in an increase in the number concentration of synthesized carbon nanoparticles in aerosol. The experimental results exhibited that the formation of the SWCNTs would be negligible at temperature lower than 1000 ℃ although the laser intensity was increased. However, the airborne SWCNTs with high purity and crystallinity were synthesized at the temperatures of 1000 and 1080 ℃. Therefore, the temperature was found to be the main parameter for the SWCNT formation.

5.2 Analysis of the carbon nanoparticle synthesis by CVD of glycerol and ferrocene

The MWCNTs were synthesized by CVD of glycerol and ferrocene under a condition of atmospheric pressure. The effects of the nitrogen flow rate, synthesizing temperature, glycerol to ferrocene molar ratio and deposited position on the morphology, purity and crystallinity and yield of the synthesized carbon nanoparticles were investigated. When the nitrogen flow rate was increased, the MWCNTs with smaller tube diameters and higher purity were synthesized. However, the increasing of the nitrogen flow rate revealed the decreasing of the yield. When the synthesizing temperature was increased, the MWCNTs with larger tube diameters and lower purity were synthesized. Furthermore, an increase in synthesizing temperature could lead to the increasing yields. The glycerol to ferrocene molar ratio could also exert significant effect on the MWCNTs. The higher molar ratio resulted in the synthesized MWCNTs with larger diameters and lower purity, while the yield was found to be decreased.

5.3 Analysis of the ZnO synthesis by oxidation of Zn

The ZnO nanoparticles were synthesized by the oxidation of pure Zn particles by a French process. The effects of the nitrogen flow rate, synthesizing temperature, oxygen flow rate and deposited position on the morphology, size and yield of the synthesized ZnO nanoparticles were investigated. When nitrogen flow rate was increased from 200 to 350 and 500 mL/min, the morphologies of the synthesized ZnO nanoparticles were changed from combination of rod-like structure, and tetrapod nanostructure to combination of rod-like structure, micro-sheets and tetrapods and only tetrapods, respectively. The increased nitrogen flow rate could lead to a significant decrease in diameter and length of the synthesized ZnO nanoparticles with tetrapod characteristics. When the synthesizing temperature was increased, the morphologies of the synthesized ZnO nanoparticles were change from tetrapods only to combination of the rod-like structure, micro-sheets and tetrapods. Increase in the synthesizing temperature would also result in a significant increase in diameter and length of the synthesized ZnO. When the oxygen flow rate was increased, the

majority of the synthesized ZnO nanoparticle morphology was tetrapod. However, the diameter and length of the pod were found to be decreased significantly with the higher oxygen flow rate.

5.4 Analysis of the ZnO/MWCNT composites

Finally, the ZnO/MWCNT composites were synthesized by a single-step gas phase reaction. The theoretical study of thermodynamics exhibited unavoidable oxidation of C and Fe simultaneous with the oxidation of Zn over wide ranges of the synthesizing conditions. The synthesizing temperature was found to be a major parameter in this work. At the synthesizing temperature of 800 ℃, the synthesized products were the composites of the ZnO nanoparticles and MWCNTs. Iron oxide in form of α-Fe_2O_3 was found to exist in the synthesized composites. These experimental results revealed that some of the MWCNTs were oxidized, leading to the formation of Fe_2O_3 because the Fe catalytic nanoparticles inside were exposed to surrounding O_2. However, at the synthesizing temperature of 900 ℃, the MWCNTs were disappeared, while some remains of Zn were clearly observed. It could be implied that the synthesizing temperature of 900 ℃ was excessively high for the formation of the ZnO/MWCNT composites. Therefore, in this work, the composites were synthesized under the optimal condition of the nitrogen flow rate, oxygen flow rate and synthesizing temperature of 500 mL/min, 100 mL/min and 800 ℃, respectively.

5.5 Recommendation for future work

In a single-step synthesis process of the ZnO/MWCNT composites by gas phase reaction, O_2 which is strong oxidizer are significantly introduced into the system at high temperature for the formation of the ZnO nanoparticles. However, the oxidations of carbon unavoidably simultaneous occur at any high temperature. Furthermore, Fe as catalyst for the formation of the carbon nanoparticles of this work was also oxidized. Therefore, the introduced O_2 might be too strong oxidizer for this system. To decrease in the oxidation of undesired products, therefore, weaker oxidizer such as water vapor is considerable recommended for next study.

REFERENCES

Andrews, R., et al. Continuous production of aligned carbon nanotubes: a step closer to commercial realization. Chemical Physics Letters 303 (1999): 467-474.

Antisari, M.V., Marazzi, R., and Krsmanovic, R. Synthesis of multiwall carbon nanotubes by electric arc discharge in liquid environments. Carbon 41 (2003): 2393–2401.

Baker, S., Cai, W., Lasseter, T., Weidkamp, K., and Hamers, R. Covalently bonded adducts of deoxyribonucleic acid (DNA) oligonucleotides with single-wall carbon nanotubes: synthesis and hybridization. Nano Letters 2 (2002): 1413-1417.

Baker, S., Cai, W., Lasseter, T., Weidkamp, K., and Hamers, R. Covalently bonded adducts of deoxyribonucleic acid (DNA) oligonucleotides with single-wall carbon nanotubes: synthesis and hybridization. Nano Letters 2 (2002) 1413-1417

Battez, A.H., et al. CuO, ZrO_2 and ZnO nanoparticles as antiwear additive in oil lubricants. Wear 265 (2008): 422-428.

Baughman, R.H., Zakhidov, A.A., and Hee, W.A. Carbon nanotubes-the route toward applications. Science 297 (2002): 787-792.

Berber, S., Kwon, Y.K., and Tomànek, D. Unusually high thermal conductivity of carbon nanotubes. Physical Review Letters 84 (2000): 4613-4616.

Chaisitsak, S., Nukeaw, J., and Tuantranont, A. Parametric study of atmospheric-pressure single-walled carbon nanotubes growth by ferrocene-ethanol mist CVD. Diamond & Related Materials 16 (2007): 1958-1966.

Chang, P., et al. ZnO nanowires synthesized by vapor trapping CVD Method. Chemistry of Materials 16 (2004): 5133-5137.

Charinpanitkul, T., et al. Naphthalene as an alternative carbon source for pyrolytic synthesis of carbon nanostructures. Journal of Analytical and Applied Pyrolysis 86 (2009): 386-390.

Chen, C.S., Chen, X.H., Xu, L.S., Yang, Z., and Li, W.H. Modification of multi-walled carbon nanotubes with fatty acid and their tribological properties as lubricant additive. Carbon 43 (2005): 1660-1666.

Chen, C.S., et al. Zinc oxide nanoparticle decorated multi-walled carbon nanotubes and their optical properties. Acta Materialia 54 (2006): 5401-5407.

Chen, X.H., et al. Non-destructive purification of multi-walled carbon nanotubes produced by catalyzed CVD. Materials Letters 57 (2002): 734-738.

Cheng, J., et al. Synthesis of iron-filled carbon nanotubes with a great excess of ferrocene and their magnetic properties. Solid State Communications 149 (2009): 1619-1622.

Chrissanthopoulos, A., et al. Novel ZnO nanostructures grown on carbon nanotubes by thermal evaporation. Thin Solid Films 515 (2007): 8524-8528.

Collins, P.G., and Avouris, P. Nanotubes for electronics. Scientific American Magazine 283 (2000): 62–9.

Cunningham, E. On the velocity of steady fall of spherical particles through fluid medium. Proceeding of the Royal Society of London A 83: 357-365.

Dai, Y., Zhang, Y., Li, Q.K., and Nan, C.W. Synthesis and optical properties of tetrapod-like zinc oxide nanorods. Chemical Physics Letters 358 (2002): 83–86.

Delalu, H., Vignalou, J.R., Elkhatib, M., and Metz, R. Kinetics and modeling of diffusion phenomena occurring during the complete oxidation of zinc powder: influence of granulometry, temperature and relative humidity of the oxidizing fluid. Solid State Sciences 2 (2000): 229-235.

Dresselhaus, M., Dresselhaus, G., and Saito, R. Physics of carbon nanotubes. Carbon 33 (1995): 883–91.

Du, Y., Hao, C.C., and Wang, G. Preparation of floral-patterned ZnO/MWCNT heterogeneity structure using microwave irradiation heating method. Materials Letters 62 (2008): 30-32.

Dupuis, A.C. The catalyst in the CCVD of carbon nanotubes-a review. Progress Materials Science 50 (2005): 929-961.

Endo, M., et al. Structural characterization of carbon nanofibers obtained by hydrocarbon pyrolysis. Carbon 39 (2001): 2003-2010.

Fu, L., et al. Coating carbon nanotubes with rare earth oxide multiwalled nanotubes. Advance Materials 16 (2004): 350-352.

Futaba, D.N., et al. Kinetics of water-assisted single-walled carbon nanotube synthesis revealed by a time-evolution analysis. Physical Review Letters 95 (2005): 056104.

Ganter, M.J., et al. Variation of single wall carbon nanotube dispersion properties with alkyl amide and halogenated aromatic solvents. Materials Chemistry and Physics 116 (2009): 235–241.

Gao, W., Li, Z.W., Harikisun, R., and Change, S.S. Zinc oxide films formed by oxidation of zinc under low partial pressure of oxygen. Materials Letters 57 (2003): 1435-1440.

Gaskell, D.R. Introduction to metallurgical thermodynamics. Hemisphere Publishing Corporation. 2nd edition, 1981

Gorbunov, A., Jost, O., pompe, W., and Graff, A. Solid-liquid-solid mechanism of single-wall carbon nanotubes. Carbon 40 (2002): 113-118.

Huang, C.S., et al. Field emission properties of CNT-ZnO composite materials. Diamond and Related Materials 18 (2009): 452-456.

Huang, L., Lau, S.P., Yang, H.Y., Leong, E.S.P., and Yu, S.F. Stable superhydrophobic surface via carbon nanotubes coated with a ZnO thin film. Journal of Physical Chemistry B 109 (2005): 7746-7748.

Iijima, S. Helical microtubules of graphitic carbon. Nature 354 (1991): 56–58.

Intra, P., and Tippayawong, N. An overview of differential mobility analyzers for size classification of nanometer-sized aerosol particles. Songklanakarin Journal of Science and Technology 30 (2008): 243-256.

Jiang, K., Eitan, A., Schadler, L.S., Ajayan, P.M., and Siegel, R.W. Selective attachment of gold nanoparticles to nitrogen-doped carbon nanotubes. Nano Letters 3 (2003): 275-277.

Jiang, L., and Gao, L. Fabrication and characterization of ZnO-coated multi-walled carbon nanotubes with enhanced photocatalytic activity. Materials Chemistry and Physics 91 (2005): 313-316.

Jorio, A., et al. Structural (n,m) determination of isolated single-wall carbon nanotubes by resonant Raman scattering. Physical Review Letters 86 (2001): 1118–1121.

Kataura, H., et al. Diameter control of single-walled carbon nanotubes. Carbon 38 (2000): 1691–1697.

Kaw, A.K. Mechanics of composite materials. CRC. 2nd edition, 2006.

Kim, S.H., and Zachariah, M.R. Gas-phase growth of diameter-controlled carbon nanotubes. Materials Letters 61 (2007): 2079–2083.

Kim, S.H., and Zachariah, M.R. In-flight measurements of the aerosol growth of carbon nanotubes by electrical mobility classification. Journal of Physical Chemistry B 110 (2006): 4555–4562.

Knutson, E.O., and Whitby, K.T. Aerosol classification by electric mobility: apparatus, theory and applications. Journal of Aerosol Science 6 (1975): 443-451.

Kobayashi, Y., Nakashima, H., Takagi, D., and Homma, Y. CVD growth of single-walled carbon nanotubes using size-controlled nanoparticle catalyst. Thin Solid Films 464-465 (2004): 286-289.

Kokai, F., et al. Growth dynamics of single-wall carbon nanotubes synthesized by CO_2 laser vaporization. Journal of Physical Chemistry B 103 (1999): 4346–4351.

Lakshmi, B.B., Dorhout, P.K., and Martin, C.R. Sol-gel template synthesis of semiconductor nanostructures. Chemistry of Materials 9 (1997): 857-862.

Lee, Y.T., Park, J., Choi, Y.S., Ryu, H., and Lee, H.J. Temperature-dependent growth of vertically aligned carbon nanotubes in the range 800-1100 ºC. Journal of Physical Chemistry B 106 (2002): 7614-7618.

Li, P.G., Tang, W.H., and Wang, X. Synthesis of ZnO nanowire arrays and their photoluminescence property. Journal of Alloys and Compounds 479 (2009): 634-637.

Li, Y., Cheng, G.S., and Zhang, L.D. Fabrication of highly ordered ZnO nanowire arrays in anodic alumina membranes. Journal of Materials Research 15 (2000): 2305-2308.

Lian, H.B., Cai, J.H., and Lee, K.Y. Field emission characteristics from tapered ZnO nanostructures grown onto vertically aligned carbon nanotubes. Vacuum 84 (2009): 534-536.

Liu, C.H., et al. Selective interaction of a soluble pentacene derivative with metallic single-walled carbon nanotubes. Chemical Physics Letters 471 (2009): 97–102.

Liu, J.W., Li, X.J., and Dai, L.M. Water-assisted growth of aligned carbon nanotube–ZnO heterojunction arrays. Advance Materials 18 (2005): 1740-1744.

Liu, Y., et al. Amorphous carbon nanotubes produced by a temperature controlled DC arc discharge. Carbon 42 (2004): 1852-1855.

Maruyama, S., Einarsson, E., Murakami, Y., and Edamura, T. Growth process of vertically aligned single-walled carbon nanotubes. Chemical Physics Letters 403 (2005): 320-323.

Misra, A., Tyagi, P.K., Singh, M.K., and Misra, D.S. FTIR studies of nitrogen doped carbon nanotubes. Diamond & Related Materials 15 (2006): 385-388.

Musso, S., Porro, S., Rovere, M., Giorcelli, M., and Tagliaferro, A. Fluid dynamic analysis of gas flow in a thermal-CVD system designed for growth of carbon nanotubes. Journal of Crystal Growth 310 (2008): 477-483.

Nasibulin, A.G., Moisala, A., Brown, D.P., Jiang, H., and Kauppinen, E.I. A novel aerosol method for single walled carbon nanotube synthesis. Chemical Physics Letters 402 (2005): 227–232.

Nomura, K., et al. Thin-film transistor fabricated in single-crystalline transparent oxide semiconductor. Science 300 (2003): 1269-1672.

Nyamori, V.O., Mhlanga, S.D., and Coville, N.J. The use of organometallic transition metal complexes in the synthesis of shaped carbon nanomaterials. Journal of Organometallic Chemistry 693 (2008): 2205-2222.

Özgür, Ü., et al. A comprehensive review of ZnO materials and devices. Journal of Applied Physics 98 (2005): 041301.

Pan, Z.W., Dai, Z.R., and Wang Z.L. Nanobelts of semiconducting oxides. Science 291 (2000): 1947-1949.

Paradise, M., and Goswami, T. Carbon nanotubes-production and industrial applications Materials & Design 28 (2007): 1477-1489.

Pearton, S.J., Norton, D.P., Ip, K., Heo, Y.W., and Steiner, T. Recent progress in processing and properties of ZnO. Superlattices and Microstructures 34 (2003): 3-32.

Pop, E., Mann, D., Wang, Q., Goodson, K., and Dai, H. Thermal conductance of an individual single-wall carbon nanotube above room temperature. Nano Letters 6 (2006): 96–100.

Popov, V.N. Carbon nanotubes: properties and application. Materials Science and Engineering: R: Reports 43 (2004): 61–102.

Port, F. Zinc handbook: properties, processing and use in design. CRC. 1991

Puengjinda. P., Sano, N., Tanthapanichakoon, W., and Charinpanitkul, T. Selective synthesis of carbon nanotubes and nanocapsules using naphthalene pyrolysis

assisted with ferrocene. <u>Journal of Industrial and Engineering Chemistry 15</u> (2009): 375-380.

Ravindran, S., Bozhilov, K.N., and Ozkan, C.S. Self assembly of ordered artificial solids of semiconducting ZnS capped CdSe nanoparticles at carbon nanotube ends. <u>Carbon 42</u> (2004): 1537-1542.

Saito, R., Dresselhaus, G., and Dresselhaus, M.S. <u>Physical properties of carbon nanotubes</u>. London: Imperial College Press, 1998.

Song, W.Y., et al. Vertical growth of ZnO nanowires on c-Al_2O_3 substrate by controlling ramping rate in a vapor-phase epitaxy method. <u>Journal of Physics and Chemistry of Solid 69</u> (2008): 1486-1490.

Stanek, J., Marest, G., Jaffrezic, H., and Binczycka, H. Interactions of iron implants in transition metals. <u>Physical Review B 52</u> (1995): 8414-8422.

Tang, D., Sun, L., Zhou, J., Zhou, W., and Xie, S. Two possible emission mechanisms involved in the arc discharge method of carbon nanotube preparation. <u>Carbon 43</u> (2005): 2812-2816.

Thostenson, E.T., Ren Z., and Chou, T.W. Advances in the science and technology of carbon nanotubes and their composites: a review. <u>Composites Science and Technology 61</u> (2001): 1899-1912.

Umar, A., Kim, S.H., Lee, Y.-S., Nahm, K.S., and Hahn Y.B. Catalyst-free large-quantity synthesis of ZnO nanorods by a vapor–solid growth mechanism: Structural and optical properties. <u>Journal of Crystal Growth 282</u> (2005): 131-136

Wang, F., et al. Interactions between individual carbon nanotubes studied by Rayleigh scattering spectroscopy. <u>Physical Review Letters 96</u> (2006): 1676401.

Weissker, U., Hampel, S., Leonhardt, A., and Büchner, B. Carbon nanotubes filled with ferromagnetic materials. <u>Material 3</u> (2010): 4387-4427.

Wu, C., Xu, J., Li, J., Dong, G., and Guan, L. The effect of the catalyst metals on the thermal-oxidative stability of single-walled carbon nanotubes. <u>Physica E</u> (2009) 41: 1591-1595.

Wu, H.Q., Wei, X.W., Shao, M.W., and Gu, J.S. Synthesis of zinc oxide nanorods using carbon nanotubes as templates. <u>Journal of Crystal Growth 265</u> (2004): 184-189.

Wu, M., et al. Study of the catalytic characteristics of nanooxide decorated carbon nanotubes for waste water processing. <u>Colloids and Surfaces A: Physicochemical and Engineering Aspects 313-314</u> (2008): 264-267.

Wu, R., and Xie, C. Formation of tetrapod nanowhiskers and its optical properties. <u>Material Research Bullletin 39</u> (2004): 637-645.

Xu, C.X., and Sun, X.W. Multipod zinc oxide nanowhiskers. <u>Journal of Crystal Growth 277</u> (2005): 330-334.

Yamabe, T. Recent development of carbon nanotubes. <u>Synthetic Metals 70</u> (1995): 1511–8.

Yu, K., Zhang, Y.S., Xu, F., Li, Q., and Zhu, Z.Q. Significant improvement of field emission by depositing zinc oxide nanostructures on screen-printed carbon nanotube films. <u>Applied Physics Letters 88</u> (2006): 153123.

Yu, S., et al. Field emission energy distribution of MgO-coated MWCNTs. <u>Physica B 323</u> (2002): 177-179.

Yudasaka, M., et al. Mechanism of the effect of NiCo, Ni and Co catalysts on the yield of Single-wall carbon nanotubes formed by pulsed Nd:YAG laser ablation. <u>Journal of Physical Chemistry B 103</u> (1999): 6224-6229.

Yudasaka, M., Komatsu, T., Ichihashi, T., and Iijima, S. Single-wall carbon nanotube formation by laser ablation using double-targets of carbon and metal. <u>Chemical Physics Letters 278</u> (1997): 102–106.

Zhang, Y., Lin, B., Sun, X., and Fu, Z. Temperature-dependent photoluminescence of nanocrystalline ZnO thin films grown on Si (100) substrates by the sol–gel process. <u>Applied Physics Letters 86</u> (2005): 131910.

Zhou, Z., Liu, J., and Hu, S. Studies on the kinetics process of tetra-needle-like ZnO whisker growth. <u>Journal of Crystal Growth 276</u> (2005): 317-320.

APPENDICES

APPENDIX A

Temperature profiles

Before doing experiments, temperature profiles in quartz tube reactor at the synthesizing temperatures of 800, 850 and 900 ℃ were investigated from inlet to outlet of the quartz tube with interval of 2 cm.
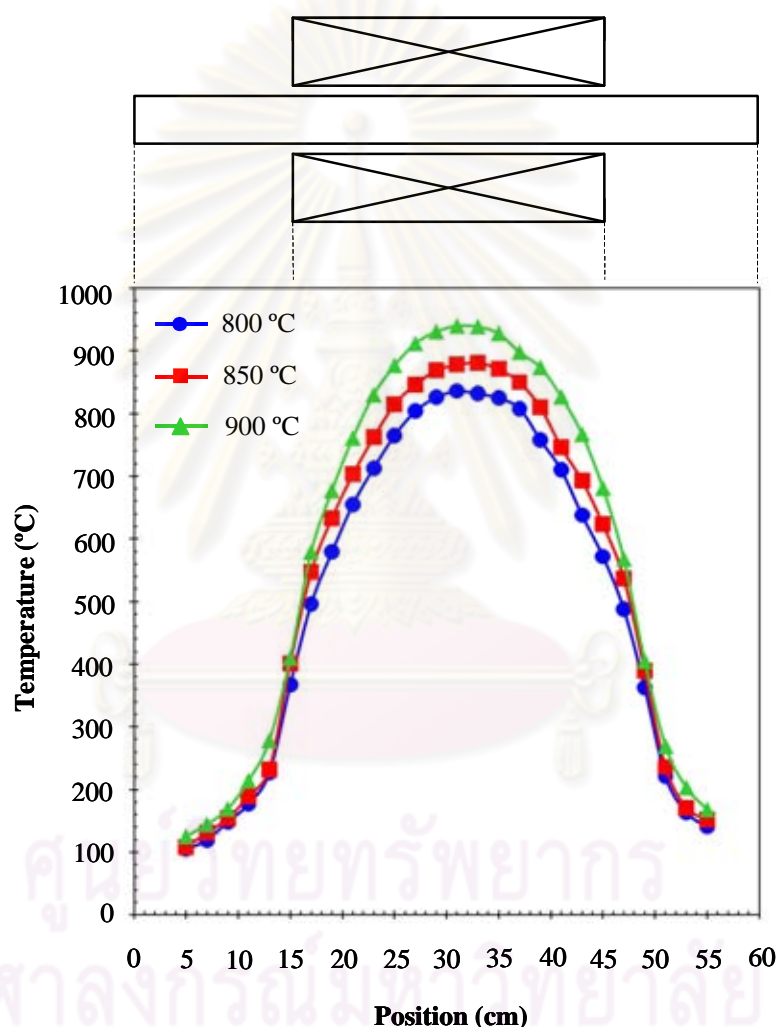

Figure A1 Temperature profiles inside the quartz tube reactor at the synthesizing temperatures of 800, 850 and 900 ℃.

Temperature profiles inside the quartz tube reactor at the synthesizing temperatures of 800, 850 and 900 ℃ were mapped, as shown in Figure A1. Each temperature profile consisted of 3 temperature gradients along flow direction including temperature increased from the lowest to the highest (0-15 cm from the

inlet) where was defined as zone 1, the temperature was the highest (15-45 cm from the inlet) where was defined as zone 2 and the temperature decreased from the highest to the lowest (45-60 cm from the inlet) where was defined as zone 3. Because indirect effect of temperature gradients and velocities gradients throughout the quartz tube reactor on the formation of the carbon nanoparticles, ZnO nanoparticles and their composites, therefore, in this work, the carbon nanoparticles, ZnO nanoparticles and their composites were studied by sampling the particles from each zone.

APPENDIX B

Calculation of partial pressure

Partial pressure of oxygen was calculated using ideal gas mixture. The mole fraction of an individual gas component in an ideal gas mixture can be expressed in terms of the component's partial pressure:

$$x_A = \frac{n_A}{n} \qquad (A1)$$

$$p_A = x_A \times p \qquad (A2)$$

where :
n	=	total moles of the gas mixture
p_A	=	partial pressure of gas component A in gas mixture
n_A	=	mole of gas component A in gas mixture
x_A	=	mole fraction of gas component A in gas mixture
p	=	pressure of gas mixture

For example, in case of 100 mL/min of oxygen and 200 mL/min of nitrogen flow rate

$$n_{O_2} = \frac{0.1(L/min) \times 1.42(g/L)}{32(g/mole)}$$
$$= 4.44 \times 10^{-3} \text{ mole/min}$$

$$n_{N_2} = \frac{0.2(L/min) \times 1.25(g/L)}{28(g/mole)}$$
$$= 8.93 \times 10^{-3} \text{ mole/min}$$

$$n = 1.33 \times 10^{-2} \text{ mole/min}$$

$$x_{O_2} = \frac{4.44 \times 10^{-3} (mole/min)}{1.33 \times 10^{-2} (mole/min)}$$

$$= \ 0.33$$

If assumption was partial pressure inside the reactor is 1 atm. Therefore, partial pressure of gas component is equal to mole fraction.

ศูนย์วิทยทรัพยากร
จุฬาลงกรณ์มหาวิทยาลัย

APPENDIX C

Publications

Journal:

Publications Authored by J. Klanwan:

Klanwan, J., Akrapattangkul, N., Pavarajarn, V., Seto, T., Otani, Y., and Charinpanitkul, T. Single-step synthesis of MWCNT/ZnO nanocomposite using co-chemical vapor deposition method. <u>Materials Letters 64</u> (2010): 80-82.

Klanwan, J., Seto, T., Furukawa, T., Otani, Y., Charinpanitkul, T., Kohno, M., and Hirasawa, M. Generation and size classification of single-walled carbon nanotube aerosol using atmospheric pressure pulsed laser ablation (AP-PLA). <u>Journal of Nanoparticle Research 12</u> (2010): 2747-2755.

Publications Co-Authored by J. Klanwan:

Charinpanitkul, T., Sano, N., Puengjinda, P., **Klanwan, J.**, Akrapattangkul, N., and Tanthapanichakoon W. Naphthalene as an alternative carbon source for pyrolytic synthesis of carbon nanostructures. <u>Journal of Analytical and Applied Pyrolysis 86</u> (2009): 386-390.

Proceeding:

Klanwan, J., Ratchahat, S., Soottitantawat, A., Kohno, M., Furukawa , T., Seto T., Otani, Y., and Charinpanitkul T. Formation of multi-walled carbon nanotubes induced by nickel nanoparticles using low-pressure chemical vapor deposition technique. Proceeding of the 17th Regional Symposium on Chemical Engineering, Queen Sirikit National Conventional Center, Bangkok, Thailand, November 22-23, 2010: MSE 495.

VITA

Miss Jiraporn Klanwan was born in April 18, 1984. She studied in secondary educations at Bangmulnak Phoomiwitthayakom School, Phichit. In 2006, she graduated Bachelor Degree of Engineering (Chemical Engineering) from King Mongkut's Institute of Technology Ladkrabang. After that, she continued to study in Doctoral degree in Center of Excellence in Particle Technology at Department of Chemical Engineering, Faculty of Engineering, Chulalongkorn University.